Investigation of Stabilizing Agents in Thin Sol-Gel Zirconium Oxide Anti-corrosion Coatings on Iron Materials

Vom Fachbereich Chemie
der Technischen Universität Darmstadt

Zur Erlangung des akademischen Grades eines
Doktor-Ingenieurs (Dr.-Ing.)

Dissertation

Ruperto Antonio Ugas Carrión

2010

Investigation of Stabilizing Agents in Thin Sol-Gel Zirconium Oxide Anti-corrosion Coatings on Iron Materials

Vom Fachbereich Chemie
der Technischen Universität Darmstadt

zur Erlangung des akademischen Grades eines
Doktor-Ingenieurs (Dr.-Ing.)

genehmigte

Dissertation

eingereicht von

Ruperto Antonio Ugas Carrión, Ing. Quim.
aus Carúpano (Venezuela)

Referent: Prof. Dr. Wolfgang Ensinger
Korreferentin: Prof. Dr. Barbara Albert

Tag der Einreichung: 13.08.2010
Tag der mündlichen Prüfung: 18.10.2010

Darmstadt 2010
D17

Dedicated to my loving mother Josefina

Acknowledgements

First I would like to thank Prof. Dr. Wolfgang Ensinger, my doctoral advisor, for giving me the opportunity to begin this investigation on his crew, for his help in several life occasions, Visa and DAAD support letters, for his comprehension about my work and for his great help given me the HiWi job necesary for my financing .

Likewise, I want to express my heartfelt gratitude to Dr. Falk Sittner, my co-advisor, for his consistent assistance, interest and great help, continous understanding and opportune observations. I greatly appreciate his patience in reading my paper manuscripts and thesis and his useful annotations which improved my thesis.

I would like special acknowledge Prof. Dr. Barbara Albert for her kind acceptance to act as co-referee of my thesis.
My sincerely thanks to Dr. Stefan Flege for the important SIMS measurements, his time, advice and for his continuos helpful and technical support in many opportunities.
I would like to acknowledge Prof. Dr. Hans-Joachim Kleebe, his crew, Frau Ulrike Kunz for the helpful cooperation with the TEM measurements and to Dr. Roland Schierholz for his very important support in the crystals analysis.
I am also very thankful to Dr. Joachin Brötz for the countless and important XRD measurements and for his necessary explanations about the crystalline structure of my samples.
My special thanks go to Prof. Dr. Michael Reggelin and Frau T. Solms for their understanding and help with the Promotionskolleg.
I am very thankful to Prof. Dr. Andreas Klein and his crew for the XPS measurements.
I want to thank Veronika Metje for her great support from the DAAD office

My further Thanks go to:

Dr. Prof. Koumei Baba for his kind cooperation with the plasma ion bean implantation samples and to Dr. Ruriko Hatada for her collaboration with the deposition.

Dr. Prof. Victor Carrizales and Dr. Prof. Lucas Álvarez for their support.

Dr. Gunther Kraft for the ESMA analysis and for the good advice and humor.

Brunhilde Thybusch for SEM and microscopical pictures.

Claudia Fasel for the hardness measurements and support with microscopical images.

Thomas Hermann for his help with SEM images.

Mehdi Yekehtaz, my working collegue, for his kind collaboration with SEM images and in the electrochemistry laboratory.

Dorotea Berres and Renate Benz for their collaboration in chemistry laboratory and for the constant support with new bulbs for our light microscop.

Jens von Ringleben for his productive advice and support with EIS measurements.

Dr. Gerhard Miehe for the allowowance to use his PIES program for some TEM crystal analysis.

Dr. Ljuba Schmitt and Jens Kling for their help with High Resolution TEM analysis.

Antje Pappenhagen, our kind secretary, for her assistance during the administrative procedures.

Eduard Gunnesch for the XPS measurements.

Dr. Olaf Baake for his kind advice

I am also very thankful to all my colleagues at the FG Materialanalytik, FB Material-und Geowissenschaften, TU-Darmstadt for the friendly and affable working ambience, helpful collaboration and the great Caferunde.

I would like to thank the government of Venezuela represented through the Fundación Gran Mariscal de Ayacucho (FUNDAYACUCHO) for the financing of a great part of my doctoral studies in Germany and to the German Academic Exchange Service (DAAD) for the financing of my german course and for given

me the great opportunity to make doctoral studies in Germany and to the TU-Darmstadt for supporting the working materials.

I express my hearty thanks to my loving mother Josefina, my sisters Cruz and Teresa, my others brother and sisters, my nephews Henry Ugas, Rebeca and Leonardo, to Sonia Negrau and her family, as well as to Oxana and my friends, Kathrin, Rudi, Yuly, Danka, Heinrich, Daniel, Juan, Miguel, Manuel Heib, for their love, comprehension and assistance during my stay in Germany and their belief in me for the successful ending of this work.

Abstract

Thin protective zirconium oxide coatings prepared via sol-gel with zirconium propoxide and acetyl acetone (acac) or hydroxypropyl cellulose as stabilizers have been successfully deposited onto iron substrates at low temperature. Electrochemical current density vs. potential scans showed a reduction of the iron dissolution current density and coating porosity in comparison to uncoated iron, with a strong decrease of these parameters around 5 orders of magnitude for a HPC concentration = 0.004 g/l. This result is expected as the steric effect of HPC.

A mixed oxide layer of zirconium and iron was observed in SIMS depth profiles. The mixed oxide layer thickness showed a dependence on the acac molar ratio. Increases of acac shorted the overall film thickness, while the mixed oxide layer was thicker. ZrO_2-HPC coatings displayed however, a thicker mixed oxide layer and additional increases of the zirconium intensity direct onto substrate surface. So a higher interdiffusion of zirconium into deeper layers and of iron towards coating surface was reached.

XRD revealed that the mixed oxide layer is localized between the substrate and coating surface and possess crystalline structure. At a HPC concentration = 0.004 g/l no ZrO_2 reflexes could be detected. ZrO_2 crystals of 70 nm size were identified by TEM in ZrO_2-acac coatings. However, ZrO_2-HPC films showed an amorphous structure constituted of ZrO_2 and iron oxide containing nanocrystalline zirconium oxide particles immersed in the mixed oxide layer. The crystals (monoclinic 112) size was between 5 and 10 nm. This result explains why there were not zirconium oxide reflexes visible in the XRD analysis. Obviously the ZrO_2 crystalline particles are too small (less than 10 nm) to be detected by XRD so they appear as amorphous material [83]. The particles are immersed in a compact and amorphous mixed oxide matrix. The correlation between growth of the mixed oxide phase and decrease of dissolution current density suggests that it is the mixed oxide phase with zirconium nanoparticles that is responsible for the reduction of film porosity and the good corrosion protection properties of the films.

Zusammenfassung

Dünne Zirkoniumoxidschutzschichten auf Basis von Zirkoniumpropoxid mit Acetylaceton (acac) und Hydroxypropylcellulose (HPC) als Stabilisatoren wurden erfolgreich durch Sol-Gel-Verfahren synthetisiert und auf Eisenwerkstoffen bei Raumtemperatur abgeschieden. Potenzialmessungen zeigten eine Erniedrigung der Stromdichte und der Porosität im Vergleich zu unbeschichtetem Eisen, wobei die ZrO_2-HPC-Beschichtungen besonders starke Erniedrigungen um bis zum 5 Größenordnungen zeigten. Dies ist vermutlich ein Ergebnis des sterischen Effekts von HPC und wurde bei einer optimalen Konzentration von 0,004 g/l erreicht. In SIMS-Messungen wurde zusätzlich eine Oxidschicht bestehend aus ZrO_2 und Eisenoxid festgestellt. Die Dicke dieser Oxidschicht weist eine Abhängigkeit von dem Molaranteil des Acetylacetons auf. Mit ansteigendem Anteil von acac wird die gesamte Schichtdicke dünner und die Oxidschicht dicker. SIMS-Messungen zeigten ZrO_2-HPC-Schichten bei den dennoch eine dickere Oxidschicht und zusätzlich einen Anstieg der Zirkoniumintensitäten direkt auf der Substratoberfläche. Daher findet eine starke Interdiffusion von Zirkonium in tiefere Schichten und von Eisen in Richtung der Probenoberfläche statt.

Die kristalline Oxidschicht liegt zwischen Substrat und Beschichtungsoberfläche, was durch die XRD-Messungen bestätig wurde. Bei einer Konzentration von HPC = 0,004 g/l konnte kein Reflex von kristallinem ZrO_2 detektiert werden. ZrO_2-Kristalle mit einer durchschnittlichen Größe von 70 nm wurden mittels TEM in ZrO_2-acac-Schichten beobachtet. Allerdings zeigten die ZrO_2-HPC-Schichten eine amorphe Oxidschichtstruktur aus Eisen und Zirkoniumoxid mit nanokristallinen ZrO_2-Partikeln. Dies erklärt, warum keine ZrO_2-Reflexe bei den XRD-Messungen detektiert wurden. Offensichtlich sind die ZrO_2-Partikel keiner als 10 nm, sodass sie als amorphes Material beim XRD erscheinen. Die Partikel sind eingebettet in eine kompakte und amorphe Oxidmatrix. Die Zuordnung zwischen dem Wachstum der Oxidschichtphase und der Reduzierung der anodischen Stromdichte weist darauf hin, dass die Oxidschichtphase sowie die Nanopartikel für die Erniedrigung der Porosität und die guten Korrosionsschutzeigenschaften der dünnen Schichten verantwortlich sind.

Index of Content

Symbols and Acronyms

Acac	----------	Acetyl acetone
S_N1	----------	Nucleophilic substitution first order
S_N2	----------	Nucleophilic substitution second order
M	----------	Metal atom
O	----------	Oxygen atom
--O--	----------	Oxo bridge
R	----------	Radical alkyl group
HZ	----------	Acidic reactant
VDWL	----------	Van der Waals-London attraction forces
(c)	----------	Ionic strength
NMR	----------	Nuclear magnetic resonance
MW	----------	Molar weight
HPC	----------	Hydroxypropyl cellulose
ΔG	----------	Free Gibbs energy
ΔQ	----------	Charge flow
Φ	----------	Electrical potential in electric work
E	----------	Electrochemical potential
ΔN	----------	Amount of transferred material
Z	----------	Metal valence
E^0	----------	Standard electrode potential
SHE	----------	Standard hydrogen potential
i_a	----------	Current density
i_0	----------	Maximum current density at equilibrium
E_{corr}	----------	Corrosion potential
i_{corr}	----------	Corrosion current
Rp	----------	Polarization resistance
βa	----------	Anodic Tafel slope
βc	----------	Cathodic Tafel slope
k	----------	Corrosion rate

Aim

The worldwide corrosion cost encloses every year billions of dollars equivalent to approximately 3 % of the world´s gross domestic product [50]. These costs arise not only from direct corrosion damage but also from its follow-up costs due to repairs or downtimes of machines. Besides the financial aspect the consequences for the environment may be dramatically higher if toxic substances are involved.

The demands of high technology fields such as microelectronics and optics have made the development of effective counter measures against corrosion a real challenge. While the dimensions of technical devices shrink down to nanometer scale new solutions against wear and corrosion have to be developed to guarantee reliable protection also in nanotechnology applications.

Since some decades the sol-gel technique has generated efficient approaches with the synthesis of thin metal oxide coatings. They can act as a barrier between metal substrate and the aggressive environment and can be deposited from a large spectrum of precursor materials. The sol-gel process combines fast, cheap and convenient deposition with the possibility to produce new classes of materials which can be designed through various process parameters to the desired needs.

Major drawbacks of this method are the complexity of different reactions during the deposition procedure and the process-related porosity which is undesirable for corrosion protection applications. The interrelations of process parameters and their effect on the final structure of the product are still not fully understood. While a lot of applications in fields such as catalysis or separation benefit from porous sol-gel materials there is only little knowledge existing about how to reduce or eliminate the film porosity. One reason is the strong dependence of the film properties on the subjacent substrate material which makes it hard to establish general principles and mechanisms that can be transferred to other coating/substrate systems.

In the present work metallic iron substrates are coated with thin zirconium oxide sol-gel films from a zirconium n-propoxide precursor. This material has already

proven its favorable protection properties on iron materials. The aim of this work is the investigation of sol-gel deposition parameters and film growth mechanisms that are crucial for the formation of porous structures and to develop a strategy to effectively reduce the process-related porosity.

The focus of the research will be on the role of certain substances that are used in the process as modifying and stabilizing agents. They are known to control various reactions pathways and to have decisive influence on the film structure. But due to the complex changes that occur during the deposition procedure their effect on film porosity and the mechanism how they affect the final film structure is not clear, yet.

The stabilizing agents acetyl acetone (acac) and hydroxypropyl cellulose (HPC) will be used to gather information about their structure building effect and to investigate their potential for the development of low-porous, protective thin films.

A. Theory

I. Sol-Gel process

1. General

Sol-gel process has its origin in the 19th century when Ebelmen carried out experiments with $SiCl_4$ and alcohol and observed a gelation of the material when it was exposed to air [1]. Later on the method was picked up by ceramic industry for the development of special kinds of glass from colloidal solutions of metal alkoxides through controlled hydrolysis and condensation reactions. Therefore the initially used silicon was replaced by more reactive transition metals such as titanium, zirconium, cerium or vanadium [2,3]. Nowadays this process is widely used for the development of a huge spectrum of ceramic products such as films (e.g., by dip coating or spin coating), or monoliths by casting into a desired shape, glasses, fibres, powders (microspheres, nanospheres), membranes and highly porous materials like xerogels and aerogels [4-9]. The technique has become a common method in glass industry and optics for the fabrication of reflective and protective oxide coatings [10-12]. Recently protective sol-gel films have been applied to proteins for encapsulation [13]. There are other applications in the micro- and nanotechnology for protection of sensitive materials against abrasion or corrosion [14-17]. The major advantages of this method are the uncomplicated technical equipment, low process temperatures, the huge choice of available precursor materials and the possibility to design all kinds of product properties such as porosity, flexibility, hardness and density via different process parameters. A sketch of the general process is shown in fig.1 [4].

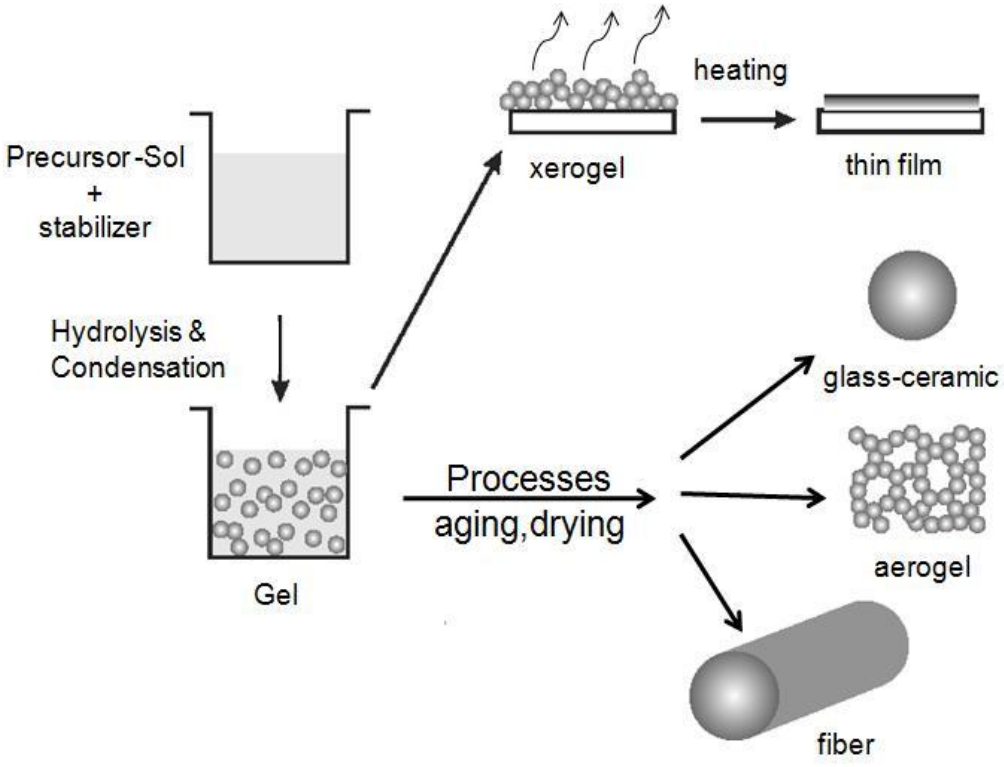

Fig.1 schema of sol gel process

The precursor reacts via hydrolysis and condensation where small molecules such as water or alcohol are released. In the further progress a colloidal suspension is developed or a polymerized network with hundreds or thousands of linear or branched monomers. When the size of the branched molecule reaches the dimension of the solution the phase is called “gel” [4]. At the gel point the phase behaves like one giant molecule which extends over the whole solution. A network of dispersed particles can be also achieved, resulting in a colloidal gel depending on the chelating and bridging nature of different agents and the flocculation or dispersion of gel particles. The following step after gelation is called “aging”. It is characterized by further condensation, precipitation of monomers or transformation reactions within the solid or liquid phases. This includes the release of liquid solvent from pores and shrinkage. During the drying step further liquid evaporation will occur through pores in the structure and the network will show deformation and shrinkage effects. The final

product is a highly porous material called “xerogel” which consists to 60-90% of air. If the gel is dried under supercritical conditions in an autoclave, shrinkage and capillarity can be suspended, resulting in the formation of so called “aerogels” with an extremely low density, consisting of typically 90-99% air. Aerogels are one of the best insulating materials. Both products are used frequently in membrane and catalysis applications [3,4]. The final step of the diagram is a heating procedure. Although most gels appear amorphous after drying, crystalline structures can be obtained during the heating step at elevated temperatures.

1.1 Sol-Gel mechanism

Precursors used in sol-gel applications are usually metal or semi-metal compounds bonded to organic and inorganic ligands. The most common precursors are alkoxides consisting of a silicon or transition metal central atom and alkoxy groups as ligands [4]. Alkoxides react with water by hydrolysis. This allows that a hydroxyl ion attaches a metal atom as shown in the reaction 1. Normally the hydrolysis reaction of silicon compounds proceeds slowly. Transition metals instead react very fast with crystalline precipitation of the metal salt. There are different mechanisms of hydrolysis and the possible products have a strong effect on the formation of chains, branches and complex compounds.

The general hydrolysis reaction can be described as:

$$M(OR)_4 + H_2O \longrightarrow HO—M(OR)_3 + ROH \qquad (1)$$

M is a metal atom and R represents a radical alkyl group. Products of an incomplete hydrolysis can react further with each other in a condensation reaction:

$$HO—M(OR)_3 + HO—M(OR)_3 \longrightarrow (OR)_3M\text{-}O\text{-}M(OR)_3 + H_2O \qquad (2)$$

Through this reaction a polymerization of the phases is possible. A repetition of the condensation step can produce more complex and highly branched compounds that are the basis of sol-gel materials.

Low hydrolysis reactivity of silicon precursors can be enhanced by either basic catalysis via S_N2 mechanism or by acidic catalysis via S_N1 mechanism and with chelating ligands as modifiers as well [5]. The hydrolysis and condensation rate of transition metals appear to be much higher than the rate of silicon alkoxides. Their higher reactivity is due to their lower electronegativity compared to silicon and to their ability to exist in different coordination states [6]. They are stronger electron donators; therefore they react easily with water via S_N1 mechanism without additional catalysis.

The S_N2 mechanism is described in the scheme 1 [5]:

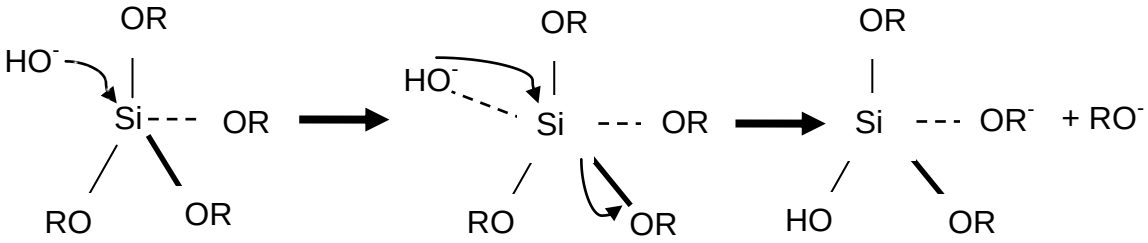

In the presence of hydroxide ions silicon alkoxides will react in a nucleophilic substitution following the S_N2 mechanism with an alkoxide leaving group. The latter can regenerate the catalyst OH^- in a reaction with water. Usually the hydrolysis of silicon alkoxides is slow because of the high electronegativity of silicon compounds.

An alternative reaction may occur in acidic environment via S_N1 mechanism [5]:

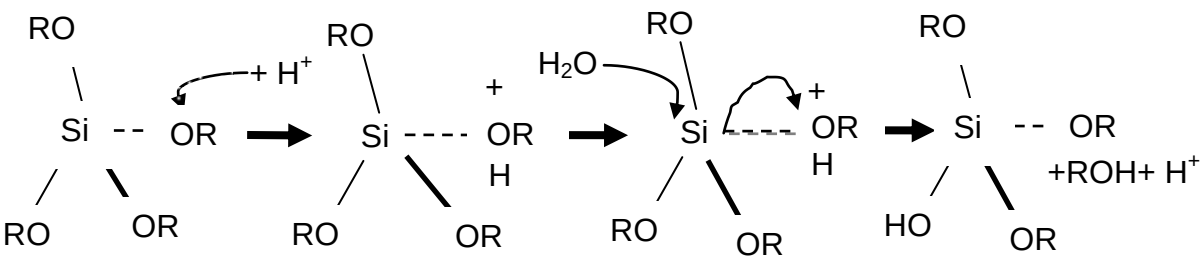

In the first step the alkoxy group is protonated, forming a very good alcohol leaving group. A water molecule can bond to the positively charged silicon, releasing a proton which can restart another hydrolysis cycle.

The hydrolysis rate needs to be moderated to allow further growth and branching of the network in subsequent condensation reactions. There are three different mechanisms of condensation that have to be considered:

Alcoxolation: a bridging oxo group (M---O---) is formed by elimination of an alcohol molecule. This reaction follows the same process as hydrolysis with Si replacing the entering group [6].

Oxolation: in this reaction an oxo bridge (---O---) between two central metal atoms is formed and water is the leaving group.

Olation: a hydroxo bridge ("ol" bridge M--OH) is formed between two metal atoms by elimination of a solvent molecule [3].

The occurrence of these mechanisms depends on the pH and coordination number of the metal. All these reactions are catalyzed by acids but slowed down in basic media [6].

Condensation can occur by two mechanisms:

When the coordination of the metal precursor is saturated the mechanism occurs via nucleophilic substitution with hydroxo group (M---OH) (OH) as nucleophile and H_2O or OH^- (OR) molecules are the leaving group (oxolation) depending on acidic and basic catalysis, respectively [4]. However, via aquo ligand M--$(OH)_2$ none entering group (OH) is obtainable making this mechanism inappropriate:

$$M_1\text{-}OH + M_2\text{-}OR \longrightarrow M_1 - \overset{\overset{H}{|}}{O} - M_2 + OR \qquad (3)$$

In the case when the coordination of the molecular precursor is unsaturated both oxolation and olation can occur only via addition with (M---OH) and/or (M---O---) as nucleophiles producing chains and cycles:

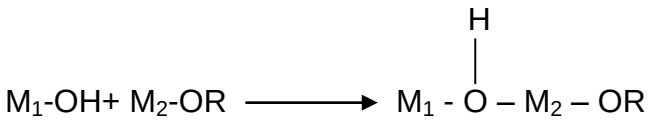

(4)

An increase of the coordination number of M_2 can be achieved as well. This depends on the electronegativity, electronic configuration of the metal atom and the water concentration [6].

1.1 Transition metals

Precursor alkoxides of transition metals react easily with water and the mechanisms of hydrolysis and condensation depend on charge and electronegativity of the metal and pH of the medium. Because of the high reaction rate the addition of moderating and stabilizing agents such as β-diketones, some carboxylic acids or alcohols is necessary to avoid instant crystalline precipitation and to obtain homogeneous films [5, 7]. In contrast to silicon compounds transition metals don't need catalytic additives for hydrolysis and they form stable cationic complexes favoring S_N1 mechanism (scheme 3) [5]:

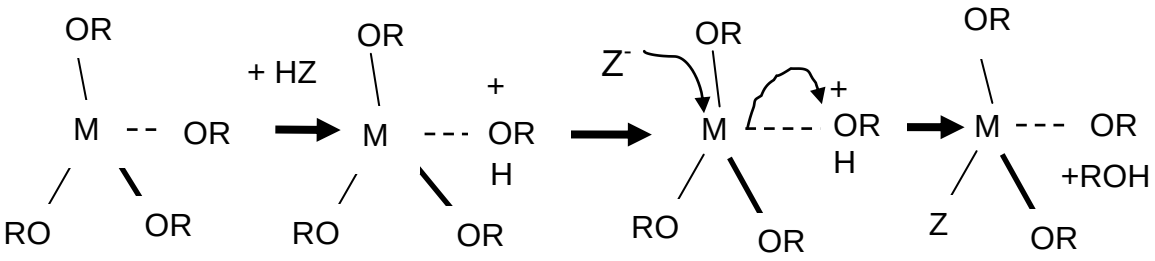

According to Kessler et al. [8], during this mechanism the metal atoms can increase their coordination number and remain connected to more ligands. The ligand exchange, e.g. both hydrolysis and chemical modification, begin with protonation of the partial negatively charged oxygen atom of the alkoxy. This process generates reactive cationic species which coordinate also an additional

donor ligand releasing an alcohol group. The reaction rate depends on the acidity of the HZ reactant, while the nucleophilic properties of the Z^- ligand don't play an important role on the bonding interchange as recently shown for tetravalent metals like titanium and zirconium alkoxide complexes [8].

Hydroxo-aquo precursors of tetravalent metal oxides such as Ti, Zr or Hf can hydrolyze easily and form stable sols. However, the growth mechanism is olation and therefore obtaining clear gels is limited because of dimerization and formation of gelatinous material instead of sol [6]. For example, clear gel of ZrO_2 can be obtained by the formation of stable colloid or dispersion phases in water or neutralizing chloride or nitrate precursors with urea. No defined structure has been achieved until now for these colloidal gels. However, mixed hydroxo –oxo bridges have been reported in the study of amorphous ZrO_2 where a sheet-like structure with Zr atoms is connected through $_3(OH)_1$ and/or $_3(O)_1$ bridges [6]. The terminology of $_x(OH)_y$ determines the number of M atoms x bridged by the number of OH groups y [9].

2. Protective sol-gel coatings

Protective films provide corrosion or abrasion resistance, good adhesion, strength and impart passivation or planarization. The advantages like low process temperatures, cost-efficient hardware, variety of materials and product properties have recommended the sol-gel technique to the field of protective coatings [21-24].

An example of a protective sol-gel layer is shown in fig.2. In this application a sol-gel overcoat is used to protect the sensitive surface of satellite mirrors in aerospace industry. The planarization layer prevents galvanic corrosion of the Fe-Ag couple while planarizing of stainless steel improves the mirror surface; the protective coating protects the reflective silver interface [25,26-29].

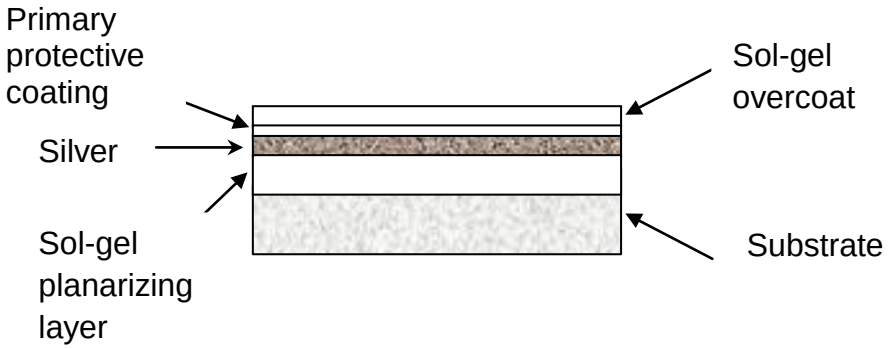

Fig. 2 Reflective metal mirror design and sol-gel protective coating

3. Protective sol-gel coatings

For many applications of protective sol-gel coatings the process-related porosity of the final film due to solvent evaporation is a serious limitation. Especially corrosion resistant coatings have to be free from pores to avoid any exposition of the sensitive metal surface to an aggressive medium. Brinker et al. [4] developed a procedure to reduce the number of pores by controlling the relative evaporation and condensation rate [22]. Likewise, other investigations have revealed that modifying and stabilizing agents have a major influence on the final film structure. Acting as chelating and bridging ligands these agents alter the reactive positions on the alkoxide molecule during the condensation reaction. This may result in a change of size and shape of the primary particles formed in sol-gel treatment of metal alkoxides. They are not influenced by kinetic effects during the hydrolysis or condensation, but by the ligands and modifier properties. [5,8,22].

Another crucial step in the deposition of protective sol-gel coatings is the drying and heating procedure because the average pore size can increase rapidly with rising process temperature due to solvent evaporation. On the other hand a densification is observed which is accompanied by shrinkage of the film structure. Therefore these parameters have to be set up carefully. Porosity means insufficient substrate surface coating and increasing of the risks to development of local corrosion.

II. **Production of protective oxide films on metals**

1. Role of stabilizers and modifiers

1.1 Use of stabilizer as bridging and chelating agents

The addition of stabilizing or modifying agents is necessary to moderate the reaction rate of transition metal alkoxides. Beyond that these stabilizers offer the possibility to adjust certain structural film properties such as density and flexibility to the desired needs. The general effect is based on the chelating and bridging properties of the stabilizing molecules. Reaction rates of hydrolysis and condensation can be controlled via substitution or elimination of metal-ligand bonds. This way certain reactive sites of the precursor molecule are stabilized and will preferably react in the polycondensation-process. As a result the sol density and the number of interconnections in the three-dimensional network will be altered.

The option to decrease the process-related porosity by modifying additives is especially attractive to the preparation of thin protective metal oxide coatings. The best stabilizing agents for this application contain carboxyl functional groups [30], but also hydroxy-, ester-, amino- and ß-diketone-groups can be advantageous. The affinity of each group to the surface of the suspended colloidal particles in the gel determines the effectiveness of stabilization. Hydrophobic or hydrophilic groups interact with corresponding polar or non-polar sites of the particle surface in the presence of water, forming bonds by electrostatic force.

Besides the type of stabilizer its concentration is also important because the stabilizer/precursor ratio determines the number of available reactive sites when more than one stabilizing molecule may aggregate with the precursor particle [30]. Another crucial parameter is the choice of an appropriate solvent because the polar character of the solvent, i.e. its affinity to both stabilizer and precursor molecule can either increase or even reverse the stabilizing effect, resulting in flocculation instead of stabilization [17].

Different stabilizing mechanisms have been reported [31,32]:

Electrostatic or charge stabilization: acts similar to an electrical double layer

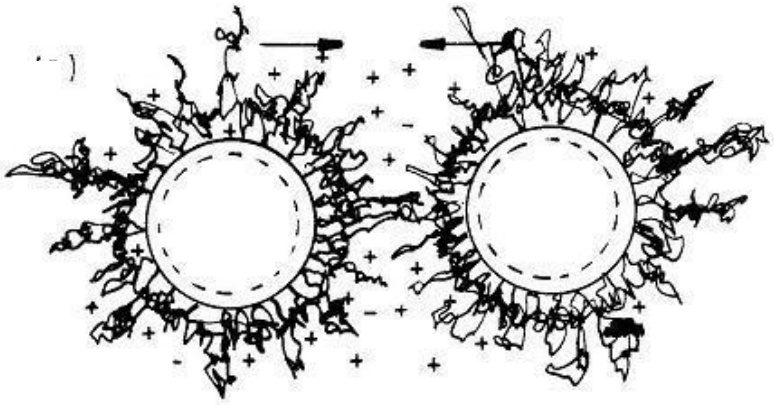

Fig. 3 Charged particles with nonionic polymers [31]

The principle is shown in fig. 3: ionic groups adsorb colloidal particles on the dispersed gel and form an electric barrier around the particle surface, resulting in mutual repulsion of equal charges in the electrostatic field. Hereby the thickness of the double layer plays an important role. It is related to the van der Waals-London (VDWL) attraction force which is defined as the minimal distance (5-10 nm) that prevents the aggregation of attractive particles. This way the particles are stabilized by the balance of attractive and repulsive forces. If the ionic strength of the dispersion medium (c) is > 10^{-1} M, the thickness of the double layer will shrink below the minimal distance to prevent attraction between particles and coagulation will be inevitable [31]. This type of stabilization is limited to polar media.

Steric stabilization: adsorbed or chemically bonded polymeric molecules as shown in fig. 4:

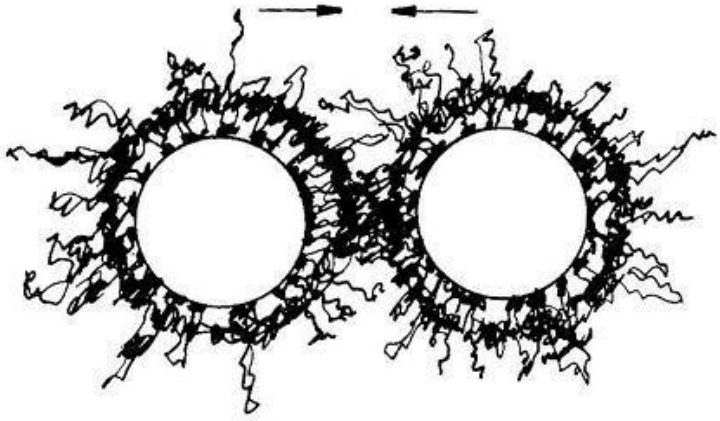

Fig. 4 Steric stabilization schema [31]

Steric stabilization occurs when suspended colloidal particles of a sol are adsorbed to polymeric macromolecules via chemisorption or grafting. It prevents the flocculation of particles and allows dispersion, that way steric stabilization is achieved. Good polymeric stabilizers are most commonly those with large polymer chains. This provides enough repulsion to reduce the VDWL attraction in the colloidal sol. This type of mechanism is more stable than electrostatic stabilization and has more advantages. For example the steric stabilization is relatively independent on the electrolyte concentration in the dispersion medium. Steric stabilization can be utilizable in non-polar and polar media. Another aspect to be considered is the fact that charge stabilized gels can produce irreversible particle agglomeration. However, a flocculation due to the steric effect is reversible. This can be explained by the electrostatic effect which generates thermodynamically metastable dispersions while steric stabilizers provide thermodynamically stable sols [4, 31].

Polymers are the best stabilizing agents due their high molar weight, especially when they contain repeating double units. Very effective segments are repeatable carboxyl or hydroxyl groups with alternating polar and nonpolar parts [34]. These substances can be used in both aqueous and non-aqueous dispersion mediums.

Depletion stabilization: free polymer in the dispersion medium

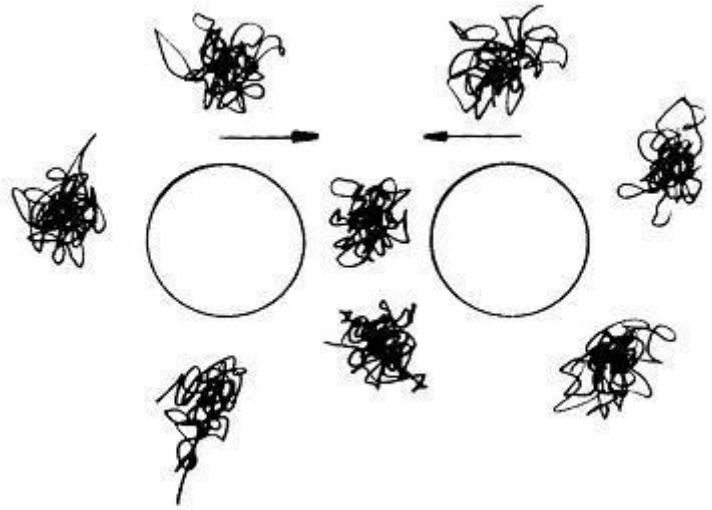

Fig. 5 Depletion stabilization [31]

Macromolecules are dispersed in a soluble medium and prevent coalescence of particles (fig. 5). The exact mechanism of this type of stabilization is not completely clear until now [3,4,31].

1.1.1 Acetyl acetone (acac)

The structure of the complex compounds formed after the gelation step in the sol-gel process is still unknown [4,35]. It becomes even more complex when the original precursor is modified by a stabilizing agent. In the case of metal alkoxides acetyl acetone, which is also used in the preparation of acetylacetonate catalysts, is often applied as a bidentate ligand [23,36,37].
With the molecular formula $CH_3COCH_2COCH_3 = C_5H_8O_2$ acetyl acetone is a diketone with a keto and an enol form which remain coexistent in solution as shown in fig. 6.

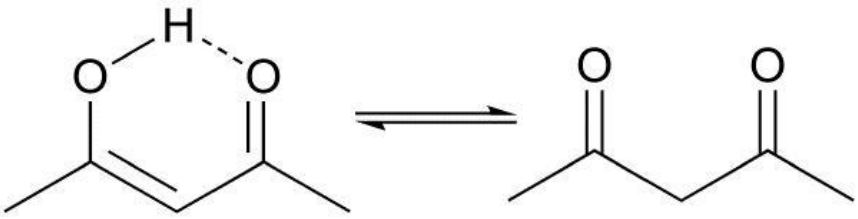

Fig. 6 Enol and Keto forms of acetyl acetone

This reagent has the ability to form several complexes with transition metals such as titanium, zirconium, hafnium, manganese, niobium, etc. [4,6]. In the exothermic reaction of the metal alkoxide with acetyl acetone a proton is released and the chelating anion acetylacetonate = acac ($C_5H_7O_2^-$) is formed with the negative charge delocalized between both oxygen atoms. The latter bound readily to the transition metal atom and form chelate complexes which are freely soluble in organic solvents.

The structure of a stable zirconium alkoxides - acac complex is shown in Fig. 7.

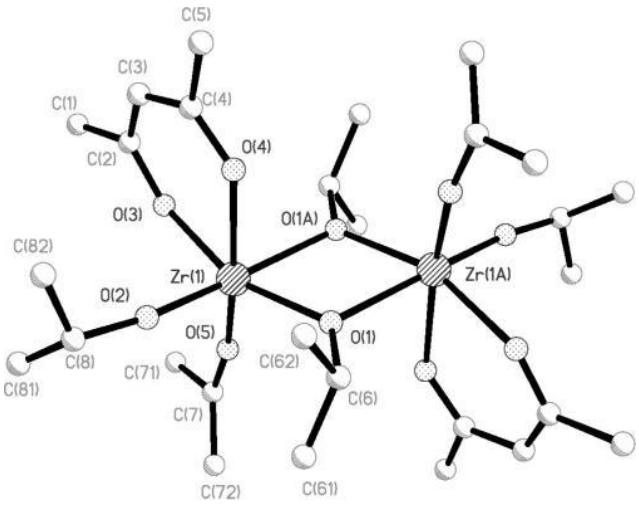

Fig. 7 Molecular structure of $[Zr(O^iPr)_3(acac)]_2$ [36]

The structural form showed in fig.7 is one of the most stable complexes of modified zirconium n-propoxide $Zr(OPr)_4$ studied by nuclear magnetic resonance (NMR) in [36].

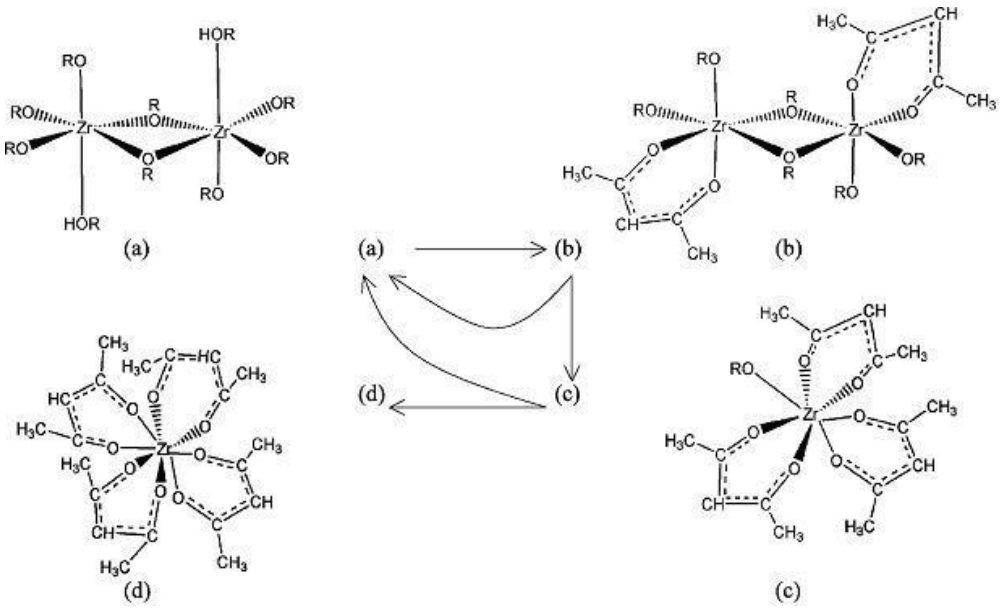

Fig. 8 Different molecular structures of zirconium compounds induced by acac [36]

However, depending of the amount of acetyl acetone the stable form (b) can change into an unstable form (c) or further into another stable form (d). Likewise they can reversibly change back into the original precursor as shown in fig. 8. This behavior can be transferred to other transition metal alkoxides. The crystalline structure and particle size of the final coating are also affected by the amount of acetyl acetone [4, 24, 36]

1.1.2 Hydroxypropyl cellulose (HPC) as stabilizer

This polymer is available with different molar weights (MW) as a crystalline powder, for example: 80,000, 100,000 or 370,000 g/mol.

Hydroxypropyl cellulose (HPC) is an ether derivative of cellulose in which some of the hydroxyl groups in the glucose units have been hydroxypropylated as shown in fig. 9.

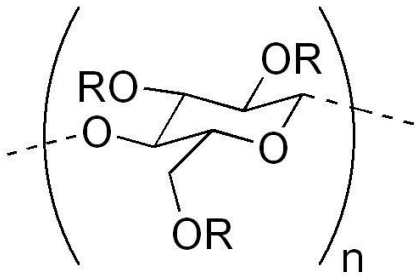

$$R = H \text{ or } CH_2CH(OH)CH_3$$

Fig. 9 Molecular structure of HPC

The main applications of HPC include the use as thickener, binder, emulsion stabilizer or surfactant polymer because of its solubility both in water and in non-polar solvents. Recent studies revealed that HPC contributes efficiently to the steric stabilization of some transition metal alkoxides during sol-gel hydrolysis and condensation [38]. It is also known that HPC can be used to reduce the sol-gel particle size and stabilize certain crystalline phases of some metal oxides, for example titanium or zirconium oxides [34,38,39].

HPC acts as a dispersant decreasing the VDWL attraction force between particles via chemisorption, i.e. the polymeric structure of HPC adsorbs dispersed micelles of the bulk sol reducing the interaction between the precursor particles. This allows that the ligands inside the micelle interact with the metal atom shortening the distance between metal atom and ligands. Therefore HPC can act as chelating and bridging agent as well because of its polar and nonpolar segments; it inhibits the agglomeration of particles and thus reduces the average particle size [38-43]. This stabilization can even persist until and beyond the heat treatment where the final metal oxide is formed. Monodipersed, submicron sized ZrO_2 particles required for manufacturing ZrO_2 ceramic components at lower sintering temperatures and minimum sintering time have been synthesized via sol-gel method [39]. The sol-gel technique applied in this investigation is used to synthesize nanocrystalline protective zirconium oxide coatings based on controlled hydrolysis and condensation of zirconium alkoxide in an alcohol solution, in the absence or presence of the polymeric steric stabilizer hydroxylpropyl cellulose [44].

III. Corrosion

1. General

In all fields of industry as well as in our everyday life we encounter corrosion phenomena [45]. It could be an old car as shown in fig.10, a piece of metal or a ship, but the consequence is always a deterioration of the material. Corrosion occurs because of the tendency of all materials to return to their lowest energy state which is usually the oxidized state. Not only metals are affected by corrosion though metal corrosion is the most common and important one [46]. For example a simple representation of a corrosion process is the chemical reaction of iron, water and oxygen:

$$Fe \quad + H_2O \quad + 1/2\,O_2 \quad \rightarrow \quad Fe(OH)_2 \tag{5}$$

Iron water oxygen ferrous hydroxide

In this reaction iron reacts with oxygen in water to form ferrous hydroxide. In case of steel and other iron materials this process is called “rusting”. It can be found on iron surfaces that are in contact with a wet and aerated medium. If any of these elements is absent, rusting will not occur.

Fig. 10 Corroded metal objects

Metal Corrosion can be understood as the result of an electrochemical reaction between an oxidant and a metal material. Different types of corrosion mechanisms have been found which are described in the following:

1.1 Uniform corrosion

Surface corrosion is one of the most important corrosion phenomena. It affects large areas of the metal surface as shown in fig. 11

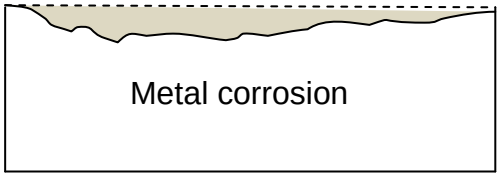

Fig. 11 Surface corrosion

The mechanism of this type of corrosion involves anodic and cathodic reactions. The corresponding anodic and cathodic areas of the metal surface change statistically in place and time resulting in an average uniform surface abrasion. It can be initiated by contact of the metal with oxygen and humidity. Uniform corrosion can be easily detected and avoided with cathodic protection or painting or other protective coatings. This form of corrosion affects steel and iron (rusting). It can be also seen on copper structures (green color).

1.2 Pitting corrosion

Pitting corrosion is a localized destruction of the metal. As intercrystalline or transgranular corrosion, pitting corrosion originates from local elements or local cells [47]. In the case of non-alloyed or low-alloyed steel the absence of oxygen in a small area generates a concentration gradient, resulting in the formation of anodic and cathodic sites.

On passivating metals such as aluminum pitting corrosion is initiated by aggressive ions like Cl^-, I^- or F^-. These anions are able to penetrate the protective oxide layer giving the electrolyte access to the metal surface.

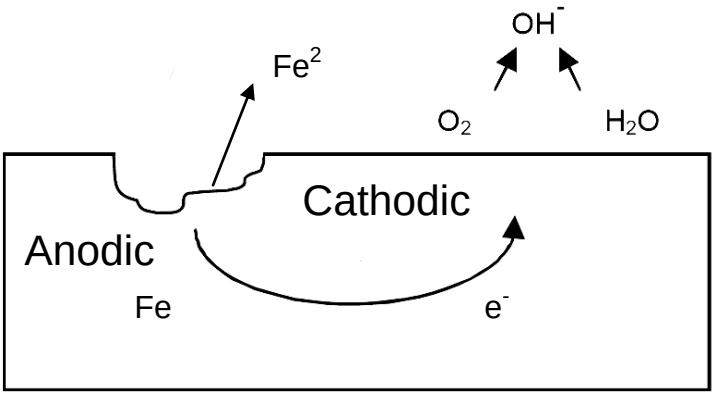

Fig.12 Schema of pitting corrosion

Pitting may be caused by an abnormal anodic site surrounded by a surface that plays the cathode role or by the vice versa process. Some literatures have coincided that four steps maybe occur during pitting corrosion:

a) Initiation which is caused by the local cell;

b) Propagation: at this stage the corrosion rate increases due to changes in the anodic and cathodic local cell;

c) The termination phase: characterized by corrosion products that precipitate on the cathodic surface and inhibit further corrosive attack and the last step: reinitiation: can occur when pits are rebuilt.

Metals which corrode uniformly are not prone to pitting corrosion [47].

1.3 Intergranular or intercrystalline corrosion

This is a localized corrosion form that begins at a narrow path or crack and proceeds along the grain boundaries of a metal. The mechanism is initiated by a potential difference between a thin particle boundary and the nearby adjacent bulk grain. This potential is usually a result of different chemical composition in the crystalline structure.

It can also be initiated by migration of alloy impurities into the grain boundary. When the concentration of impurities increases in a lateral portion of particles, a second phase may precipitate in the adjacent part and a local corrosion cell is developed which promotes intercrystalline corrosion [48].

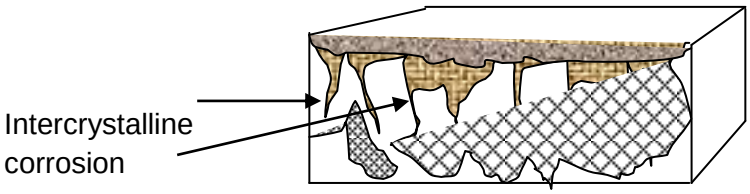

Fig.13 Effect of intercrystalline corrosion on particles boundaries

Intercrystalline corrosion is a common phenomenon on aluminium, copper and 18-8 stainless steel alloys. It can also be a consequence of heat treatment in alloy production because shape and size of the crystalline particles are affected by temperature, followed by a change of composition and concentration in grain boundaries. During the preparation of coatings based on metal oxides crystalline impurities and cracks can be the initiation of intergranular corrosion.

1.4 Galvanic corrosion

When two different metals are brought into electrical contact while they are immersed in an electrolyte the potential difference between them causes a current and ionic flow that result in the deterioration of the base metal.

The nobility of a metal, i.e. its resistance to corrosion and oxidation in moist air, can be derived from galvanic series. In these tables metals are classified on behalf of their potential against a standard reference electrode. (Table 1) [48].

Table1. Galvanic series of metals used in metallurgy [48]

Metallurgy	**Index (V)**
Gold, solid and plated, Gold-platinum alloy	0.00
Rhodium plated on silver-plated copper	0.05
Silver, solid or plated; monel metal. High nickel-copper alloys	0.15
Nickel, solid or plated, titanium an s alloys, Monel	0.30
Copper, solid or plated; low brasses or bronzes; silver solder; German silvery high copper-nickel alloys; nickel-chromium alloys	0.35
Brass and bronzes	0.40
High brasses and bronzes	0.45
18% chromium type corrosion-resistant steels	0.50
Chromium plated; tin plated; 12% chromium type corrosion-resistant steels	0.60
Tin-plate; tin-lead solder	0.65
Lead, solid or plated; high lead alloys	0.70
Aluminum, wrought alloys of the 2000 Series	0.75
Iron, wrought, gray or malleable, plain carbon and low alloy steels	0.85
Aluminum, wrought alloys other than 2000 Series aluminum, cast alloys of the silicon type	0.90
Aluminum, cast alloys other than silicon type, cadmium, plated and chromate	0.95
Hot-dip-zinc plate; galvanized steel	1.20
Zinc, wrought; zinc-base die-casting alloys; zinc plated	1.25
Magnesium & magnesium-base alloys, cast or wrought	1.75
Beryllium	1.85

Higher potentials indicate that the metal will corrode easier than metals with lower potentials. There are also more specified galvanic series described in the bibliography [48,49]. The mechanism of galvanic corrosion can be also used as corrosion protection. This principle of the “sacrificial anode” is widely used to protect ships or pipelines in seawater environment. The base metal acts as anode when it is in contact with the noble cathodic metal. The base metal will

corrode and dissolve while the noble metal is protected. This can decrease the corrosion process of the other metal for long time. For example, if small parts of zinc are connected to longer pieces of steel the zinc will corrode instead of steel [50]. However, very small anodic areas are undesirable because the material of the sacrificial anode would dissolve too quickly. This principle is used for cathodic protection. The figure 14, shows an example of galvanic corrosion where the less noble metal loses mass as effect of contact with a noble metal in a given electrolyte.

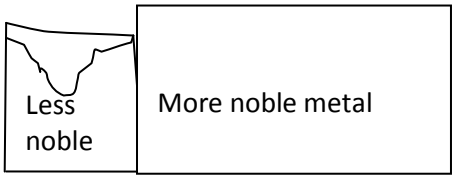

Fig.14 Example of galvanic corrosion

1.5 Bio-Corrosion

Microbial corrosion has attracted interest because it can do severe damage to both metallic and non-metallic materials. The corrosive damage is similar to other corrosion types and therefore the actual cause is often overlooked. The damage originates from metabolites of microorganisms that grow on the surface of the material in both aerobic and anaerobic environments. A typical biofilm is found on the surface which protects the microorganisms and promotes its growth as well. Such biofilm deposits can form concentration cells and may cause galvanic and pitting corrosion. Underground and underwater pipelines of oil- and gas-industry are often affected by this special type of corrosion.

Fig. 15 Steel corroded by microorganisms [51]

Sulfate reducing bacteria are able to generate hydrogen sulfide which reacts easily with iron or steel producing iron sulfide FeS and hydrogen. However, other sulfate–reducing bacteria oxidize the iron directly or by formation of sulfuric acid. These types of iron corrosion occur frequently in oil and gas industry where the products of biofilm generate sulfide stress cracking [51,52]. Even in anaerobic environments iron and steel can take damage without the presence of oxygen from bacteria such as *Desulfovibrio* or *desulfuricans.*

2. Passivation

Metals such as aluminum, zinc, copper or stainless steel have the ability to produce a natural and invisibly thin but dense oxide layer on their exposed surface, which separates the bulk metal from further attacks of the environment reducing this way the anodic reaction with movement of the potential further towards positive potentials [53].

Passivation can be also reached and even increased with an external current source. This process is called “anodizing” which is a common method for corrosion protection of aluminum. It means that at a specific current and potential have to be reached in order to inhibit the anodic reaction. Another example is phosphate conversion coatings to protect ferrous materials.

Passivation layers of nickel fluoride on nickel alloys such as “monel” allow handling of hydrogen fluoride or elemental fluorine.

3. Thermodynamics and kinetics aspect

3.1 Free standard energy

Gibbs free energy G determines the feasibility of a chemical reaction. A reaction can take place spontaneously when the difference of free energy is negative $\Delta G < 0$.

When a metal is exposed to a solution containing ions of the same metal, more ions will dissolve from the bulk metal into the solution and ions from the solution will be deposited on the metal surface in a reverse process. Finally, a state of equilibrium will be reached when the rates of dissolution and deposition equalize. In this state free energy is defined as:

$$\Delta G = \varphi \cdot \Delta Q \tag{6}$$

Energy is proportional to the charge flow ΔQ and the electrical potential (φ) which moves the charges. For an amount Δn of transferred material it can be expressed by the following equation:

$$\Delta G = E \cdot \Delta n \tag{7}$$

E is called electrical potential of the reaction. Each mole of a reacting species of valence z transports a charge of $Q = z \cdot F$. The change of Gibbs free energy per mole of a reacting species is proportional to the difference of electrical potentials ΔE and can be expressed with Faraday’s number F = 96485 C mol^{-1}:

$$\Delta G = -zF\Delta E \tag{8}$$

For the dissolution reaction of a metal $A_{red} \rightarrow A_{ox} + e^-$ free energy can be calculated as:

$$\Delta G = \Delta G^0 + RT \ln \frac{A_{ox}}{A_{red}} \tag{9}$$

Combination with equation (8) gives:

$$E = E^0 - \frac{RT}{zF} \ln \frac{a(M_{ox})}{a(M_{red})} \quad (10)$$

This equation is called the *Nernst Equation*. Free standard energy G^0 has been replaced by the standard electrode potential E^0 which is defined as the electrode potential of a reversible electrode at 298 K, an effective concentration of 1 mol/l and a gas pressure of 101300 Pa against standard hydrogen electrode (SHE) with E^0 = 0 V. The latter determines the reference point for all potential measurements. Because of the laborious handling of the SHE in practice other reference electrodes with known potentials are used. According to the Nernst equation the energy of an electrochemical reaction can be calculated and the feasibility of the reaction can be predicted on the basis of electrochemical potentials.

This principle can be demonstrated with the corrosion reaction of iron in deoxygenated acid solution [53]:

$$Fe + 2H^+ \longrightarrow Fe^{2+} + H_2 \quad (11)$$

This reaction can be described as an electrochemical cell:

$$Fe|Fe^{+2}\|2H^+|H_2 \quad (12)$$

The standard cell potential can be calculated from the difference of the individual reaction potentials:

$$\Delta E^0 cell = E^0 cathodic - E^0 anodic \quad (13)$$

By definition the cathodic hydrogen potential (SHE) is 0.0 V and the anodic potential of iron dissolution is -0.44 V [53]. The resulting cell potential is positive which means that the free energy becomes negative and therefore the reaction can occur as a spontaneous process.

Reverse non-spontaneous processes can be achieved with the application of external work induced by an external current source like it is done in electrolysis [53].

A corrosion reaction may occur spontaneously when stable products such as oxides or sulfides are built under release of energy. However, the analysis of thermodynamic data alone is not a sufficient criterion to decide about a possible corrosive threat. Even if a reaction can proceed spontaneously it may be hindered by a kinetic barrier and the reaction rate will be slowed down or even inhibited and no measurable change will occur. Examples are metals such as aluminum or titanium which develop a natural oxide passive layer which protects them against corrosive media [53].

3.2 Corrosion of Iron

Iron (Fe) is found in nature as a mixed oxidized material (hematite Fe_2O_3) or accompanied with sulfur as pyrite FeS_2. The metal can be obtained from its minerals by reversing the natural oxidation reaction. This can be achieved in a reduction process with carbon at high temperatures above 2000 K. The raw metal contains a high amount of carbon which can be removed in a purification procedure. The amount of carbon determines hardness as well as corrosion resistance of the final material. Besides carbon other alloy compounds such as nickel, chrome, tungsten or vanadium are used to design very hard, malleable or corrosion resistant alloys in the refining process of steel production. Because of the tendency of iron materials to return to their natural oxidized state they are very susceptible to corrosion when exposed to air and moisture, resulting in the formation of the well known rust [49, 52].

The corrosion of iron is a result of the contact between metal and oxygen in the presence of an electrolyte. Iron corrosion can be described as an electrochemical process of two partial reactions:

anodic reaction:

$$Fe \longrightarrow Fe^{2+} + 2e^{-} \quad (14)$$

The formation of iron hydroxide and iron oxide also known as rust encloses the following reactions:

$$2Fe^{+} + 4OH^{-} \longrightarrow 2Fe(OH)_2 \quad (15)$$

$$2Fe(OH)_2 + 1/2O_2 \longrightarrow Fe_2O_3 + 2H_2O \quad (16)$$

During this reaction the metal suffers a decrease of electron charge because of metal dissolution and consequently damage of the metallic structure. This anodic reaction is known as oxidation. In a complementary reaction hydrogen is developed from proton reduction:

cathodic reaction in neutral or weakly acidic electrolytes:

$$2H^+ + 2e^- \longrightarrow H_2 \quad (17)$$

The electrons released in the anodic reaction flow through the metal to the cathodic site while at the same time a transfer of positively charged ions occurs inside the electrolyte. In order to maintain the charge balance between electrons and cations the amount of transferred charge through the phase boundaries must be the same for anodic and cathodic reaction. This way the two reactions are linked to each other. The exchange rate of both reactions equates an exchange current density, which is strongly dependent on the electrode material and surface properties. Exchange current density has also a major influence on corrosion reaction rate which will be described in detail in chapter 3.3.

3.3 Effect of pH

Because proton reduction is a common cathodic reaction in most metallic corrosion reactions, the pH value is a crucial parameter in the investigation of corrosion phenomena. The corrosion potential can be calculated from the relationship between potential and ion concentration using the Nernst equation:

$$E = E^0 + \frac{2.3RT}{nF} \lg\left(\frac{a_{ox}}{a_{red}}\right) \quad (18)$$

The reduction of H^+ to H_2 is a thermodynamically feasible manner to incite the oxidation of Fe specifically in deoxygenated solutions. This fact indicates the importance of the H^+ concentration which is determined by the pH value:

$$E = E^0 + \frac{2.3RT}{nF} \lg a\left[H^+\right] \quad (19)$$

The activity of Fe can be considered one because it is in solid phase.

- *a* is the chemical activity of products or reactants (oxidation or reduction; ions or molecules)
- E is the measured potential
- E^0 is the standard electrode potential
- R is the ideal gas constant 1.986 calories/(mole K)
- T is the temperature in degrees Kelvin (K)
- n is the number of transferred electrons in the half reaction (e.g., n = 2 in Equation 9)
- F is the Faraday constant 96485 coulombs/equivalent or 23060 Kcalories/Volt
- $[H^+]$ is the concentration of dissolved hydrogen ions

An (equilibrium) phase diagram of an aquous electrochemical system where the corrosion or passivation phases vary according to the pH and potential is shown in fig.16. It is well known as Pourbaix diagram of iron corroding in 1M of acid solution [54]. pE values are obtained from reduction potentials by dividing E^0 by 0.059. Solid lines separate species attributed to acid-base equilibria. Line a shows the pH at which half of the 1M iron occurs as Fe^{3+} and half is precipitated as $Fe(OH)_3$. Solid double lines separate species related to redox equilibria (lines c & d). Likewise redox equilibria of species that do not contain hydrogen or hydroxide ions appear as horizontal boundaries (line b). However, species involving hydrogen or hydroxide appear as diagonal boundaries because they are in the part acid-base equilibria (line c).

Diagonal boundary lines from upper left to lower right represent basic solutions which tend to favor the more oxidized species. Longer dashed lines denote the theoretical region where water changes from oxidation to reduction (lines d & f) while shorter dashed lines enclose the practical region of stability of water (e & g).

Dashed line d represents the potential of water saturated with O_2 at 101,325 Pa (very well aerated water), above this potential water is oxidized to oxygen:

$$2\ H_2O + 4\ H^+\ (aq)\ O_2 + 4e^-\ E^o = +1.229\ V \qquad (20)$$

Dashed line e indicates the overvoltage of oxygen formation. Dashed line f represents the potential of water saturated with dissolved H_2 at 101,325 Pa pressure (high level or reducing agents in solution). Below this potential water is reduced to hydrogen:

$$2\ H^+ + 2\ e^-\ E^o = +1.229\ V \qquad (21)$$

In practice, an overvoltage effect prevents significant release of hydrogen until the lower dashed line g is reached [54].

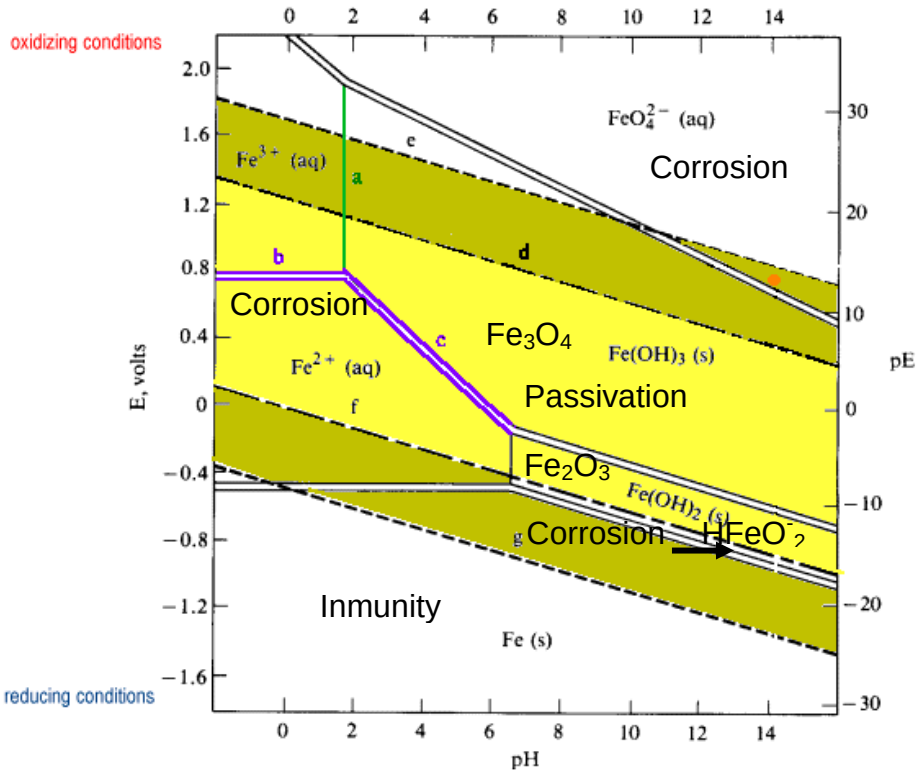

Fig. 16 Pourbaix diagram for iron [54]

It is observable that for applied potentials less than -0.6 Volts iron will not corrode except for high pH more than 8. However at positive potentials above -0.6 V iron will corrode with different products depending of the pH conditions. It

is also important to see that iron forms a passive layer at different pH and potential ranges which can protect the metal from oxidation. This principle is applied to generate a passive layer on the metal to prevent the corrosion through cathodic and anodic protection.

3.4 Kinetics aspects of corrosion processes

As mentioned before, thermodynamic data provide information about the possibility of a spontaneous reaction. But the actual susceptibility to corrosion can only be estimated with the consideration of kinetic effects.

The anodic reaction of iron dissolution is:

$$Fe \rightarrow Fe^{2+} + 2e^{-} \quad (14)$$

The reaction rate of this reaction can be expressed as:

$$v = K_{corr}\, c(Fe) \quad (22)$$

rate constant K as well as reaction rate v are proportional to the corresponding current density i_{corr} on the electrode surface:

$$v \propto i_{corr} \quad (23)$$

K_{corr} also depends on temperature. This is described by the *Arrhenius*-Equation:

$$K = K^0 \cdot e^{E_A/RT} \quad (24)$$

K is the rate constant for the chemical reaction and the units are time reciprocal, K^0 is the theoretical maximum reaction rate if all reactants would react completely spontaneous. But only a small part of all reactants possesses the necessary activation energy E_A which is expressed by the exponential part of the formula. R is the gas constant and T the absolute temperature in Kelvin's degree. An increase of the temperature will increase the reaction rate.

In analogy to the *Arrhenius-Equation* the current densities can be expressed as:

$$i = i_0 * \exp\left\{\frac{\alpha \cdot n \cdot F \cdot \Delta E}{R \cdot T}\right\} \quad (25)$$

In this equation the constant *K* and K^0 of the reaction rate where substituted by *i* and i_o (current density and maximal current density at equilibrium, respectively). The term α is a proportional factor for charging step which lies usually around α = 0.5 generally. Activation energy is represented by the term from the equation (8) *zFΔE.*

This equation can be applied to both the anodic and cathodic reactions i_a and i_c:

$$i_a = i_0 * \exp\left\{\frac{\alpha nF\Delta E}{RT}\right\} \tag{26}$$

$$i_c = i_0 * \exp\left\{-\frac{(1-\alpha)nF\Delta E}{RT}\right\} \tag{27}$$

Next to the equilibrium both reactions overlay and the resulting current density is the sum of the current densities of both reactions:

$$i = i_0 * \left[\ \exp\left\{\frac{\alpha nF\left(E - E_{corr}\right)}{RT}\right\} - \exp\left\{-\frac{(1-\alpha)nF\left(E - E_{corr}\right)}{RT}\right\}\ \right] \tag{28}$$

E_{corr} is the corrosion potential.

This formula which relates the current density of interfacial reaction with both applied potential and E^0 for each specific system is the *Butler-Volmer* equation [49].

In the study of corrosion processes the determination of the corrosion rate is a very important parameter which is directly proportional to the interchange current density at equilibrium or open circuit potential (OCP):

$$i_o = i_{corr} \propto k \tag{29}$$

k is the corrosion rate, i_o is the measured current and i_{corr} the current at no applied potential.

This equation can be therefore applied to experimental determination of corrosion rates.

4. Corrosion protection

The worldwide corrosion cost encloses every year billions us dollars equivalent to approximately 3 % of the world´s gross domestic product [50].

Different methods have been developed to manage this problem.

Cathodic protection

An external negative potential is applied to the metal making it nobler or immune. The ultimate objective is to suppress all current flowing from the anode in a corrosion cell. This technology uses an external electrical circuit or attaches a sacrificial anode which dissolves instead of the metal that has to be protected. This will result in a cathodic rather than anodic behavior on these surfaces.

Anodic protection

In this technique a passive layer is generated on the metal surface by application of a positive potential by an external power supply. Control of pH-value and potential is crucial to avoid accidental increase of corrosion when the potential shifts into the active dissolution region. The main advantages of this method are: a) low current requirements; b) efficient reduction of corrosion rates; and c) applicability to certain strong, hot acids or other highly corrosive media [51].

Both methods are used in the industry but actually cathodic protection is the most important. They are used for example in the sheathing of pipelines in seawater or underground, protection of ship hulls, tubings and many others.

Inhibitors

The use of inhibitors or additives is very common in oil and natural gas industry. These implement corrosion inhibitors such as sodium nitrite, aldehydes, and hydrazine. In most cases they help to produce a thin passive layer on the metal surface to prevent corrosion. The major corrosive agents that come with natural gas and oil are hydrogen sulfide and carbon dioxide. The concentration of inhibitors has to be controlled very thoroughly, because some of them like nitrite can also produce pitting corrosion [54].

Protective coatings

Another solution against corrosion is the deposition of a protective film onto the metal surface which separates the material from the aggressive environment.

Various deposition techniques have been developed for different coating materials and applications. For example thin films of diamond-like carbon are used to protect sensitive data storage media such as hard disks against corrosive and mechanical damage [55]. The use of thin protective films (< 1µm) has also proved to be an interesting alternative with low cost [55]. Transition materials and silicon coatings provide many types of thin protective coatings [4,6,57,58].

5. Protection by sol-gel coatings

5.1 Protective metal alkoxide coatings

The application of metal alkoxides as a precursor for protective metal oxide films has been investigated extensively over the last decades. In the special case of iron and steel the most promising oxide-based materials are zirconium propoxide or isopropoxide, titanium propoxide or ethoxide, aluminum propoxide, vanadium pentoxide, niobium propoxide, etc. The oxides formed with these compounds have proven good adhesion, reflectivity or UV protection, hydrophobic behavior and corrosion protection [44,59-61]. Metal alkoxies have the property to react quickly with water by hydrolysis and when a partial hydrolysis and polycondesation are reached, clear gels can be produced. That way after appropriate deposition and heat treatment ceramic-like films can be formed with very favorable properties such as high hardness, homogeneity and density [20,62]. Due to the high reactivity of metal alkoxides, the use of modification agents is necessary to control the rate of hydrolysis and condensation. That way it is also possible to design specific properties of the final coating.

Metal alkoxides are very potent precursors for the preparation of protective coatings because they promote a relative stable structure. β-diketones, carboxylic agents, amines or surfactants are frequently used as modifiers which

provide either chelating and bridging or additional functionality in the precursor molecule. This way stable bonds are formed between metal and hydroxyl or oxo ligands which turn into metal–oxygen–metal bonds after heat treatment. Consequently, protective ceramic-like films are generated with low porosity, better temperature resistance, high hardness, hydrophobicity and resistance against corrosive attack. It must be mentioned that the reaction mechanism of metal alkoxies is complex and it needs careful preparation. However various fast, easy and cheap deposition techniques at low temperatures make them a very interesting and promising alternative for the production of ceramic-like coatings.

5.2 Hybrid metal oxide films

The composition of sol-gel coatings can be altered from pure inorganic to almost organic, resulting in a huge spectrum from very hard to soft, polymer-like materials. New classes of materials are available that are not accessible in traditional ceramic synthesis methods. These so called ”hybrid materials” are a combination of inorganic and organic structures, where the inorganic part supplies mechanical stability while the organic part promotes highly branched networks and flexibility. For example the addition of zirconium precursors to titanium films provides a much higher resistance against corrosion and temperature. Alkyl- or aryl- substituted trialkoxysilanes can increase the hydrophobicity of the final coating. It can be also enhanced adding molecule of fluorinate. Toughness and scratch resistance can be improved with the use of hard nanoparticles in some polymers [30]. Silicon coatings are often combined with zirconium-based materials to increase the adhesion on metallic substrates. Inorganic gels could present better stability and performance if either organic or biomolecules are included.

5.3 Zirconium oxide- base films

As a transition element with an incomplete d sub-shell (allows multi ligands connections) zirconium is an excellent precursor for applications against corrosive and temperature damage. In the other hand, zirconium oxide ZrO_2 (Baddeleyite) is the most occurring mineral of this metal with a monoclinic

crystal phase. Zirconium oxide can occur in tetragonal and cubic phase, but it needs high temperatures to obtain those phases. During the heating and cooling processes cracks may occur in the final coating due to volume expansion during phase transition [56]. Therefore it needs either to be combined with other metal oxides like: calcium, magnesium, yttrium, cerium, etc. or other additives to stabilize the crystalline structure. The resulting material is hard, decorative, and crystalline with numerous applications [24,63]. Another interesting property of this metal is its thermal expansion coefficient (5.7 $\mu m \cdot m^{-1} \cdot K^{-1}$) which is close to that of iron (11.8 $\mu m \cdot m^{-1} \cdot K^{-1}$) and titanium (8.6 $\mu m \cdot m^{-1} \cdot K^{-1}$), respectively. This aspect is used to prepare individual or hybrids coatings of zirconium and titanium oxide on iron or steel against corrosion, because of its excellent adhesion [30,44].

There are other different ways to make ZrO_2 from zirconium precursors: via vapor phase deposition or reduction/oxidation at high temperature in a furnace, plasma, electrochemical deposition, electron beam, etc [63-67]. Gels derivable from compounds of zirconium can be obtained for example by neutralization of chloride or nitrate precursors with urea or by peptization [4,6]. An alternative way is the fragmentation of zirconium *tert*-butoxide molecules at high temperatures in oven via *pyrolysis* [4]:

$$Zr(C_4H_9)_4 \longrightarrow ZrO_2 + \text{alcohol} + \text{olefin} \qquad (30)$$

The problem of zirconium precursors is the low electronegativity of zirconium in the last electron shell. Therefore precursors of this metal react very quickly with water via hydrolysis forming crystalline precipitates. However the gel structure remains unknown until now [4,68].

IV. Electrochemical methods on corrosion characterization

1. Linear polarization resistance

1.1 Double layer and Butler –Volmer equation

Changes of the equilibrium potential of electrochemical reactions generate a polarization on the metal electrode. Because the Nernst Equation does not

relate electrical currents with electrochemical reactions, other principles such as Ohm's have to be considered:

$$V = IR \tag{31}$$

It states that an electrical voltage (V) is equal to the product of electrical resistance and (R) electrical current (I).

When a metal electrode is exposed to an electrolyte and an external potential is applied, an electrical current will be generated. When a metal is exposed to an electrolyte ions leave their lattice while electrons are left behind. The metal ions are surrounded and shielded by water molecules. These hydrated ions are attracted by the negative surface charge of the electrode surface and a potential is developed between surface and ion layer in the near surface region. This layer containing metal ions, water molecules and bulk electrolyte is known as electrical double layer (EDL) [46].

When the EDL is in equilibrium the rate of metal ions leaving the metal surface is the same as the rate of ions being reduced and re-deposited in the lattice. But when the equilibrium is disturbed a net current will be generated, resulting in a mass transport through the phase boundaries. In the case of corrosion reactions the metal will be oxidized. Such a disturbance can be produced by an external potential resulting in a characteristic response of the metal electrode. This method is the basis of various electrochemical techniques that can be used for the investigation of corrosion phenomena on metallic surfaces.

The relationship between electrical current and potential change is given by the Butler-Volmer equation:

$$i = i_0 * \left[\exp\left\{\frac{\alpha n F\left(E - E_{corr}\right)}{RT}\right\} - \exp\left\{-\frac{\left(1-\alpha\right) n F\left(E - E_{corr}\right)}{RT}\right\} \right] \tag{18}$$

When the overpotential ($E-E_{corr}$) is very small, the exponential function can be expressed as a power series which can be terminated after the first element:

$$e^x = \sum_{n=0}^{\infty} \frac{x^n}{n!} = 1 + x + \frac{x^2}{2!} + \frac{x3}{3!} + \frac{x^4}{4!} + ... \tag{32}$$

This allows a simplification of the Butler-Volmer equation:

$$i = \left\{ \frac{i_0 \alpha n F \left(E - E_{corr}\right)}{RT} \right\} \quad or \quad \Delta E = \frac{RT}{nFi_0} * i \tag{33}$$

For very low variations of the potential ΔE < 0.01 V the term $\frac{RT}{nFi_0}$ represents a resistance similar to Ohm's law which is well known as polarization resistance (R_p):

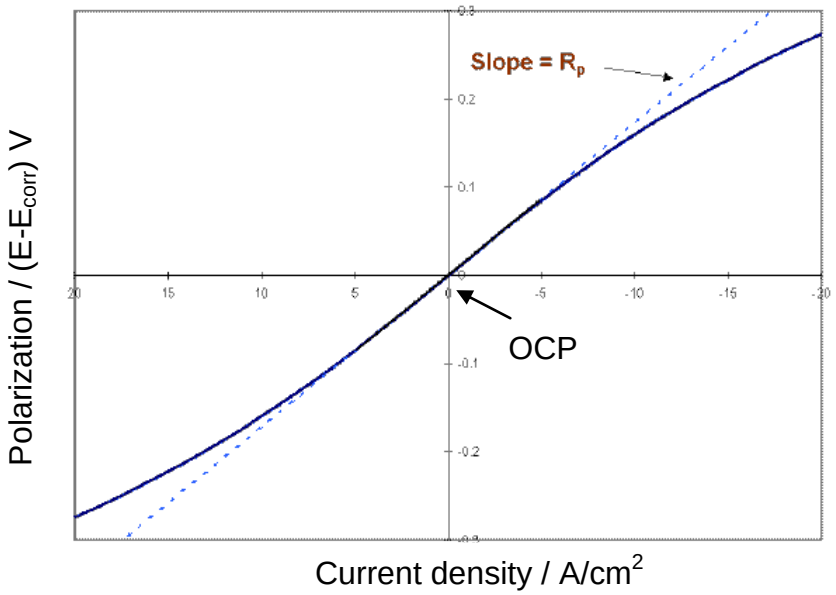

Fig. 17 Voltage-Current density Polarization resistance [55]

The slope of the line is the change of the potential Y-values divided by the change of its X-values, which is the polarization resistance:

$$Rp = \frac{\Delta E}{\Delta i} \tag{34}$$

The range of linear dependence of current on the applied potential (fig.17) is described by a corroding electrode (anodic and cathodic reactions) because of small deviations produced on the Tafel slopes. This linear dependence can be explained as a simple difference between two logarithmic functions of current approximated to a linear function when the logarithmic functions are of the same order of magnitude, as described by *Stern and Geary* [70,71].

At a range from - 20 mV to +20 mV from the open circuit potential OCP (fig. 18), it is possible to calculate R_p from the measured current-potential plots.

1.2 Stern-Geary equation and corrosion rate

Apart from R_p values other useful information can be obtained from polarization measurements. For example the corrosion current can be converted into a corrosion rate or depth penetration. A mathematical relationship between corrosion resistance and corrosion current was developed by Stern and Geary. It allows the calculation of corrosion rates from linear polarization data:

$$R_p = \frac{B}{i_{corr}} \tag{35}$$

where:

$$\mathrm{B} = \frac{\beta a \cdot \beta c}{2.303(\beta a + \beta c)} \tag{36}$$

$$i_{corr} = \frac{\beta a \cdot \beta c}{2.303 Rp, E_{corr} 2.303(\beta a + \beta c)} \tag{37}$$

- i_{corr} is the corrosion current density in A/cm^2
- Rp is the polarization resistance in Ohms·cm^2
- β_a is the anodic Tafel slope in V/decade of current density
- β_c is the cathodic Tafel slope in V/decade of current density

Tafel slopes can be obtained from Tafel-plots (see chapter 2).

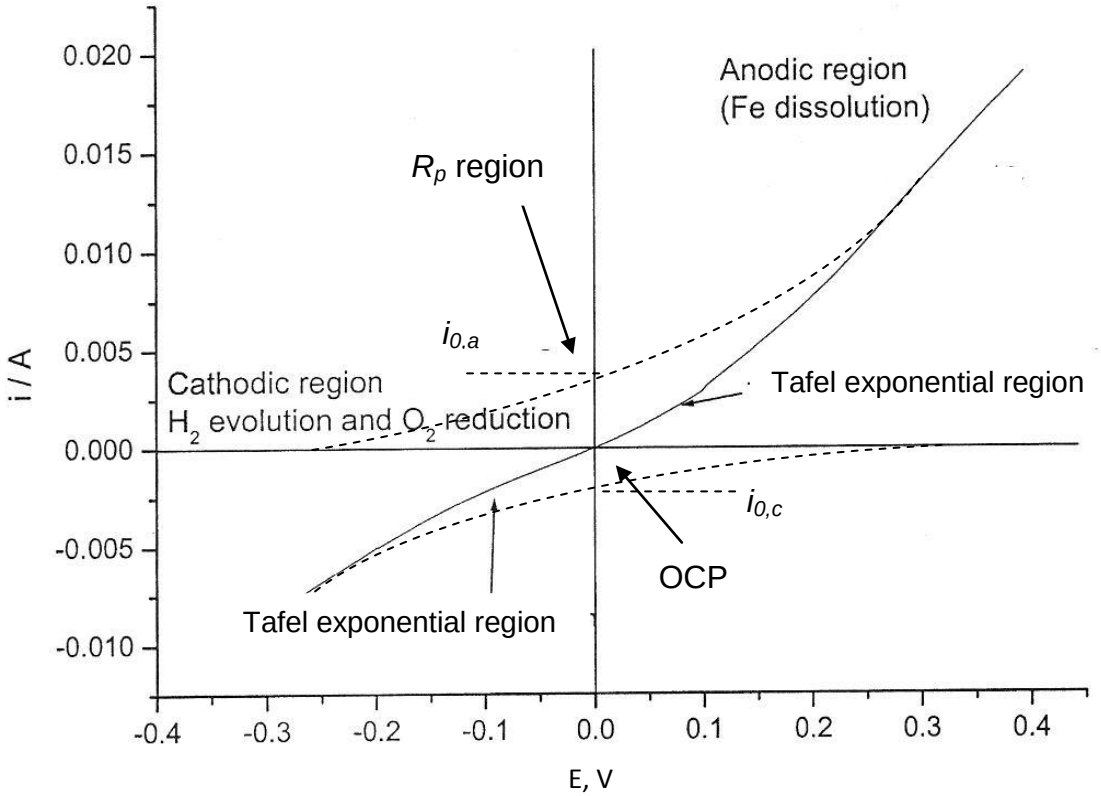

Fig. 18 Current density-Potential curve for a reaction in equilibrium [69]

The corrosion rate can be converted into an abrasion rate by *Faraday´s* law, or by the next equation:

$$MPY = i_{corr}(\Lambda)(1/\rho)(\varepsilon) \tag{38}$$

- MPY is the corrosion rate in mils/years (mpy)
- Λ is a conversion factor of 1.2866x10^5 [equivalents·s·mils] / [Coulombs·cm·years]
- i_{corr} with the unit A/cm^2 (1 A = 1 Coulomb/s)
- ρ is the metal density in grams/cc
- ε is the equivalent weight in grams/equivalent (the metal´s molar weight in gram divided by the number of electrons transferred in a half anodic reaction) [46]

Conversion tables are available for different materials for an easy corrosion rate calculation:

Table 2. Current and corrosion rate conversion factors for iron and steel [46]

Iron and steel	Corrosion current	Penetration rates	Penetration rates	Mass loss
	mA cm^{-2}	mm $year^{-1}$	mpy	g m^{-2} day^{-1}
mA cm^{-2}	1	11.6	456	249
mm $year^{-1}$	0.0863	1	39.4	21.6
mpy	0.00219	0.0254	1	0.547
g m^{-2} day^{-1}	0.00401	0.0463	1.83	1

2. Tafel Plot

Tafel plots measurements use the same principle as linear polarization except for a wider potential range between - 200 mV and + 200 from OCP as shown in fig.19. Additionally, it delivers more information than linear polarization experiments. The currents of anodic and cathodic branches are defined by the Butler-Volmer equation as:

$$i = i_{corr} * \left[\exp\left\{\frac{\alpha n F\left(E - E_{corr}\right)}{RT}\right\} - \exp\left\{-\frac{(1-\alpha) n F\left(E - E_{corr}\right)}{RT}\right\} \right] \quad (39)$$

At very high overpotentials Δ*E*≥ 50 mV one part of the equation becomes insignificant. This means that an electrode with an anodic overpotential beyond +50 mV can be considered to show purely anodic behavior. This applies also for cathodic behavior with negative overpotenials of ≥ -50 mV. In this region the two branches can be described in logarithmic scale as:

$$\log i_a = \log i_{corr} - \left\{\frac{\alpha n F\left(E - E_{corr}\right)}{2.3RT}\right\} \text{ at anodic potential} \quad (40)$$

$$\log i_c = \log i_{corr} - \left\{-\frac{(1-\alpha) n F\left(E - E_{corr}\right)}{2.3RT}\right\} \text{at cathodic potential} \quad (41)$$

This relationship allows the extraction of corrosion rates from the linear parts of anodic and cathodic branches of Tafel plots which occur around ± 50 mV from OCP (fig. 19):

$$\Delta E = \beta \cdot \log\left|\frac{i}{i_{corr}}\right| \tag{42}$$

In this equation the term β represents the anodic reaction $\beta_a = \frac{2.3 \cdot RT}{\alpha nF}$ and in case of the cathodic reaction $\beta_b = \frac{2.3 \cdot RT}{(1-\alpha)nF}$. Both terms are the Tafel-slopes of both partial electrochemical reactions. This calculation is well known as *Tafel-fit*.

There are two types of Tafel plots that can be observed:

a) Activation controlled: when the corrosion rate is determined by the rate of metal ions passing over into the electrolyte.

b) Diffusion controlled: when the corrosion rate is determined by the transport of the reacting species to and from the metal surface.

Fig. 19 shows an example of Tafel plots for activation controlled reactions. In these experiments a three-electrode setup must be used and the potential scan rate should be slow to establish equilibrium conditions. Therefore plotting log IiI vs. E for both half reactions allows the extrapolation of anodic and cathodic slopes which appear as straight lines in fig. 17. The intersection gives log i_{corr}.

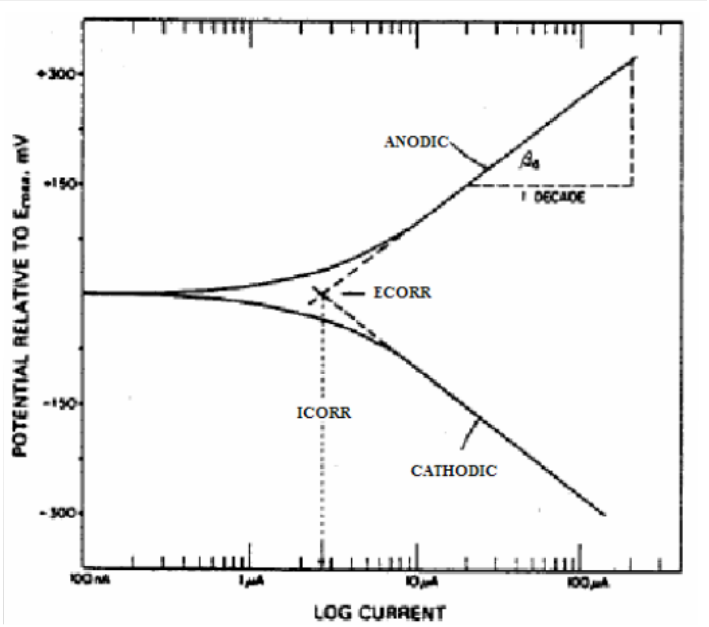

Fig. 19 Tafel fit indicating the slopes of anodic and cathodic reactions [69]

In the case of diffusion control the corrosion current is the diffusion current when cathodic current remains constant at decreasing potentials [46,69].

With the values of density and equivalent weight and using Rp both i_{corr} and corrosion rate can be calculated with equation 38 or by using corresponding software.

3. Cyclic voltammentry and potential scans

The last chapters described electrochemical methods such as linear polarization that provides information about corrosion rates in a very small potential range. Tafel plots provide corrosion rate and kinetic information as well in a wider potential spectrum. This chapter will illustrate how even more information can be gained from a further increased potential range in potentiodynamic scanning (PDS) or cyclic voltammetry (CV) experiments.
Both techniques are carried out in a typical three electrode setup as shown in fig. 20.

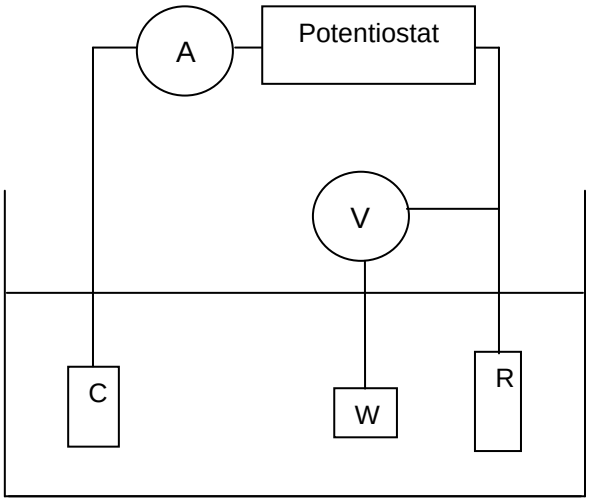

Fig. 20 Electrochemical cell for cyclic voltammetry measurements
(C: counter electrode; W: working electrode and R: reference electrode)

Potentiodynamic scanning is based on a linear potential waveform; i.e., the potential is changed as a linear function of time. The rate of change is called scan rate.

The simplest technique used in this method is Linear Sweep Voltammetry (LSV). The potential range is scanned starting from an initial potential and ending at the final potential. The wide potential spectrum covers the cathodic range from several hundreds of mV in negative direction from OCP and a large anodic area up to e.g. 1000 mV from OCP as well. Therefore a lot of information can be extracted from the plots about the corrosion behavior, dissolution current densities in the active region, formation of passive layers and transpassive oxidatin, etc. CV is an extension of LSV where the direction of the potential scan is reversed at the end of the first scan (the first Switching Potential), and the potential range is scanned again in the reverse direction. A typical current density-potential plot is shown in fig. 21.

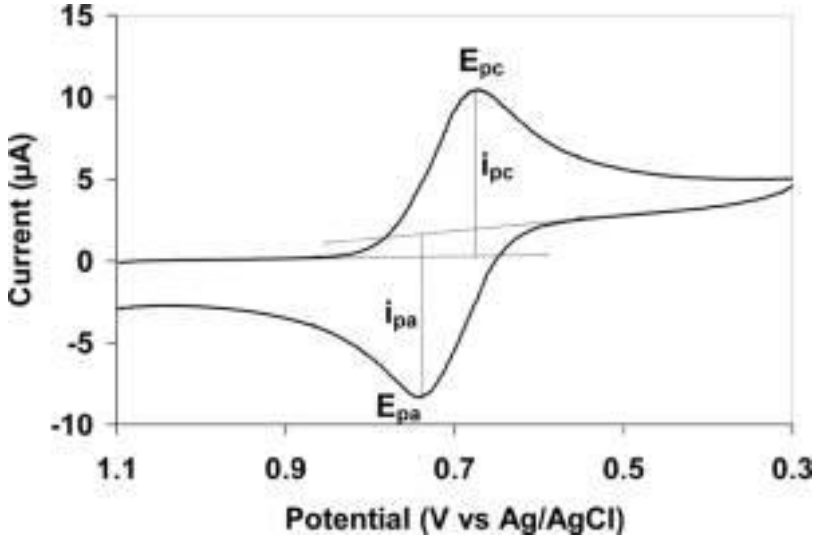

Fig. 21 Foward sweep and reverse cycle (Potentiogram) [72]

I_{pa}, E_{pa} and i_{pc} and E_{pc} are the maximun current density and the corresponding potential at the anodic and cathodic area, respectively. The reverse cycle usually does not show the same behavior and amplitude as the foward sweep. It depends on the scan rate, reversibility of oxidation and reduction reactions, electrolyte concentration, surface roughness and the velocity of charge transfer into the electrolyte. Often it shows a positive or negative hysteresis indicating that pitting corrosion is either initiated or a damaged passive film is repaired [73].

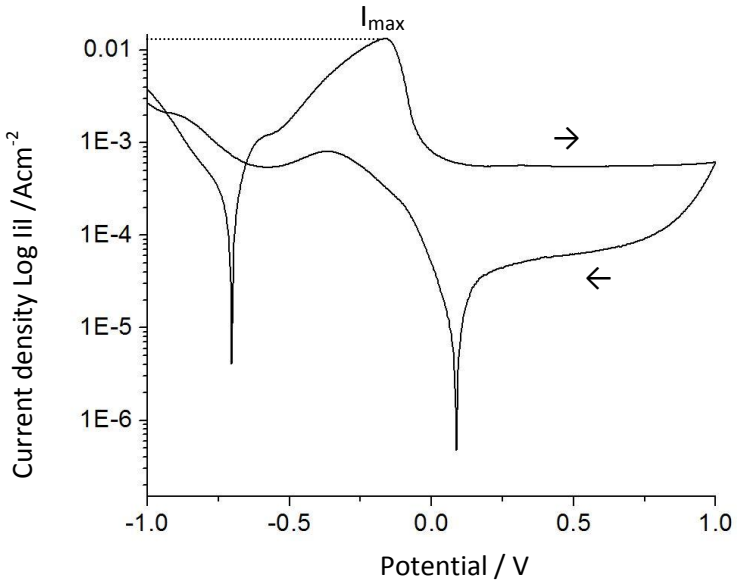

Fig. 22 Foward sweep and backward cycles of iron

Cyclic voltammetry can be used to predict the long term behavior of a sample which has to bare oxidizing and reductive potentials over and over with each cycle. Although typical data like pitting potentials and dissolution current densities are not intrinsic properties of the material, they can be used to compare different samples to investigate film porosity and corrosion resistance as long as any other parameters of the system are kept constant. The average film porosity of a coated sample can be measured for instance, when it is compared with an uncoated reference sample and a higher coating porosity will result in higher current densities [23,24]. I_{max} expresses the maximum iron dissolution rate before the passive film formation starts at higher potentials. Also the shift of OCP can be an indicator for a change of porosity when the coating material is electrochemically inert [23,24].

4. Electrochemical impedance spectroscopy

4.1 Measure principle

In electrochemical impedance spectroscopy (EIS) the samples are polarized with a range of low magnitude voltages at different frequencies. The change of

amplitude and phase of the current response of the observed system is recorded and from this data the impedance is calculated on the basis of an appropriate equivalent circuit. This circuit is a theoretical model that describes the investigated system as a sum of electro-technical components such as capacitors, resistors and inductors. The major problem of EIS is the fact that the equivalent circuit has to match the measured system perfectly in order to receive reliable data. On the other hand this method provides information about corrosion behavior, corrosion rates, diffusion and coating properties in a fast and non-destructive way [46,74-76].

Due to the sinusoidal shape of the AC signal the mathematical calculation may be difficult. However, because of the small excitation signal (amplitude between 5 and 10 mV) the response of the electrochemical cell is pseudo-linear, that is a sinusoid at the same frequency but shifted.

The mathematic form for a sinusoidal signal is:

$$E_t = E_s \sin(wt) \tag{43}$$

E_t is the potential at time t, E_s is the amplitude of the signal and (*w)* is the radial frequency which is also known as w = 2πf in Hertz.

The pseudo-linear response of the system will be measured at the phase angle (Φ) as current:

$$I_t = I_s \sin(wt + \phi) \tag{44}$$

Using Ohm's law from equation 30 and assuming that impedance (Z) is analogous to a resistance:

$$Z = E_t / I_t = \frac{E_s \sin(wt)}{I_s \sin(wt + \phi)} = Z_s \frac{\sin(wt)}{\sin(wt + \phi)} \tag{45}$$

It is known that for bigger excitation signals the impedance can be written as a complex function [46,77]:

$$E_t = E_s \exp(jwt) \tag{46}$$

$$I_t = I^0 \exp(jwt + \phi) \tag{47}$$

$$Z(w) = E / I = Z_s \exp(j\phi) = Z_s(\cos\phi + \sin\phi) \tag{48}$$

Z(*w*) is the impedance of the system and it is the sum of a real and an imaginary magnitude. It can be expressed in absolute values as a vector function in a so called Nyquist plot (fig. 23). Y axis depicts the imaginary component and the X axis contains the real part. Absolute impedance IZI can be obtained for each frequency from the angle between both parts.

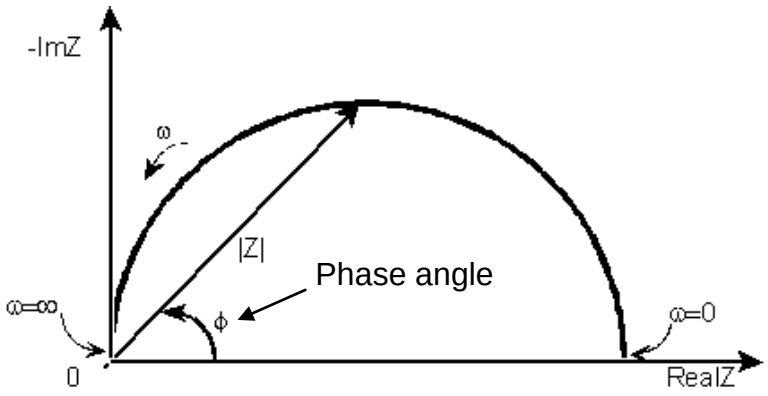

Fig. 23 Nyquist plot with impedance vector [77]

There is another common form to graph EIS data. It is called Bode-plot where the total impedance or phase angle Φ is plotted at logarithmic scale on the Y-axis vs. the logarithm of frequency on the X-axis. A corresponding Bode-plot for the above diagram is shown in fig. 24

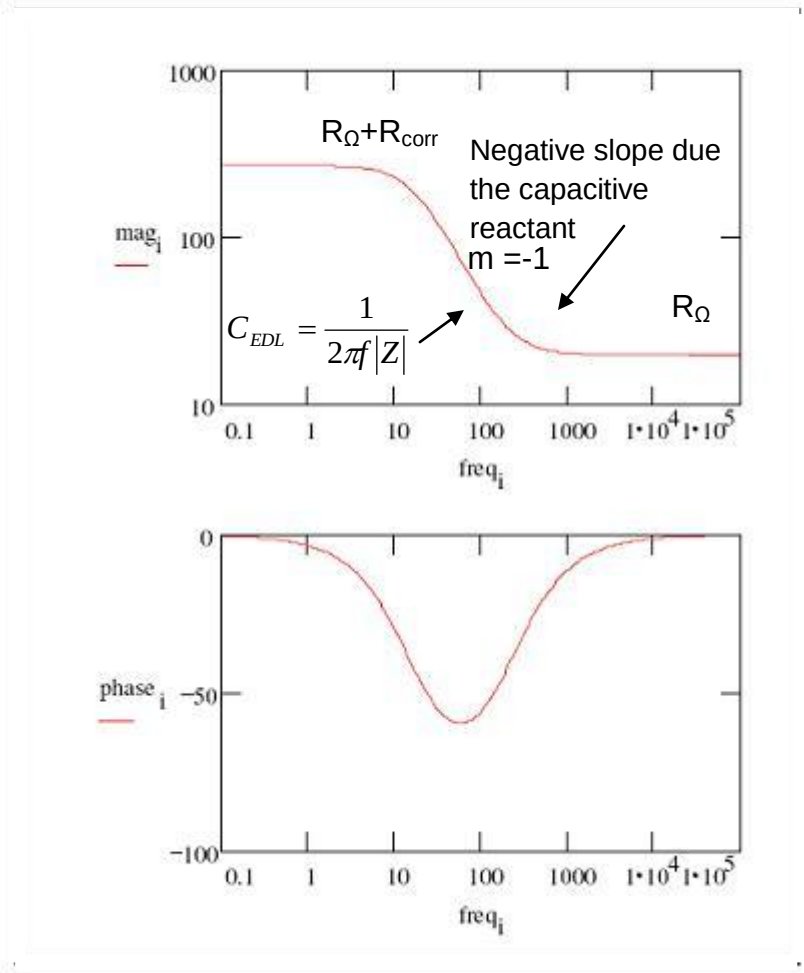

Fig. 24 Bode-plot for a single time constant

4.2 Physical representation of impedance

It is necessary to use equivalents electrical circuits for analysis of impedance measurements and to relate them with physical phenomena:

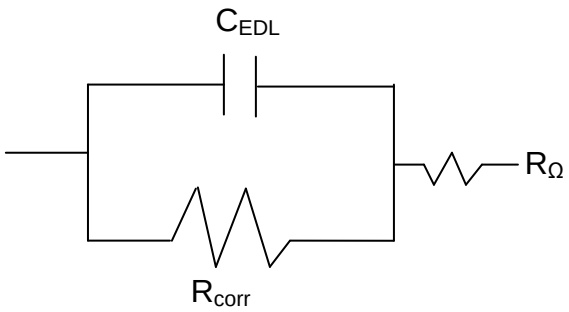

Fig. 25 Simple electrical circuit for uncoated metal

Electrical equivalent circuit model in fig. 25, also known as Randles cell, represents a metal submerged in an electrolyte with an electrical double formed at the surface. The capacitor (C_{EDL}) corresponds to the capacity of the electrical double layer to be charged or discharged, R_Ω is the solution resistance and R_{corr} is the polarization resistance or the resistance of the metal to the transfer of active species into the electrolyte.

This circuit appears always as a semi circle in Nyquist plot. In fig. 23 the solution resistance can be found in the real axis value at the high frequency intercept (next to the origin). The lowest frequency (right hand side of the plot) represents the sum of solution resistance and polarization resistance, i. e. the polarization resistance Rp. The Nyquist plot does not allow an estimation of the capacitance which can be obtained from the Bode plot. The slope is zero when the polarization is caused by a resistance and it is negative when it is caused by a capacitance. The slope (m) can be calculated by the ratio of Rp or R_{corr} and R_Ω and approaches -1 when the ratio increases [46,77]. Therefore extrapolation of the slope line and intercepting it with the frequency w allows the calculation of the capacitance as shown in fig. 24.

4.3 Equivalent circuit for coated metal

When a coated metal is exposed to an electrolyte active species may diffuse through pores inside the film material to and from the metal surface. This can produce a new interface where corrosion processes can occur. This highly complex behavior has been studied for years on the basis of different equivalent circuits and researchers still do not agree about the interpretation of impedance data and the physical processes [77]. Because of the different opinions about this system only the most common electrical circuit for coated metals will be shown here and it is displayed in the fig. 26.

In a quasi-perfect pore free coating impedance consists of a parallel circuit containing the capacitance C_{coat} and the coating resistance R_{coat}:

$$Z(jw) = \frac{R_{coat}}{1 + jwR_{coat}C_{coat}} \tag{49}$$

A capacitance is defined as two conducting plates are separated by a nonconductive medium known as dielectric [46]. The capacitance magnitude depends on parameters like distance, size and dielectric properties and it can be calculated from:

$$C_{coat} = \frac{\varepsilon \varepsilon_0 A}{d} \tag{50}$$

ε is the relative electrical permittivity; ε_0 is the electrical permittivity in vacuum, considering the plate to be the exposed coating surface, A is the surface of one plate and d is the coating thickness. Reference values of ε are predicted for different materials: vacuum 1; water 80.1 (293 K); organic coating = 4 – 8 [46]. When the coating is free from pores the resistance disappears [57] and only the capacitance will be measured.

However, usually after some time electrolyte will diffuse into the coating structure and because ε of the coating material is lower than ε of water, the coating resistance will decrease and can be measured. It is supposed that a pocket will be formed where the electrolyte solution concentration is different from the bulk solution. This interface zone between the blank metal and the electrolyte is considered as a double layer capacity (C_{edl}) in parallel with the electrochemical transfer reactions.

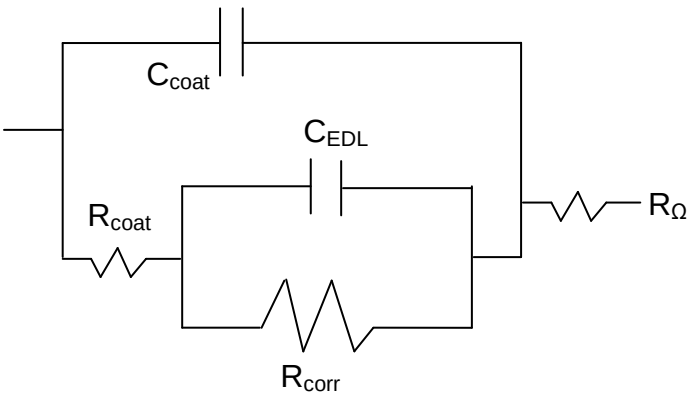

Fig. 26 Equivalent electrical circuit for coated metal

According to literature much more information can be obtained from Nyquist and Bode plots when two time constants are used [78-80]. There are also other aspects to be considered like mixed kinetic and diffusion control (Warburg impedance) which are not discussed in detail here. Finally the value of polarization resistance can be used to calculate corrosion rate according to the Stern-Geary equation as described before.

B. Experimental

I. Samples preparation

1. Polishing process

Pure iron rods (99,8%) were cut into round cylindrical slides (29 mm in diameter x 3 mm thick). They were ground with silicon carbide paper by different steps (180, 320 and 1200 mesh), using the parameters presented in the following table.

Table 3. Polishing parameters

Step	Polishing material	Mesh size	Solution	Time(min)	Force	Speed
1	SiC Paper	P320	Water	3 min	30 N	300 Rpm
2	SiC Paper	P1200	Water	3 min	30 N	300 Rpm
3	Micro Floc	MetaDi Supreme 3 µm	Dialub SW	3 min	15 N	180 Rpm

Finally they were polished with a 3 µm polycrystalline diamond suspension to reach a reproducible mirror-like surface as shown in fig. 27.

In order to remove the rest of impurities from the samples surface, they were dried under warm air and afterwards degreased and cleaned with technical iso-propanol for 20 seconds in an ultrasonic bath between each step.

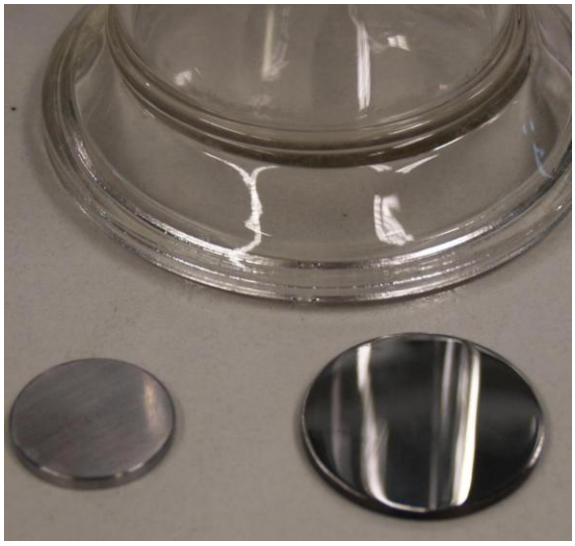

Fig. 27 Rough and mirror–like polished iron sample

2. Sol preparation

2.1 Zirconium n-propoxide-acetyl acetone sols

Films were prepared from a precursor solution of zirconium n-propoxide (70% in n-propanol). 2.5 ml of this solution were filled with a syringe into a beaker that had been cleaned with iso-propanol and dried with warm air. Then 1.25 ml of anhydric acetic acid 99% was added under stirring to reduce the hydrolysis reaction of the precursor. Afterwards 1.25 ml of acetyl acetone was added to the solution as a stabilizing agent and to incite the polycondensation reaction [24,27]. A yellow color indicated the reaction of acetyl acetone with the precursor. Finally a mixture of propanol and water (3.5/0.5 ml) was added. This solution was kept stirring and covered for one hour.

A second solution was prepared by mixing 1.7 ml (0.1 M) of zirconium propoxide with 0.85 ml of acetic acid 99 %. Then 0.54 ml acetyl acetone and finally a mixture of 2 ml n-propanol and 0.5 ml water were added.

2.2 Zirconium n-propoxide-hydroxypropyl cellulose sols

The solution of zirconium n-propoxide and hydroxypropyl cellulose as stabilizing agent was prepared as follows.

The first part was prepared by mixing 2.8 ml of distilled water with 1.3 ml of absolute ethanol and adding 0.001 g of the stabilizer HPC (80,000 g/mol MW) per ml of ethanol under rapid stirring in a beaker which has been previously cleaned with anhydrous ethanol and dried with warm air. This solution was covered and stirred overnight [44] to promote the dissolution reaction of HPC.

A second beaker was cleaned with absolute ethanol, dried with warm air and used as recipient for the second part of the solution. This part was prepared by mixing 0.54 ml of glacial acetic acid 99% with 1.70 ml of zirconium propoxide (0.1M) under stirring and adding 2 ml of absolute ethanol. This solution was rapidly stirred and covered for a few minutes. The first part was mixed with the second solution under vigorous stirring for few minutes. The resulting sol was kept covered and stirred for 2 hours and left still at room temperature for 2 more hours. This time is important in order to allow the complete reaction of the stabilizing agent with the precursor.

2.3 Hybrid sols

It is known that silicon compounds promote elasticity and other mechanical properties of the final coating [29]. Therefore silicon compounds such as phenyl triethoxysilane and tetraethylortosilicate (TEOS) were used to improve the protective properties of the film material. All recipes are shown in table 4.

Table 4. Sol composition

Name	Precursor	Volumen / ml	HOAc / ml	Hacac / ml	H_2O-Prop/ ml	H_2O-Etha/ ml	HPC g/ ml
ZrO_2 Acetylacetone	$Zr(OPr)_4$	2.5	1.25	1.25	2 / 0.5	-	-
Hydroxypropyl-cellulose(HPC)	$Zr(OPr)_4$	2.5	-	0.587	-/-	4.79 / 4	0.002
[Zr 50:50 Si] Acetylacetone	$Zr(OPr)_4$ $PhSi(OEt)_3$	2.5 1.4	2	2	5	-	-
ZrO_2 Hydroxypropyl-cellulose (HPC)	$Zr(OPr)_4$	1.69	-	0.587	-/-	2.79 / 4	0.001
ZrO_2 Acetylacetone	$Zr(OPr)_4$	1.70	0.85	0.54	2 / 0.5	-	-
Hydroxypropyl - cellulose (HPC) [Zr 50:50 Si]	$Zr(OPr)_4$ $PhSi(OEt)_3$	2.5 1.4	-	0.587	3.79 / 4	-/4	0.001

Different sol proportions were applied to study film structure and protective properties. The respective volume ratios are enclosed in table 4.

3. Deposition parameters and spin coating

Before coating the samples were cleaned with ethanol and warm air to remove any residues or impurities from the surface. Films were deposited in a spin-coater at room temperature with a syringe through a 0.45 µm mesh nylon filter. The sol was deposited onto the rotating iron sample as soon as the final spinning speed was reached. The spinning speed and rotation time were optimized until a reproducible and homogeneous film was produced.

The best results were obtained after a rotating time of 90 seconds. After this time the films showed good coverage and a reproducible homogeneous surface. The spinning speed was varied from 500 to 10000 rpm (revolutions per minute). Lower speeds resulted in thicker but cracked films; higher speeds from 8000 to 10000 rpm were not practicable due to the weight of the iron samples. As the optimum speed 4000 rpm was chosen which yielded the most homogeneous and reproducible films of all samples.

During the deposition process the spin coater was kept covered to prevent the formation of comets or irregularities on the sample surface [27].

4. Heat treatment

After the coating deposition all samples were kept covered for one hour at room temperature to prevent the precipitation and incorporation of impurities or dust particles and to promote the polymerization and network-formation process. During this phase some organic compounds of the sol began to evaporate from the surface. Besides time and speed the heat treatment of the samples had to be optimized, too. Therefore different temperatures and heating times were applied because the ceramic or ceramic-like character of the film structure depends strongly on these parameters. The temperature range was studied from room temperature (295K) up to 1073K. The exact temperatures were: room temperature, 373, 473, 573, 673, 773, 873 and 1073 K, respectively. All samples were treated with a heating rate of 50 K/15 min. The heating time at the final temperature in the furnace was one and two hours, respectively.

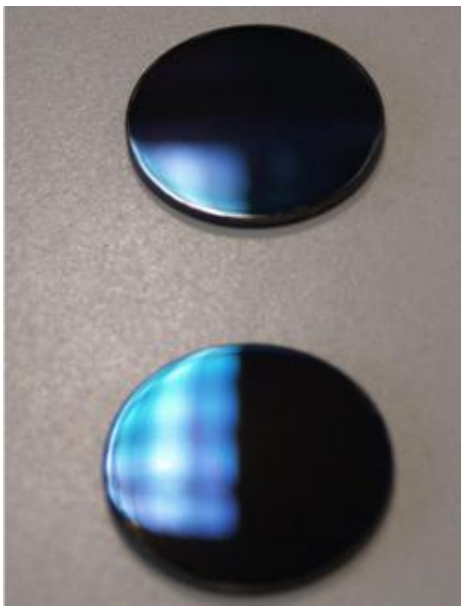

Fig. 28 Iron coated with zirconium propoxide and heated at 673 K

5. Film thickness

To determine the film thickness and its dependence on spinning speed and heating parameters, a Dektak® D8000 surface profilometer was used. Therefore the dimensions of sputter craters from secondary ion mass spectrometry (SIMS)

investigations were measured. Additional thickness measurements were estimated with X-ray diffraction (XRD) by the penetration depth of photons with energy of 8000 eV as a function of the incidence angle ω. Below a certain angle of incidence only the reflections of the film were visible [81]

II. Electrochemical measurements

1. Electrochemical cell

Electrochemical measurements were carried out with a typical three electrode setup and the assembly of the samples and the electrochemical cell are shown in fig. 29 and fig. 30, respectively. Samples were hold inside a plastic protector holder with silicon sealings leaving only a defined area of 2 cm^2 of the polished surface exposed to the electrolyte.

The coated sample acts as working electrode and the potential was measured against a standard saturated silver/silver-chloride electrode (0.197 V) vs. SHE. This reference electrode was placed inside a Luggin-capillary with the capillary tip close to the sample surface to avoid adverse effects from the potential drop of the solution. The counter electrode was a cylindrical rod made of platinated titanium.

Fig. 29 Assembly of iron samples in the sample holder

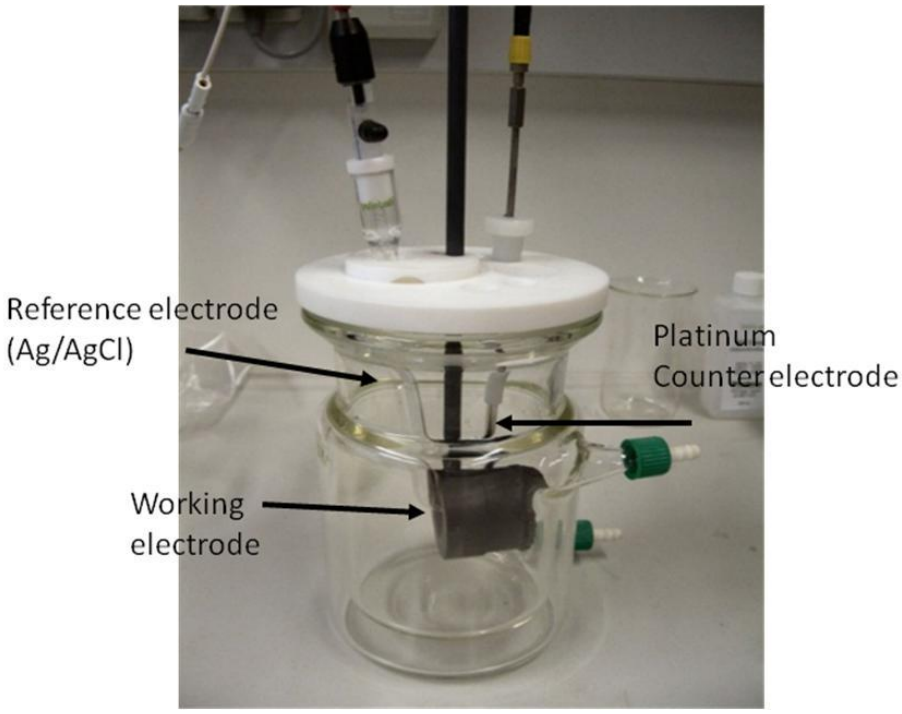

Fig. 30 Electrochemical cell

2. Electrolyte, pH and temperature

The electrolyte for electrochemical porosity measurements had to fulfill special demands: the pH-value had to be stable and the corrosion rate of iron should be moderate. The rate had to be as high as necessary to detect even small pores or defects of the coating but not too high to avoid distortion of the shape of the current density potential plots to guarantee a good visibility and reproducibility of the active metal dissolution area (fig. 31).

According to the Pourbiax diagram different electrolytes were chosen: sulfuric acid 2 M, pure water, sodium chloride 0.01M and 0.05M, sodium sulfide 0.05M, sodium sulfate 0.01M and a buffer of sodium acetat / acetic acid 0.1M/0.01M. The pH was measured with a pH-meter.

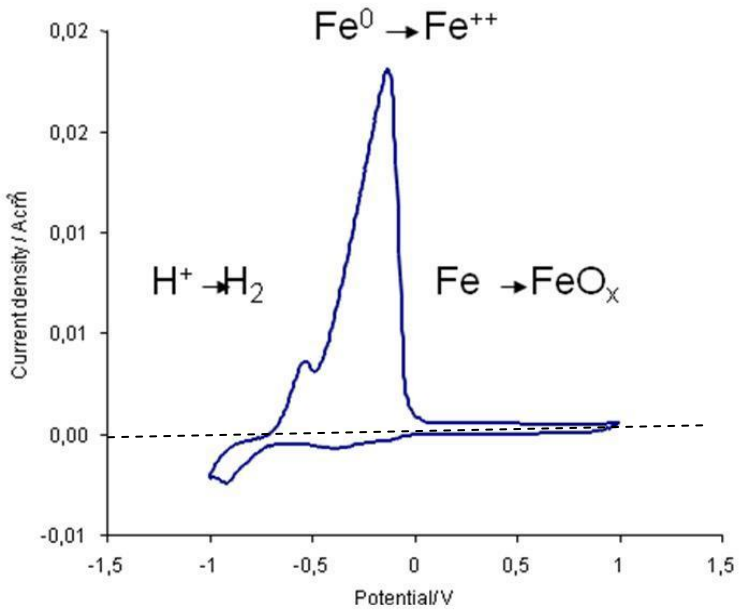

Fig. 31 Potential scan of pure iron in a sodium acetate/acetic acid (0.1/0.01M)

Best results of all tested electrolytes were obtained with a sodium acetate/ acetic acid buffer (0.1M/0.01M) with a pH value of 5.65. Each portion of electrolyte was prepared with de-ionized water.

Electrolyte temperature was verified with help of an equipment that controls the temperature of the electrochemical cell. Different temperatures were adjusted from room temperature 298 K to 308 K. This study was done to investigate the influence of the temperature on the corrosion process of bare samples. The working temperature was optimized at room temperature.

3. Potentiodynamic scans and cyclic voltammetry

Potential scans were carried out with the setup shown in fig. 30. A potential scan rate = 100 mV/s was applied for all experiments; a relatively high scan rate was chosen to avoid additional corrosive damage of the sample. The potential range was swept from -1 V to +1 V; and the surface exposed area was 2.01 cm^2; in cyclic voltammetry measurements 20 cycles were recorded to study the stability of the coating over a longer period of time. Each experiment was done in a fresh electrolyte. Potentiodynamic polarization curves were obtained with a

Princeton Applied Research Potentiostat “Parstat 2273” with the software Power Suite 2.58.

4. Linear polarization resistance

The linear polarization measurements were carried out with the same three electrode setup as in 1.5.3. Polarization resistance (Rp) measurement is a well known corrosion test to investigate the corrosion process and to determine the corrosion current and corrosion rate of the coated iron samples [80]. In this case the electrolyte was exchanged with a sodium chloride solution (NaCl) of 0.01 and 0.05 M. A low scan rate of 1 mV/s was used to establish equilibrium conditions. The scanned range was – 0.20 Volts and + 0.20 Volts vs. OCP. Open circuit potential was measured for 45 min. prior to each linear polarization experiment to guarantee equilibrium conditions. The Power Suite software was used for the calculation of Rp and corrosion rate.

5. Tafel Plot

The setup for the Tafel Plot experiments was the same as for linear polarization except the scan rate was decreased to 0.116 mV/s [46]. At the beginning of each experiment the OCP was recorded for 45 min until equilibrium had established. The potential range was scanned from – 250 mV to +250 mVolt vs. OCP. The extrapolation of Tafel plots was done with the PowerSUITE® software package and corrosion currents and corrosion rates were fitted based on density, equivalent weight and exposed area of iron.

6. Electrochemical impedance spectroscopy

The measurements were made in the same three electrode setup as in the section 1.5.3 after the samples reached equilibrium at invariable OCP. The electrolyte solutions were sodium actetate / acetic acid buffer (0.1M/0.01M) and sodium chloride with a concentration of 0.1M and 0.05M, as well. The frequency range was set between 0.005 Hertz and 10.000 Hertz. The electrical equivalent

circuit was verified with the ZSimpWin 3.21 software (Echem Software, Bruno Yeum, Dimauril 2005) and the evaluation of circuit components was done with Power Suite®.

III. Structure and composition characterization

1. Scanning electron microscopy (SEM/EDX)

Scanning electron microscopy (SEM) was applied to characterize the morphology of the different films. Microphotographs were obtained at acceleration voltages of 10kV and 20kV to generate high resolution images. Because of the three-dimensional appearance of SEM images a detailed observation of the surface is possible. In the mechanism of SEM, the primary electrons coming from the source strike the surface and are inelastically scattered by sample atoms. Secondary electrons emitted from the sample surface are detected to produce an image; because the high energy of the primary electrons excite electrons at the magnetic shell of the sample producing X-rays. These were detected in an energy dispersive X-ray (EDX) spectroscope. The use of EDX allows the identification of elements in the upper sample surface. The SEM equipment can be also adapted for different detection modes such as the detection of backscattered electrons or electron backscatter diffraction (EBSD) which gives crystallographic information about the sample. Generally a resolution down to several nm is possible [82]. The SEM used in this investigation was from FEI Company, Series XL 30 (FEG).

2. Electron probe microscope analysis (ESMA/EPMA)

This method was utilized to receive an element composition map of the sample surface and to verify the coating homogeneity as well. This method is a combination of X-ray microanalysis and scanning electron microscopy. ESMA provides the opportunity to obtain information about the local elemental composition in conjunction with the surface topography. Here the use of SEM allows the optical electron micrographic view. In this technique electrons are

emitted from a common source and bunched in the middle of an electromagnetic lens system that will spotlight the electrons to the analyzed sample. It works similarly to a SEM where the sample is bombarded with an electron beam, and signals that come from the sample are collected. Specific X-ray wavelengths are selected and counted. This enables the elements present within sample volumes of 10-30 cubic micrometers or less to be determined, by comparing the intensities of characteristic X-rays from the sample material with intensities from known composition (standards). The equipment used in this work was a Cameca serie SX50.

3. X-ray photoelectron spectroscopy (XPS)

XPS is a surface sensitive analytical tool which objective is the determination of chemical composition and electronic state of the sample. During the XPS measurement, the samples are kept under high vacuum and are bombarded with X-rays. The photons penetrate several nanometers deep into the superficial layer of the sample, exciting photoelectrons. The emissions emanated from the excited electrons from about 5 nm depth can be detected. The energy of these electrons is measured by an analyzer.
With help of monochromatic X-rays it is possible to quantify the binding energy emitted of the electron by an equation of Einstein:

$$E_{binding} = E_{photon} - E_{kinetic} - \Phi \quad (51)$$

Φ is the work function of the material. Because the energy of the electrons shell is specific for each element the spectrum provides information about the elemental composition of the thin surface region. XPS provides also the possibility of creating depth profiles of the elemental composition by surface sputtering [82,83]. The XPS spectra were measured on a Thermo VG Scientific ESCALAB 250.

4. Secondary ion mass spectrometry (SIMS)

In order to study the film structure and the element distribution, a depth profile of the coating was received from secondary ion mass spectrometry (SIMS) measurements. The films were bombarded with Cs^+ ions with a current of 15 nA and 5.5 keV as impact energy. SIMS is an analytical technique that can detect very low concentrations of dopants and impurities. It can provide elemental depth profiles over a depth range from a few nanometers to tens of microns. SIMS works by sputtering the sample surface with a beam of primary ions. Secondary ions formed during the sputtering are extracted and analyzed using a mass spectrometer. These secondary ions can range from matrix levels down to sub-parts-per-million trace levels [83,84]. A scheme of the SIMS equipment is presented in the next picture.

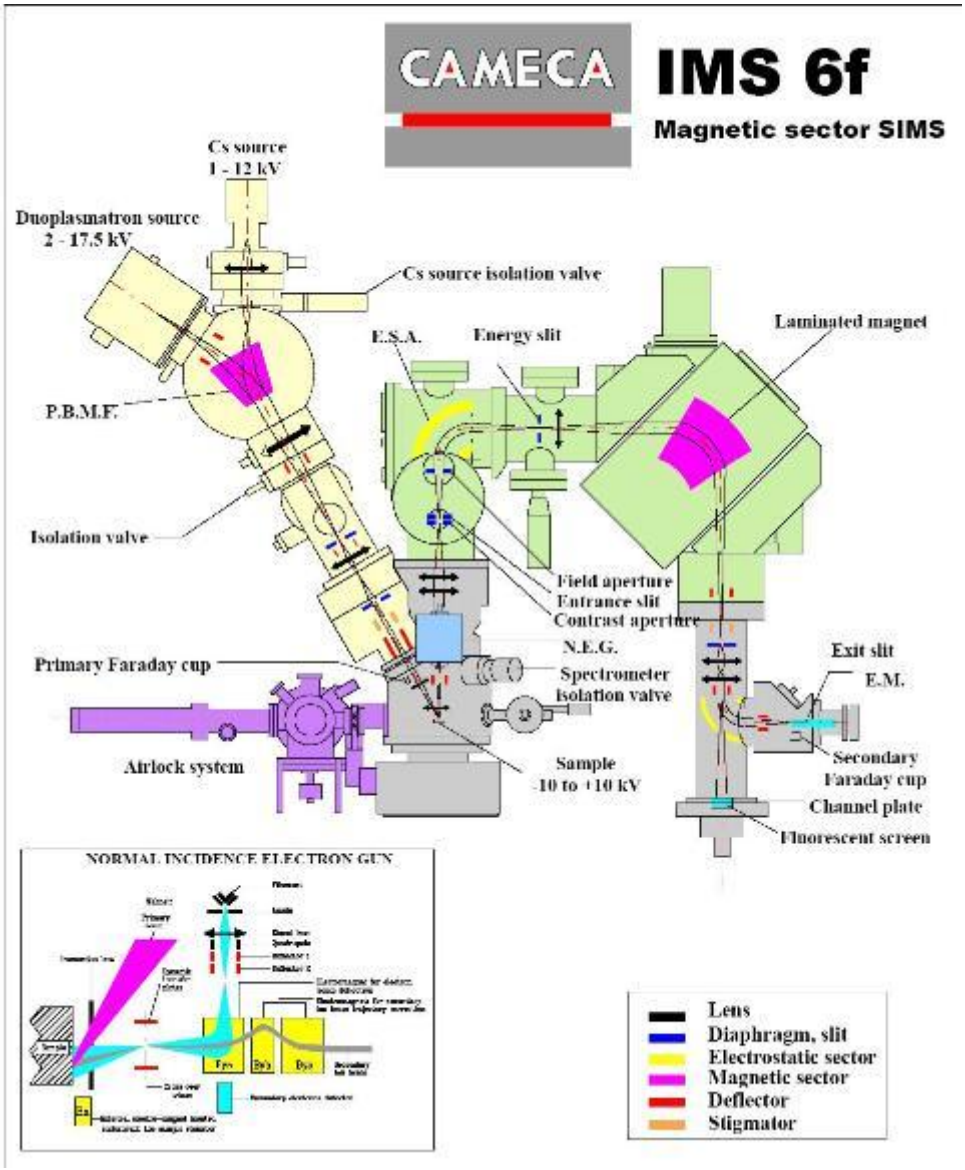

Fig. 32 Scheme of the SIMS equipment [85]

5. X-ray diffraction (XRD)

Knowledge of the chemical composition and the physical phases of the inner structure of the coating material are essential to understand the effects and interaction of deposition parameters on the protection performance. Therefore the crystalline phases of the films were studied with X-ray diffraction (XRD) using a four circle diffractometer (Seifert PTS 3003). The diffractometer was operated with Cu $K\alpha_1$ and $K\alpha_2$ radiation with 8027 eV as X-ray energy, using an X-ray mirror at the primary side and a long Soller slit with a 0.3° divergence with

respect to the sample surface plane as well as a graphite monochromator at the secondary side [81]. For the surface sensitive grazing incidence X-ray diffraction measurements (GIXD) the inclination angles were: ω = 0.1°; 0.3°; 0.8°; 1°; 3° and ω = 5°. X-ray diffraction was also used to verify the film thickness of the coating.

In an X-ray diffraction measurement, the sample is rotated precisely and irradiated with X-rays at different angles. From the obtained diffraction patterns at a variety of rotation angles a three-dimensional model of the electron density can be created within the crystal and combined with chemical data of a known sample. Poor resolution or even errors may result if the crystals are too small or non-uniform in their internal structure [86].

X-ray diffraction is commonly used to identify different phases of polycrystalline samples. The two most important advantages for analysis of hybrid materials are the speed and nondestructive conditions of this technique. The positions and intensities of a diffraction pattern are unique for a single substance. The X-ray pattern of a substance can be seen as a fingerprint and mixtures of different crystallographic phases can be easily distinguished by comparison with reference data [86].

6. Transmission electron microscopy (TEM)

Transmission electron microscopy (TEM; FEI, CM20STEM) was performed to distinguish and identify the particle size and structure of the zirconium oxide film. High-resolution TEM images were analyzed with the software Gatan DigitalMicrograph^{TM}. Electron patterns were analyzed with Fourier Transform and with special interpreting software PIEP. In TEM measurements images are obtained by focusing a beam of electrons onto a very thin sample. The beam will partially penetrate the thin film and the electrons will interact with the sample material on their way through the sample yielding information about its inner structure. The images are recorded at a photographic plate or a light sensitive CCD sensor and the image can be displayed in real time. Due to the weak interaction of the samples with the electron beam it is often difficult to observe detailed structures in TEM, especially for samples that have a high content of

organic components. Often heavy metals are used to overcome this problem. The dense electron clouds of the heavy atoms interact strongly with the electron beam. TEM allows also determination of the elemental composition of the specimen by analyzing its X-ray spectrum or the energy-loss spectrum of the transmitted electrons. Additionally if the observed material is crystalline, diffraction patterns are obtained that give information about the crystal orientation [84].

C. Results and Discussion

I. Parameters optimization

Prior to the analysis of coated samples certain parameters needed to be adjusted to guarantee reproducible and informative data. These parameters include: spinning speed and time and its influence on film thickness, temperature and time of heat treatment, electrolyte composition and dependence of current density-potential plots on temperature.

1. Influence of spinning rate and time on film thickness

As described in the experimental part, the film thickness depends on the spinning speed and time during the spin coating deposition process, as well as on heating temperature and time in the furnace.
Fig. 33 shows the results of profilometer thickness measurements of zirconium oxide films on iron samples obtained at different rotation rates and different heating temperatures.
As can be clearly seen in the graph, low spinning speeds result in thicker films but the thickness variation becomes less significant at temperatures higher than 873 K.

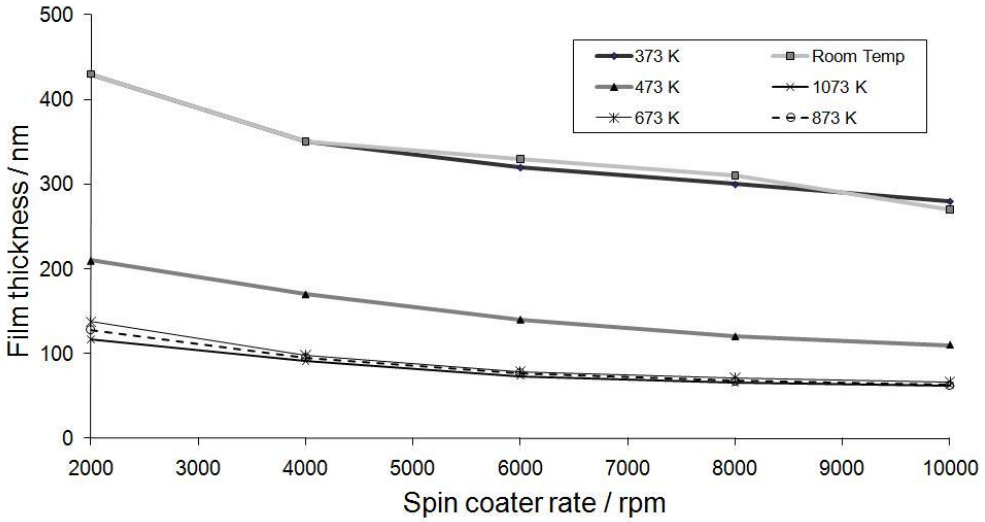

Fig. 33 a) Film thickness as function of spin coater rate for different heat treatment temperatures

It can be also seen that beyond 4000 revolutions per minute (rpm) the further decrease of thickness with increasing speed becomes marginal. Therefore and due to the relatively high weight of the iron samples a moderate spinning rate of 4000 rpm was chosen as the standard speed for all samples. Under these conditions the film thickness was 120 nm ± 20 nm. These data was obtained from zirconium oxide coatings stabilized with acetyl acetone (acac). In the case of zirconium oxide coatings stabilized with hydroxypropyl cellulose (HPC) the films were 30 nanometers thicker than acac-films [37].

2. Heating time and temperature effect

Between samples that were dried at room temperature or treated at 373 K in a furnace for one hour no significant dependence on temperature was observed (see Fig. 33 b). After treatment at these low temperatures the coatings could be easily washed off with distilled water. Obviously the properties of these films matched the original precursor-gel rather than a ceramic-like coating. However, heating temperatures above 473 K yielded coatings that could not be removed with water. Their thickness was much thinner as can be seen in fig. 33 b. They showed good adhesion to the metal surface.

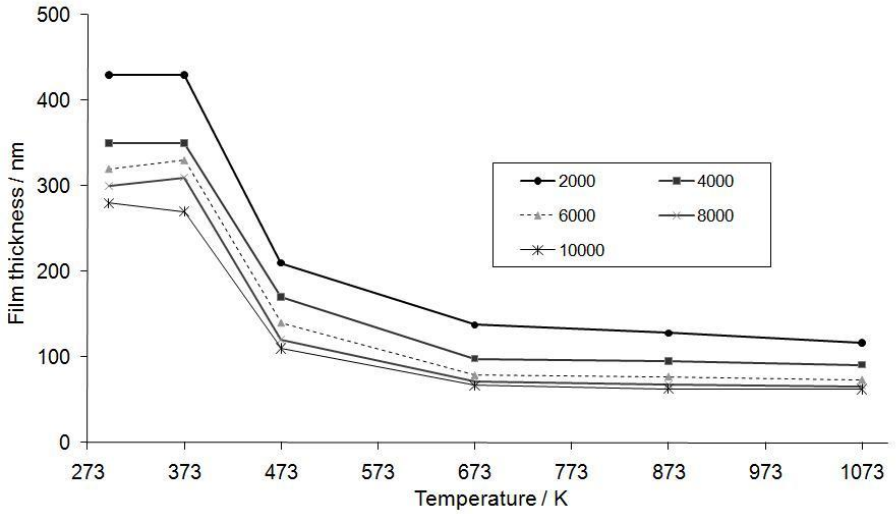

Fig. 33 b) Influence of temperature on film thickness

It can be also seen in fig. 33 b) that a heat treatment above 673 K will no longer change the film thickness significantly. Therefore it can be expected that the most critical structure changes occur in the lower temperature region. Samples treated at higher temperatures over 773 K showed rises on the edges because of pressure and metal expansion that probably could be later no recommendable for the good performance of the coatings.

As a consequence of different film thicknesses in the range of hundreds of nanometers, coated samples showed typical decorative interference colors from bright blue, silver, green up to red and gold [23].

3. Effect of the electrolyte temperature

Because electrochemical reactions among other factors depend on mass transport through different phases, it was necessary to investigate the effect of temperature on the electrochemical data to ensure the reliability of these experiments. Therefore dissolution current densities vs. potential plots of uncoated iron samples were recorded at different temperatures of the sodium acetate/acetic acid buffer solution (0.1M/0.01M). Each potential scan was repeated 20 times to receive information about the long term behavior of the sample. From the current density vs. potential curves the maximun current (I_{max})

of anodic iron dissolution was extracted. Fig. 34 shows I_{max} as a function of the number of potential cycles, recorded at different electrolyte temperatures. The electrolyte dissolution current densities increase over 20 cycles because the metal surface takes damage over time from the corrosive attack, as can be seen in fig. 34. A dependence on temperature is clearly visible, though it is insignificantly small at the first cycle and lies within the range of natural current density variation. The first one is also the most important cycle for the determination of film porosity because here the sample's condition is very close to its original state right after film deposition and the sample has not suffered severe corrosion damage yet. Because of the increased mass transport at higher electrolyte temperatures the corrosive damage will also increase stronger with the duration of the experiment. Therefore the rise of current densities becomes much more significant with increasing number of cycles. Since the ambient temperature in the laboratory varies only a few degrees from 293 K and usually only the first cycle is considered in porosity evaluation, all experiments could be done without temperature control. Additionally, the influence of other sol composition parameters was found to be orders of magnitude stronger than electrolyte temperature.

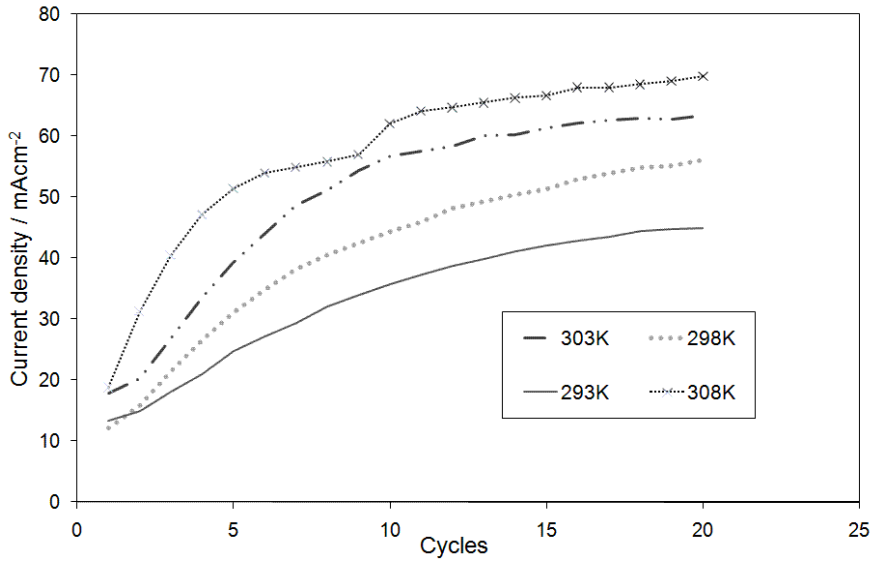

Fig. 34 Variation of the current density at different electrolyte temperatures for pure iron

4. Types of electrolyte, pH and concentration

For the electrochemical evaluation of film porosity a suitable electrolyte had to be found that allowed a moderate corrosion rate of coated and uncoated samples and clear identification of typical corrosion phenomena in the graph, i.e. anodic oxidation, maximum dissolution current density, formation of passive layers, etc. Therefore various parameters such as electrolyte salt concentration, pH-value and scanning speed had to be adjusted. Thereby various electrolytes have been tested at different concentrations, such as sodium sulfite, sodium chloride, sodium sulfate and sulfuric acid. None of them met the desired demands because current densities were either too high or low or specific corrosion phenomena could not be observed in the graph. Instead, best results were obtained from a sodium acetate / acetic acid buffer solution (0.1 mol/l / 0.01 mol/l) with a pH-value of 5.65 as shown in fig. 35. Similar buffer concentrations have been successfully applied to the analysis of iron corrosion behavior before [23,43].

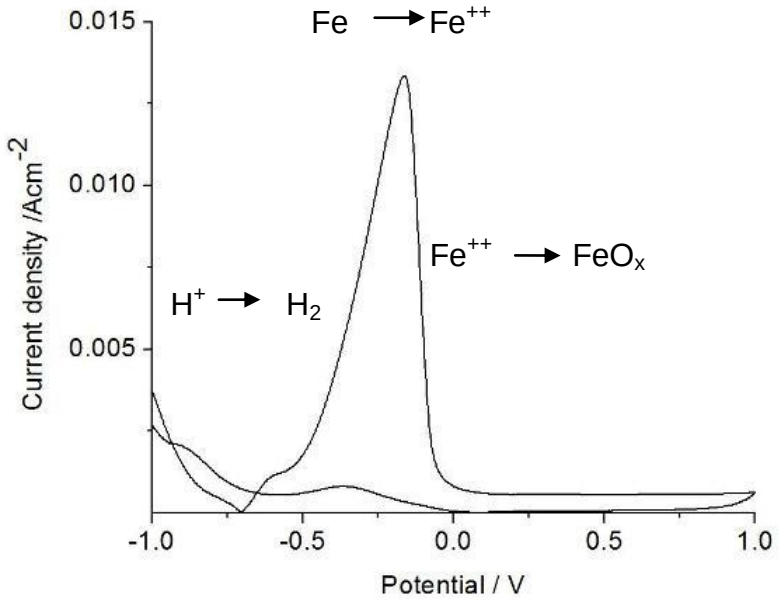

Fig. 35 Current density behavior of iron in buffer sodium acetate/acetic acid (NaAc/HAc; 0.1/0,01M)

A particular advantage of the acetate buffer solution is its ability to keep the pH-value constant in contrast to most pure salt solutions. A pH-alteration would result in strong disturbances of electrochemical reactions and therefore reproducibility of porosity evaluation could hardly be accomplished.

II. Electrochemical porosity measurements

1. Potentiodynamic scans

Fig. 36 shows a linear potential scan of an uncoated iron sample. The current density is plotted in logarithmic scale vs. potential for better visualization. At negative potentials left from the open circuit potential (OCP) the sample behaves cathodic and reduction reactions dominate on the metal surface. At the OCP cathodic and anodic reactions proceed with the same ratio, resulting in a sum current density of zero. At higher potentials the sample will show anodic behavior and an increase of current density can be observed due to beginning metal dissolution. With growing potential current density rises further until a maximum current density I_{max} can be observed as a peak in the graph. It expresses the maximum iron dissolution rate before the passive film formation starts at higher potentials. The value I_{max} of the uncoated sample can be used as a reference current density representing a porosity of 100 %. As long as the sample has not suffered significant corrosion damage the current density is primarily dependent on the size of the uncovered substrate surface, i.e. the film porosity. Therefore a high scan rate was chosen to avoid change of the pore structure due to precipitation or delamination. This way the coverage and porosity of different insulating coating materials can be determined in relation to the uncovered metal surface.

In addition the open circuit potential (OCP) gives an indication of the nobility and resistance of the coated sample. However, the reliability of this information is limited because various parameters like surface condition and oxide films have a strong effect on the position of the OCP. In some cases though, when

the coating material is absolutely inert, an OCP-shift can provide information about the change of the average pore size of different coatings [23,24].

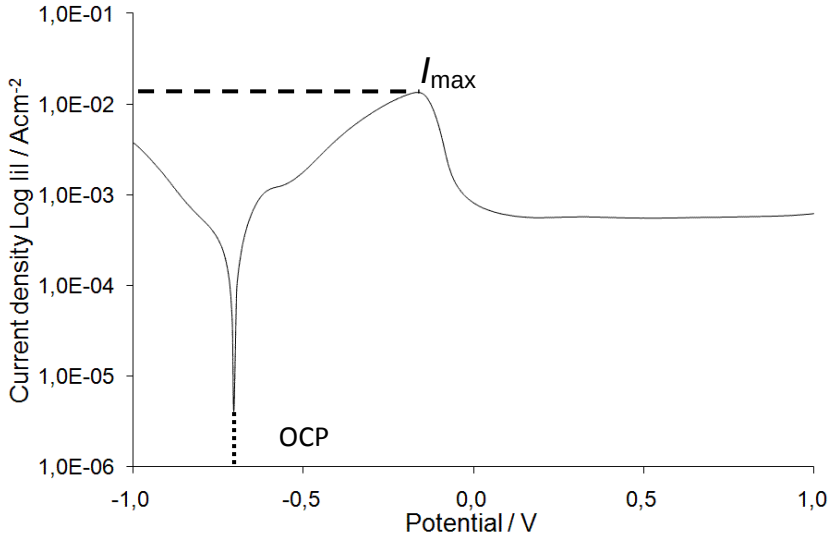

Fig. 36 Potential scan of uncoated iron

1.1 Zirconium oxide coatings with acetyl acetone (ZrO_2-acac)

1.1.1 Influence of heating temperature

Fig. 37 shows the influence of the heating temperature on the dissolution current density I_{max} for samples coated at 4000 rpm with zirconium propoxide and acetyl acetone (1:1) as stabilizer.

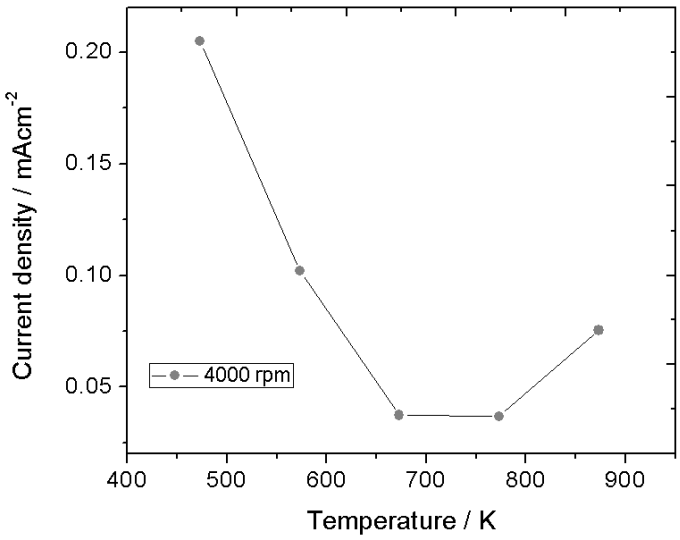

Fig. 37 Effect of heat treatment temperature on current density

From 473 to 673 K the current density decreases due to drying and densification processes in the coating material. These reactions lead to a reduction of both number and size of pores. At 673 K the dissolution current density is decreased by approximately 4 orders of magnitudes with respect to the 473 K sample. At 773 K the current density is still very low but increases when temperature is raised to 873 K. This behavior could be related to stress phenomena in the coating material, especially in the interface region between substrate and coating. In the literature it has been indicated that zirconium propoxide shows a phase transition around 698 K into crystalline material [56]. Together with electrochemical porosity evaluation also structural characterization experiments such as XRD, SIMS and TEM were done to verify whether this transition might have a beneficial effect on the corrosion resistance of the coating. At higher temperatures the sol-gel films will show more ceramic-like behavior, that is high hardness and density. But unless these structures have a positive effect on the protection ability there is no reason to apply more energy in the process than necessary. According to fig. 37 a further temperature raise beyond 673 K does not contribute significantly to porosity reduction, therefore the focus of further investigation was on the lower temperature range and the structural changes that can be observed there.

In another experiment current densities were recorded over 20 cycles for each sample to investigate whether higher temperatures will yield more stable film structures. The results are shown in fig. 38.

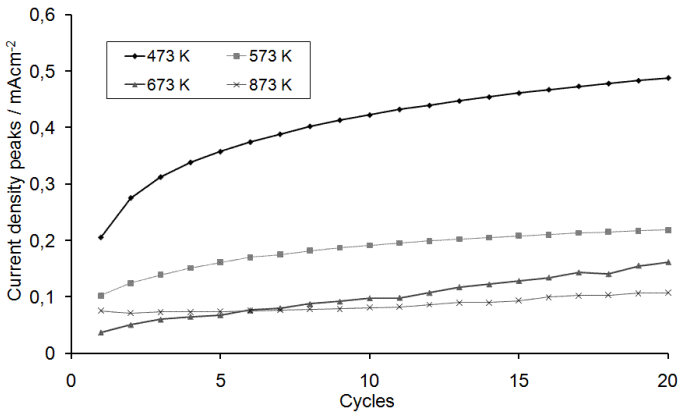

Fig. 38 Maximum current density peaks as a function of potential cycles for a coating rate of 4000 rpm

All samples show rising dissolution current densities over 20 cycles because they take increasing damage from the corrosive attack of the electrolyte. But while the sample heated at 473 K shows a quite steep rise of current density this effect diminishes consequently with increasing temperature. This was the minimum temperature that was necessary to obtain a coating which could not be removed with water any more, indicating good adhesion to the substrate. However, the film remains in an amorphous state because of the low temperature. After heating at 873 K the rise of current density over time becomes negligible. On the other hand this sample shows a higher porosity during the first five cycles compared to the 673 K sample.

It looks like higher temperatures can fortify the coating structure, leading to more stable coatings but unfortunately the benefit of stability comes along with a higher porosity. This experiment also suggests that the best results can be expected from the low to medium temperature range. Apart from porosity one also has to consider the substrate material which may limit the available temperature range of the heating procedure. The advantage of greater stability

will be obsolete when the metal substrate suffers from structural damage or undesirable oxidation.

1.1.2 Effect of propanol/water ratio

Several potential scans were recorded with different volume ratios of the solvents propanol and water. The volume ratio of propanol and water in the solution of zirconium n-propoxide was varied from 4:1 to 3:1, respectively. The variation of this parameter has obviously at most a very small effect on the current density which is hardly significant as can be seen in fig. 39.

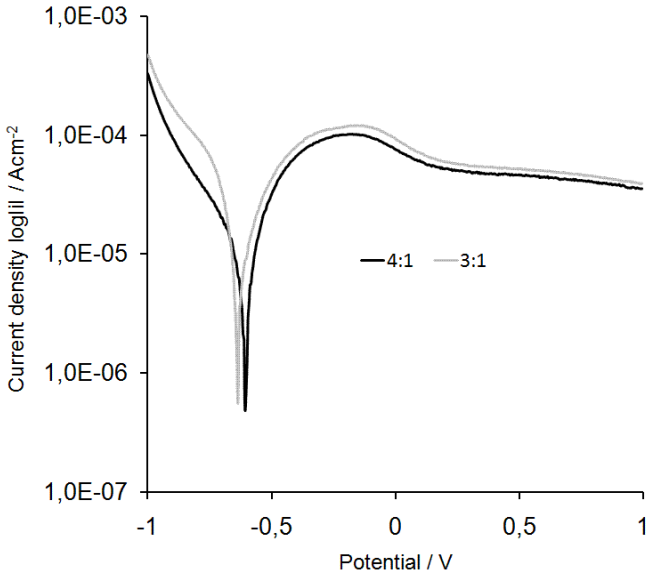

Fig. 39 Effect of propanol/water ratio on current density for coated samples after heating at 573K for 1 hour

The solvent mixture of propanol and water acts as solvent and hydrolysis initiator as well. Therefore variations of both volumes have no considerable effect on the proceeding of the condensation reaction and final network structure, thus the film porosity remains the same.

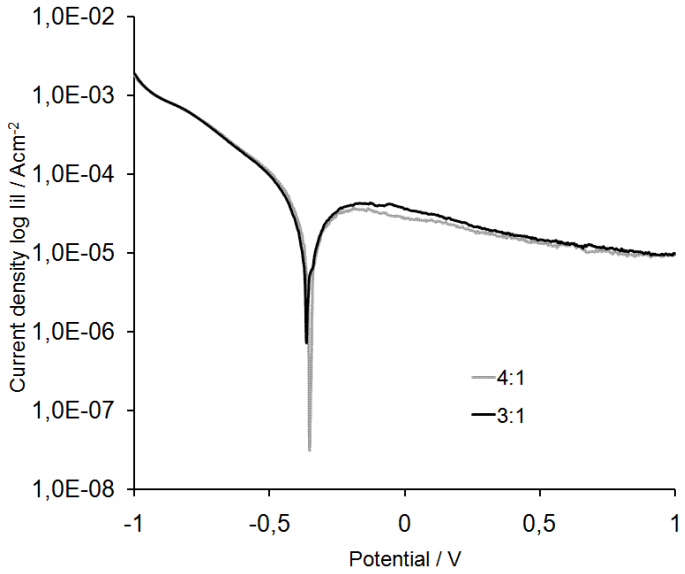

Fig. 40 Effect of propanol/water variation on current density for samples treated at 673K

This is supported by samples that have been treated in the same way except that the heating temperature was raised to 673 K. As can be seen in fig.40 both current density and OCP do not change significantly and again pore structure is not affected by neither volume variation.

1.1.3 Effect of acetyl acetone concentration

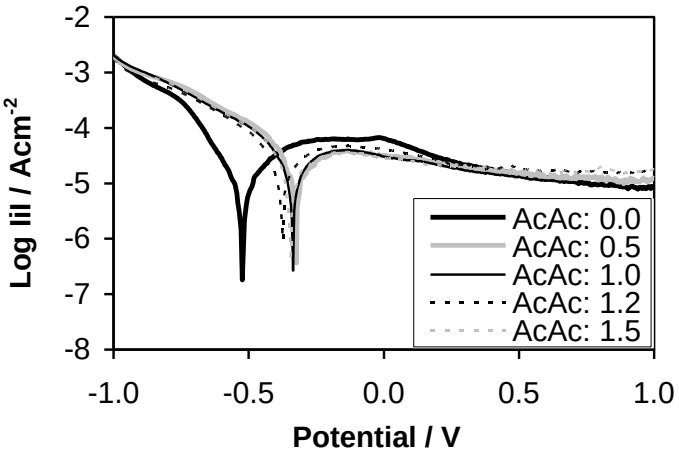

Fig. 41 Potential scans of coatings with different acac concentrations heated at 573K [24]

In the fig.41 the dissolution current density vs. potential plots of samples with different amounts of acac are shown. The shift of the open circuit potential of the curves towards anodic direction (positive potentials) might be an indication of the reduction of the average pore size [23]. The maximum current density peaks have decreased in comparison to the uncoated iron by two orders of magnitude for the sample with a ratio of 1:1. This ratio seems to be the optimum providing the lowest current densities as can be seen in the linear graph in fig. 42.

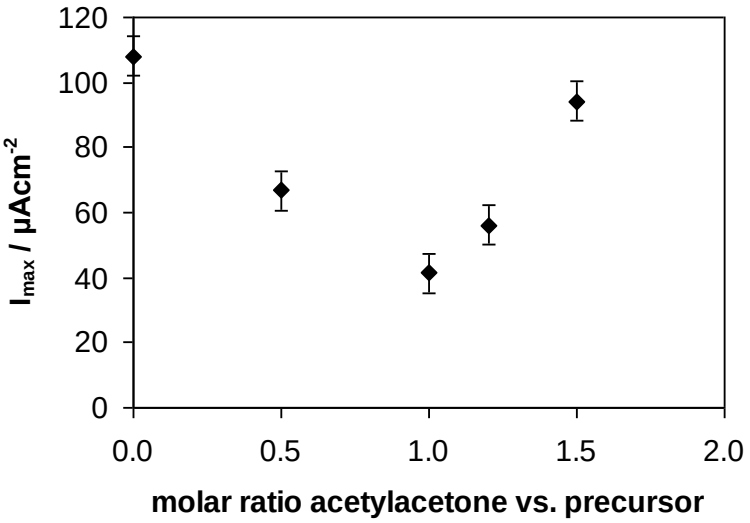

Fig. 42 Current density vs. molar ratio of acetyl acetone/precursor [24]

According to the literature the precursor structure is stabilized at a determined precursor/acac ratio [38]. Obviously this structure also promotes the formation of a low-porous film. A further increase of acac conentration will destabilize the precursor which corresponds to the observed rise of current density in fig. 39 when the ratio is raised beyond 1:1.

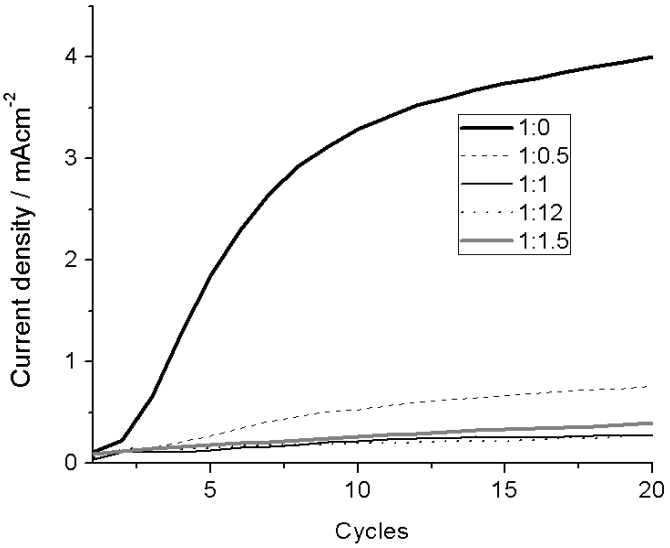

Fig. 43 Current density of coated iron prepared with different molar ratios of acac and heated at 573K

Fig. 43 shows another record of maximum current densities over 20 cycles to see whether the amount of acac affects the stability of the sample in a similar way like it was observed for higher drying temperatures. When the coating is prepared without acac the current densities rise abruptly which indicates that the sample is not stable at all. As soon as acac is added the stability improves significantly and the samples remain in good condition, even after 20 cycles. This result underlines the importance of the effect of stabilizing agents on the final film structure of protective sol-gel coatings.

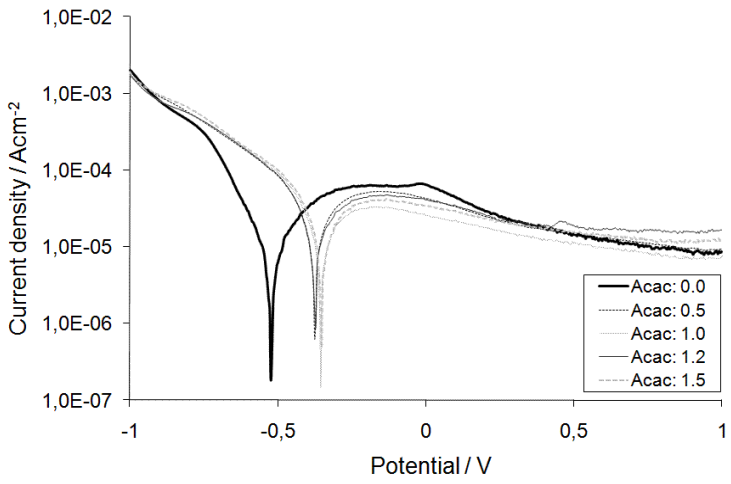

Fig. 44 Potential scans of different coatings heated at 673 K

The effect of acac concentration seems to be independent on the applied heating temperature as can be seen in fig. 44, 45 and 46. After heating at 673 K the samples show a very similar behavior like the 573 K samples before. Lowest current densities are again found at an acac/precursor ratio of 1:1. The coating material is subjected to substantial changes during the drying and heating step due to solvent evaporation, densification and bond-fragmentation. Since the effect of acac can be verified in the final coating it seems that the stabilizer promotes some fundamental structure change which persists through the heating step.

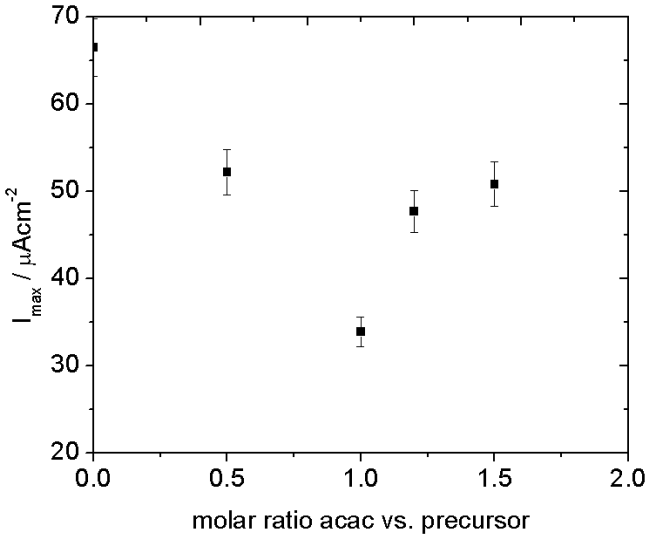

Fig. 45 Current density and molar ratio acetyl acetone vs. precursor

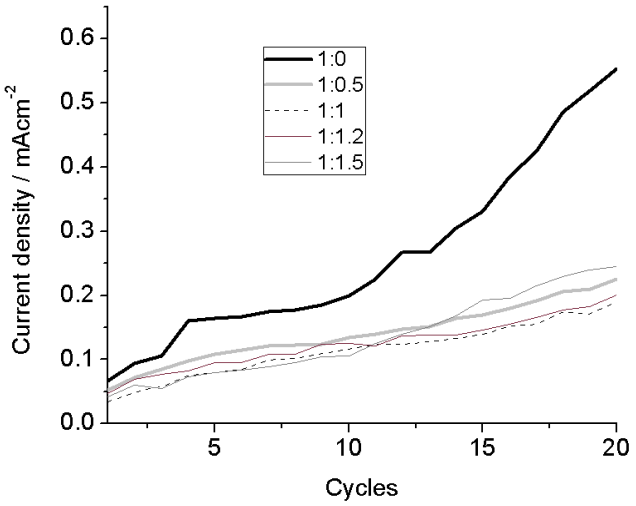

Fig. 46 Cyclic voltammetry of coatings prepared with different molar ratios of acac and heated at 673K

During the condensation and gelation phases the alkoxide tends to be stabilized in a compact and dense film because of the chelating influence of acetyl acetone. This can provide better particle accommodation and better adhesion to the substrate, reducing thus the film porosity and therefore also reducing the contact between film and electrolyte. These experiments were repeated in more occasions throwing reproducible results.

1.1.4 Effect of heating time

In the fig. 47 and fig. 48 potential scans of coated samples heated for one and two hours in a furnace at 573 and 673 K are shown. Samples heated for two hours show additional reduction of the current density in comparison with samples treated for one hour. It appears to indicate that a prolongation of heating can improve the film properties; however from an application point of view, additional heat exposition means also higher energy costs to obtain only a little improvement.

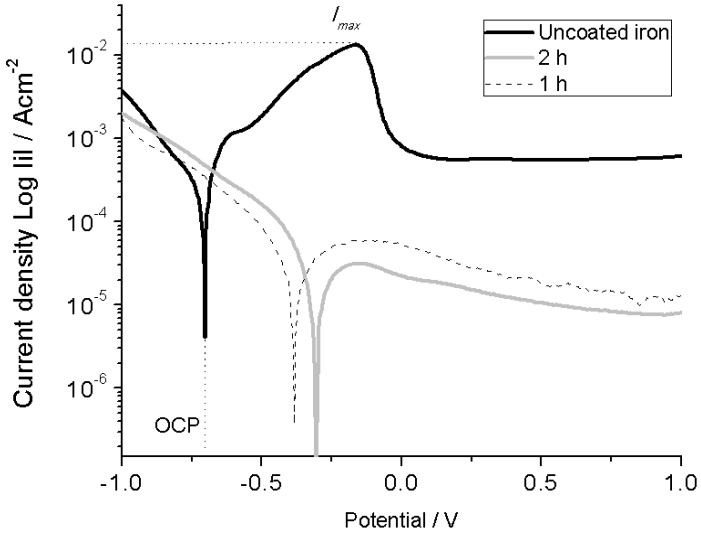

Fig. 47 Comparison ZrO_2-acac coatings heated for 1 and 2 hours at 673 K

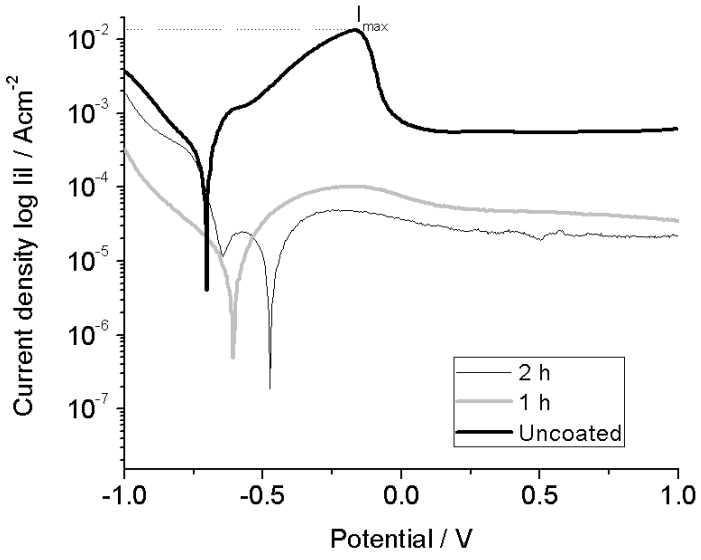

Fig. 48 Comparison of ZrO_2-acac coatings heated for 1 and 2 hours at 573 K

1.1.5 Multilayer coatings

An alternative way of reducing film porosity is the deposition of a second coating layer on top of the first ZrO_2 film. The second layer should improve the protection ability of the coating for two reasons: remaining pores in the first layer will be covered and the coating becomes a much stronger electrolyte barrier

due to its higher film thickness. This method has been also successfully tried for other coatings systems in [87-90]. The current density vs. potential plot of such a multilayer coating is shown in fig. 49.

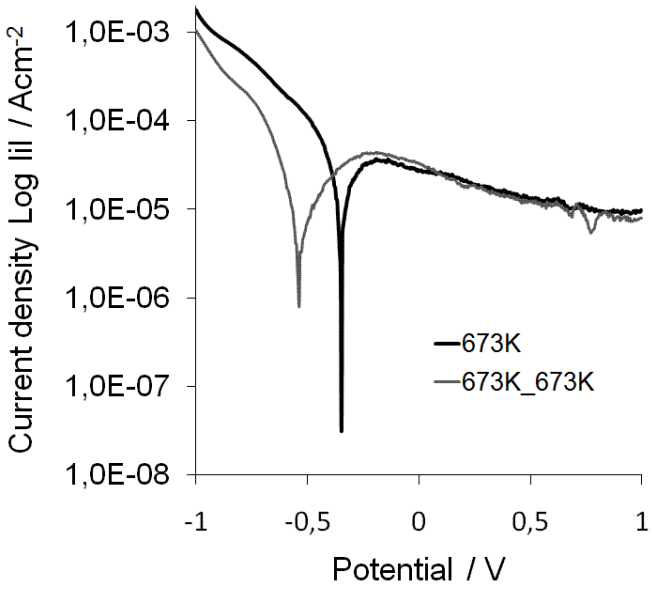

Fig. 49 Current densities for double layer ZrO_2 coating heated at 673 K

The coating consists of two ZrO_2 films that were deposited one after the other. Both were subjected to the full deposition procedure, including the heating step at 673 K for one hour. However, a significant enhancement of protection cannot be observed in comparison to the corresponding monolayer system. The current densities of both coatings are almost identical. Actually the cathodic OCP-shift of the multilayer system suggests a less noble behavior with increased average pore size.

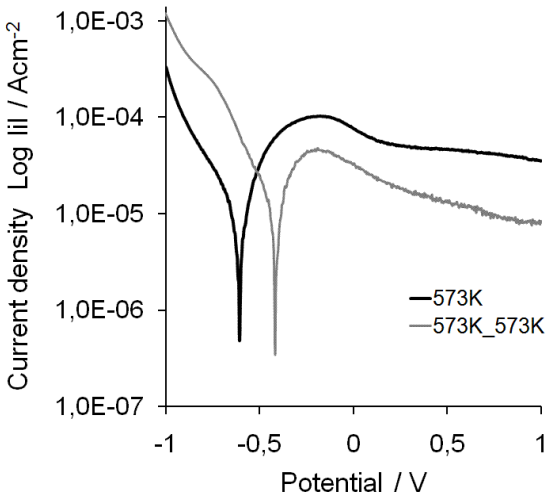

Fig. 50 Current densities double layer ZrO_2 coating heated at 573 K

A different behavior can be observed for samples heated at 573 K. This time the current density of the double layer system is about 20 % lower compared to the single layer film. The OCP is shifted in anodic direction, indicating a reduced pore size. Obviously at 573 K stress phenomena are far less dominant than at 673 K. So in principle the idea of improving the protection by the deposition of a second layer works for this coating system but only at the lower temperature range. Since the porosity of the monolayer coating heated at 673 K is still lower compared to the two-layer system heated at 573 K, there is no benefit that could justify the uneconomic second deposition step.

1.2 Hybrid films

Another advantage of the sol-gel process is the option to combine different precursors to join their properties in a new class of materials. In these so called hybrid coatings inorganic components usually provide hardness, density and chemical resistance while the addition of organic compounds can increase flexibility, elasticity and adhesion. [4, 91,92].

In this experiment zirconium propoxide was mixed with phenyltriethoxysilane. Silicon compounds are commonly used in sol-gel deposition for their good corrosion resistance, UV-protection and hydrophobicity [93,94]. Especially the

latter could have a favorable effect on the corrosion protection ability in aqueous media.

1.3 Zirconium-silicon oxide coatings

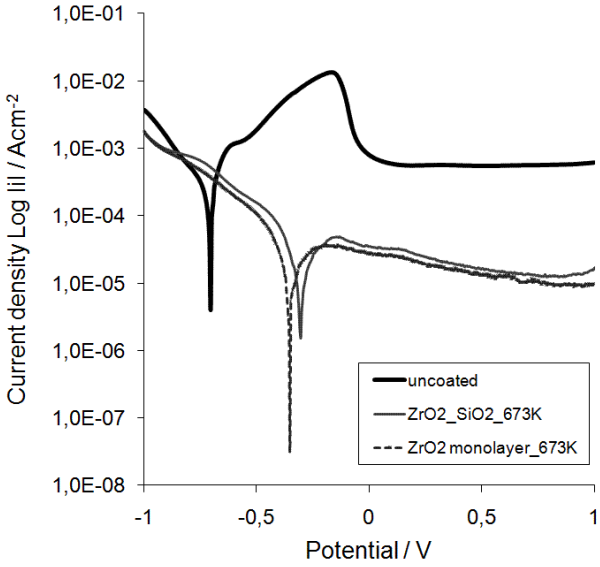

Fig. 51 Hybrid coating based on zirconium oxide and silicon oxide

Fig. 51 shows the potential scan of a hybrid film prepared with a mixture of zirconium propoxide and phenyltriethoxysilan (1:1) that was heated for one hour at 673 K. The maximal current density of the hybrid film is about 3 orders of magnitude lower than uncoated iron. However, in comparison to the corresponding ZrO_2 monolayer coating the differences in current density and OCP are very small and hardly significant.

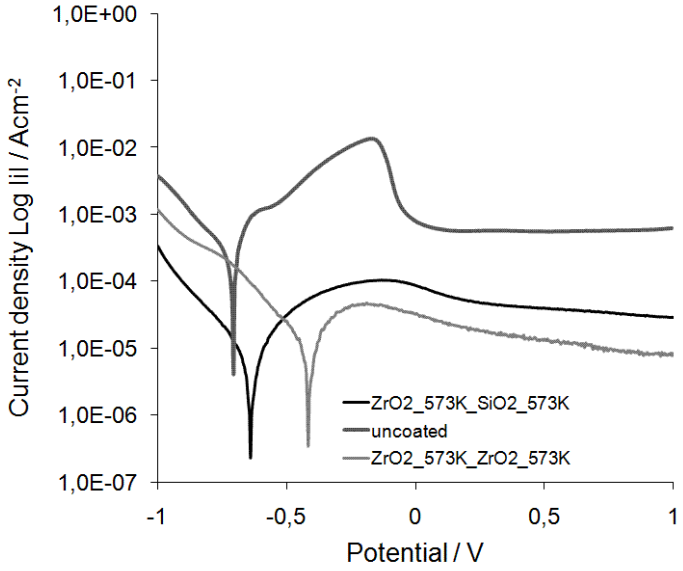

Fig. 52 Multilayer hybrid coating of ZrO_2 and SiO_2

Fig. 52 shows another kind of hybrid coating. This time the two precursors were combined in a multilayer system, one coating on top of the other. During the film preparation the samples showed increased oxidation when the silicon precursor was deposited first directly on the iron surface, therefore the zirconium layer was deposited on the substrate instead and the silicon component was deposited on top. To avoid stress phenomena like they occurred during the deposition of ZrO_2 double layers at 673 K the silicon/zirconium multilayers were only heated at 573 K. At this temperature a significant effect of the additional layer was found for the ZrO_2 system (fig. 49).

Although the multilayer coating shows a considerable reduction of dissolution current density in fig.49 compared to the uncoated metal the performance of the pure ZrO_2 double layer film without silicon is still better with a 20 % lower current density and an anodic OCP-shift, as well.

The addition of the silicon precursor does not show any improvement to the protection performance, neither as a hybrid coating nor as a multilayer system. Since the best results can be obtained with the monolayer ZrO_2 film, there is no need for unnecessary complication of the deposition process.

1.4 Zirconium oxide coatings with hydroxypropyl cellulose (ZrO_2-HPC)

It was found that the amount of acetyl acetone has a significant effect on film porosity of ZrO_2 coatings. Therefore experiments with the stabilizing agent HPC were done to investigate whether a similar dependence occurs and how the ability of HPC to decrease the particle size affects the porosity of the coating.

1.4.1 Effect of HPC concentration

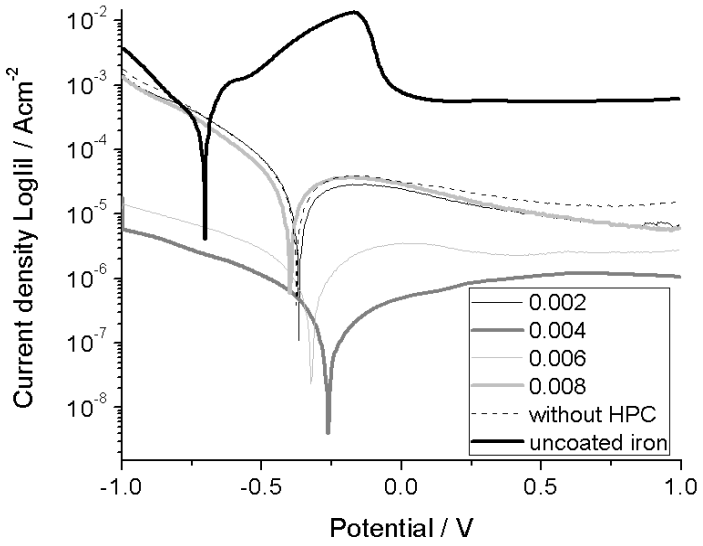

Fig. 53a Effect of HPC molecule (80,000 g/mol) concentrations (g/l) on current density

Fig. 53a shows potential scans for ZrO_2-coated iron samples treated at 673 K and prepared with different concentrations of HPC. It can be seen that the HPC concentration has a considerable effect on the coating quality and the lowest current density corresponds to the HPC concentration of 0.004 g/l. This indicates that this concentration promotes a compact and homogeneous structure with a strongly reduced inner porosity. Interestingly both lower and higher HPC concentrations lead to increased metal dissolution, indicating very porous film structures. For better visualization the maximal current density peaks are plotted against the HPC concentration in fig. 53b.

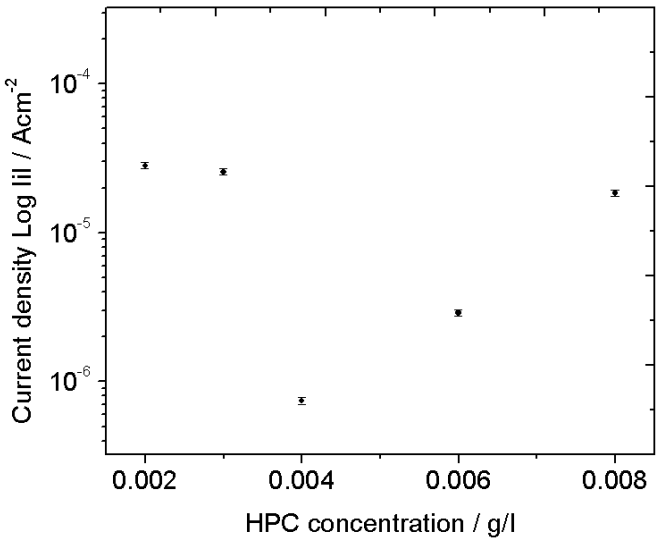

Fig. 53b Current densities at different HPC concentrations

This graphic reveals that similar to the correlation found for acetyl acetone there is an optimum HPC concentration of 0.004 g/l that provides the most compact and dense film structure. Again a small variation of the stabilizer amount has a major effect on the final coating structure. It is very likely that the ratio between precursor and stabilizer determines the number of reactive sites on the precursor molecule during gelation phase according to the number of substituent's connected to the metal atom [32]. Low HPC concentrations might not provide enough stabilization while higher concentrations can reduce particle mobility during polycondensation and result in increasing flocculation. Therefore the stabilizer amount controls also the shape and density of the final network structure. The quality and degree of this change was further investigated with SIMS and XRD and will be discussed in detail in chapter (5,6).

1.4.2 Effect of heating temperature

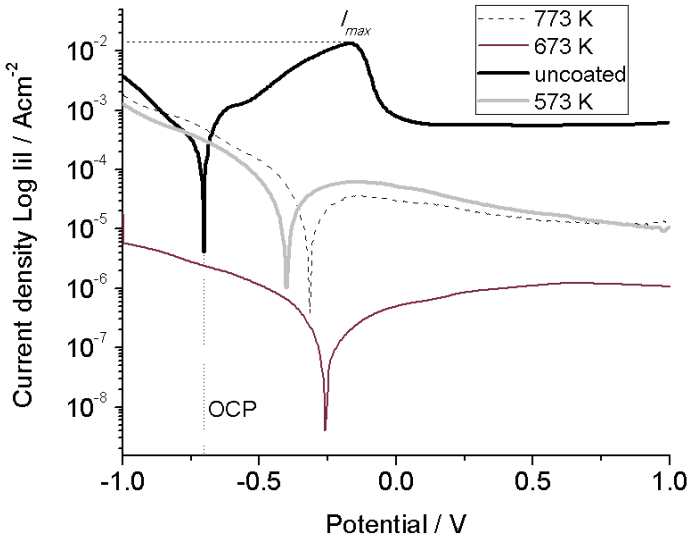

Fig. 54 Potential scans of ZrO_2-HPC coatings treated at different temperatures

Potential scans of coatings prepared with zirconium propoxide and hydroxypropyl cellulose (0.004 g/l) are shown in the fig. 54. The samples have been dried at different temperatures. The maximal current density peak of uncoated iron is used as reference. The 573 K sample shows a considerable reduction of approximately 2 orders of magnitude compared to the uncoated material; however, there is still a certain amount of polymeric compounds and solvent remaining in the film material. Because of incomplete evaporation of these residues the densification progress of the coating material is not finished yet and a moderate porosity persists in the film. At 673 K an exceptional low current density can be found. It is reduced by more than four orders of magnitude compared to the blank sample, indicating a minimum porosity of the coating system ZrO_2/HPC. On the other hand, the higher temperature of 773 K does not result in a further decrease of porosity but, on the contrary the current densities rise again. This might be related to stress phenomena during the heating procedure. This is again a similar behavior like it was observed for acetylacetone stabilized coatings. Again the film with the lowest porosity is obtained at a moderate heating temperature.

1.4.3 Effect of molar weight of HPC

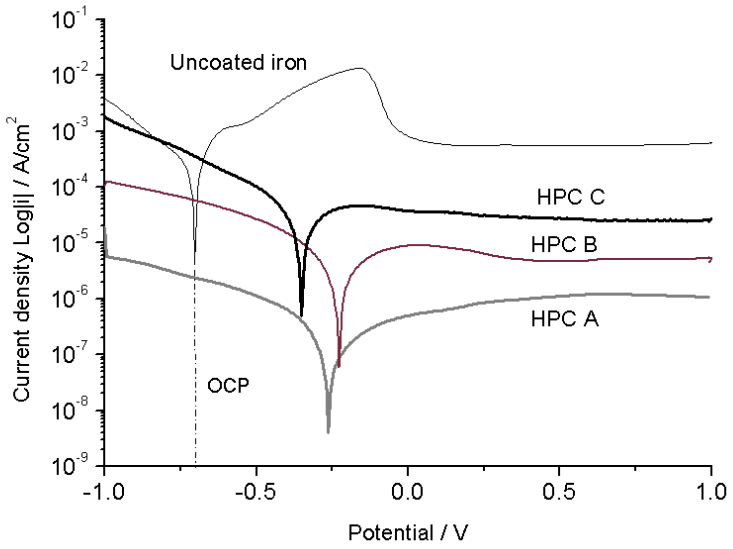

Fig. 55 Potential scans of coatings prepared with zirconium propoxide and different HPC molecules

Three kinds of HPC with different molar weight have been investigated to determine the influence of the molecule size of the stabilizer on the structural change of the film material. The coatings were prepared with zirconium propoxide and an HPC concentration of 0.004 g of HPC per liter of ethanol. The letters A, B and C, correspond to the molar weights (MW) of HPC molecules: 80,000; 100,000 and 370,000 g/mol, respectively. As can be seen there is a significant effect on the current densities and obviously a lower molecule size is advantageous for the formation of low porous coatings. Lowest dissolution current is found for sample A with 80,000 g/l and the current increases with growing molecular weight from 100,000 (B) until 370,000 (C). The different currents densities shown by the HPC molecules can be explained because very long polymer chains can overcome the saturation of the particle surface coverage. In this case the bridging between particles in form of flocculation becomes inevitable, reducing thus the stabilization and increasing defects (porosity) on the coating structure [31]. However, low-weight HPC molecules posses better surface contact around the particles surface [31,32,97-99],

reducing the particle size and resulting in better stabilization and lower dissolution current densities.

1.4.4 Hybrid coatings

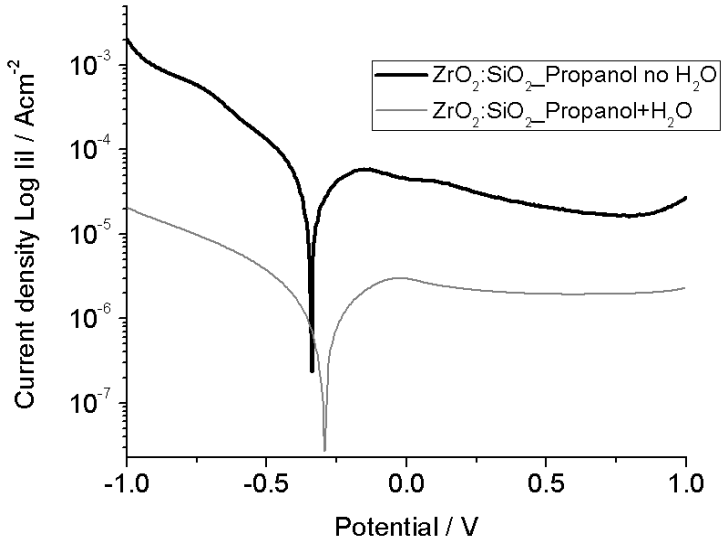

Fig. 56 Potential scans of hybrid coatings prepared of ZrO_2 and SiO_2 basis and heated at 673 K

In aqueous sol-gel processes water acts as solvent and ligand, as well. Oxygen for the formation of the oxidic compound is supplied by water molecules. In nonaqueous systems, where intrinsically no water is present, the oxygen for the metal oxide is provided by solvents or the organic constituent of the precursor [4, 104]. Hybrid coatings were prepared with and without water according to table 6 in order to find out which preparation way provides the structure with the lowest porosity. Potentiodynamic scans of samples prepared with propanol and with/without water as solvent and with 0.004 g/l HPC are shown in fig. 56. The sample with H_2O appears to be more dense (low porosity) and its maximum current density peak was reduced by two orders of magnitude in comparison to the sample without water. This indicates that in this case the absence of water limits the formation of dispersed particles and oxygen-metal-oxygen bonds specifically for the low reactive silicon precursor. This results in a porous and poorly stabilized structure.

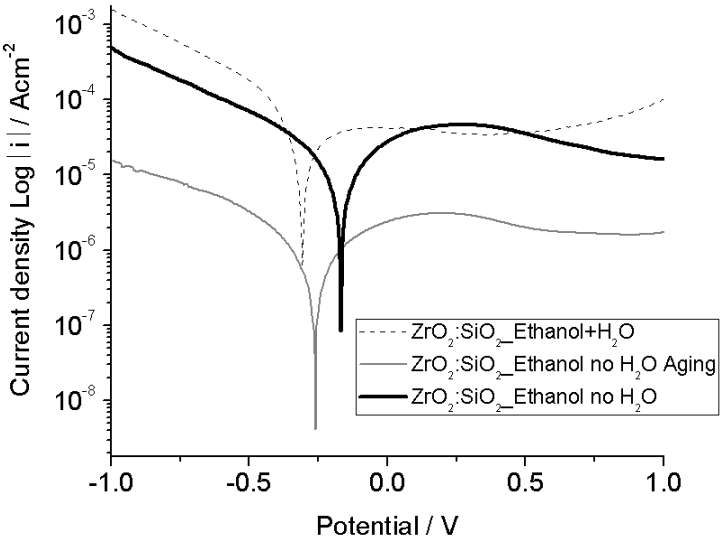

Fig. 57 Potential scans of hybrid coatings prepared with Zr and Si alkoxides and heated at 673 K

A similar pair of samples was prepared with ethanol instead of propanol. An additional aging step was introduced for a third sample to investigate whether the increased condensation time could overcome the lack of water. Current densities are shown in fig. 57. Both samples prepared with and without water show similar current densities with a small OCP-shift for the sample without water. Considerably lower current densities are found for the sample that was aged for three days. The resulting coating structure provides a major increase in protection performance with a further reduction of current density. During film preparation sometimes a problem occurred because the sol showed visible alteration before the heating step resulting in inhomogeneous films. The sol containing water showed a reduced life time because after 3 hours significant precipitation of the precursor material occurred. HPC acts in nonaqueous as surfactant providing stabilization in absence of water [104].

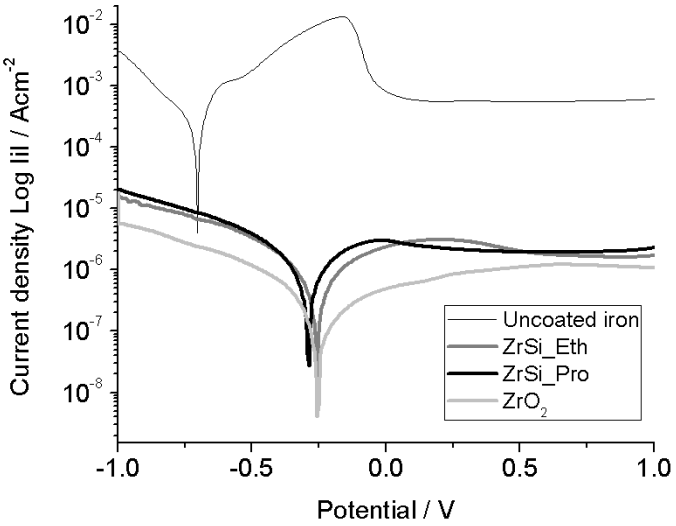

Fig. 58 Comparison of ZrO_2-SiO_2 hybrids coatings and pure zirconium oxide films

Fig. 58 summarizes the experiments about the effect of water content in the sol. It can be seen that the best hybrid coatings show a considerable reduction of current densities but cannot compete against the single precursor sol which still provides the lowest porosity. A similar result was found for acac-stabilized coatings where the best protection performance was also found for the pure precursor. It might be that the different precursor materials are not fully compatible resulting in a less uniform structure or increased susceptibility to stress during the heating procedure. Obviously the best results are obtained with the simple sol composition and the more complex sols showed no further advantage.

1.4.5 Steel samples

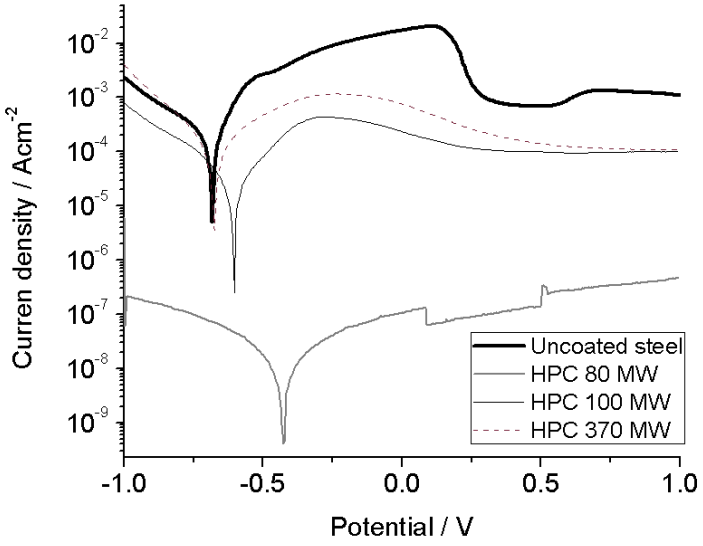

Fig. 59 Potential scans of construction steel coated with ZrO_2-HPC measured in sodium acetate/acetic acid buffer 0.1/0.01M

The application of HPC stabilizer in zirconium oxide coatings has probed good results not only on iron but onto construction steel as well as shown in fig. 59. Only the relevants coatings were used to test the behavior on this material. The porosity and current density were also reduced by the coatings.

III. Film morphology and structure

For a better understanding of the film constitution and to obtain more details about the effect of the stabilizing agents and other parameters, surface and structure characterization methods have been applied.

1. Scanning electron microscopy (SEM)

Physical characterization of the sample surface has been verified with SEM microscopic observations. Coatings prepared with zirconium propoxide and acetyl acetone and hydroxypropyl cellulose as stabilizing agents have been investigated.

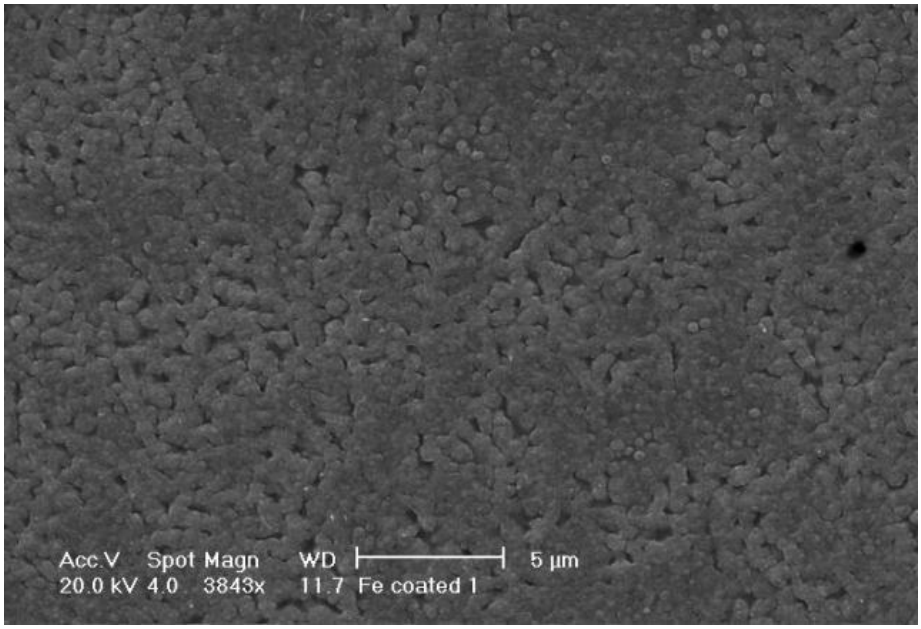

Fig. 60 SEM image of the coating prepared with Zr-propoxide and acac as stabilizer heated at 573K

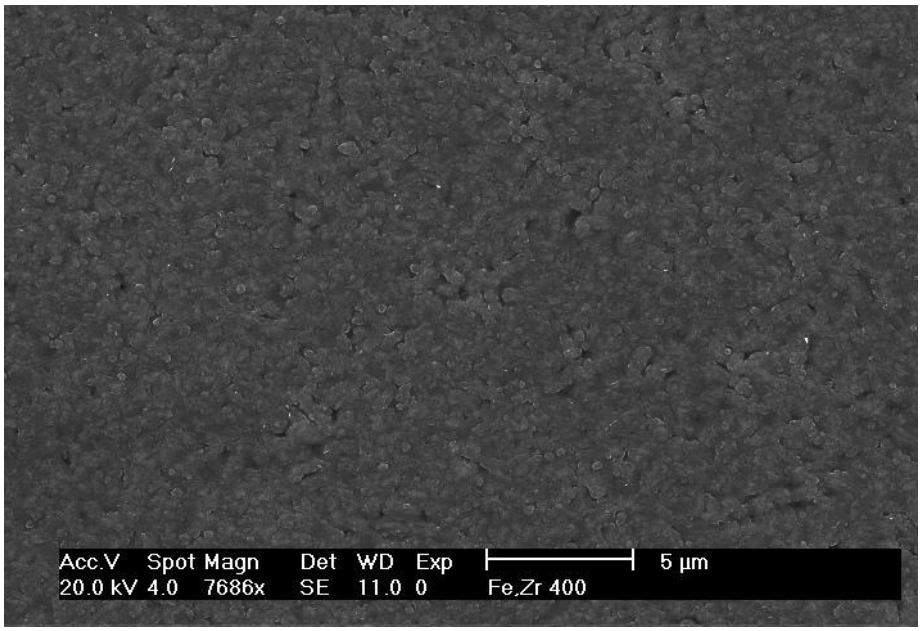

Fig. 61 SEM image of the coating surface for samples prepared with Zr-propoxide and acac and heated at 673 K

Fig. 60 and fig. 61 show SEM pictures of zirconium oxide films, stabilized with acac and heated for 1 hour at 573 and 673 K, respectively. The sample treated at 673 K shows a more compact structure with fewer cavities in comparison to the 573 K sample. This supports the results of electrochemical porosity

characterization but on the other hand SEM gives only an image of the superficial morphology and not of the inner structure of the coating. The obviously more compact structure supports the idea that higher temperature leads to the formation of a denser network with lower porosity. On the other hand higher temperatures often come along with stress phenomena and crack formation that can result in deterioration of the protective film. The SEM pictures suggest a well distributed, homogeneous coating structure with smaller particle size for higher temperatures but for the evaluation of the sample's protection performance the piercing porosity over the whole film thickness has to be considered (see II. 1).

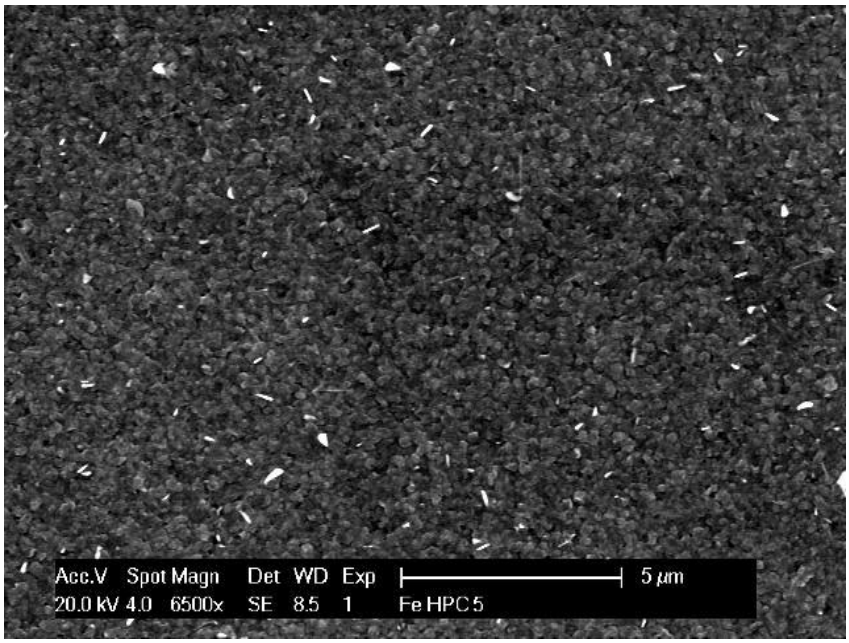

Fig.62 SEM image of a coating prepared with Zr-propoxide and HPC as stabilizer heated at 673K

The use of HPC as stabilizing agent leads to an even finer grained structure as can be seen in fig. 62. The particle size seems to be further reduced compared to acac-samples. This supports the ability of HPC to decrease particle size and porosity as well. In the fig. 63 a magnification of the above image is shown for better visualization.

.

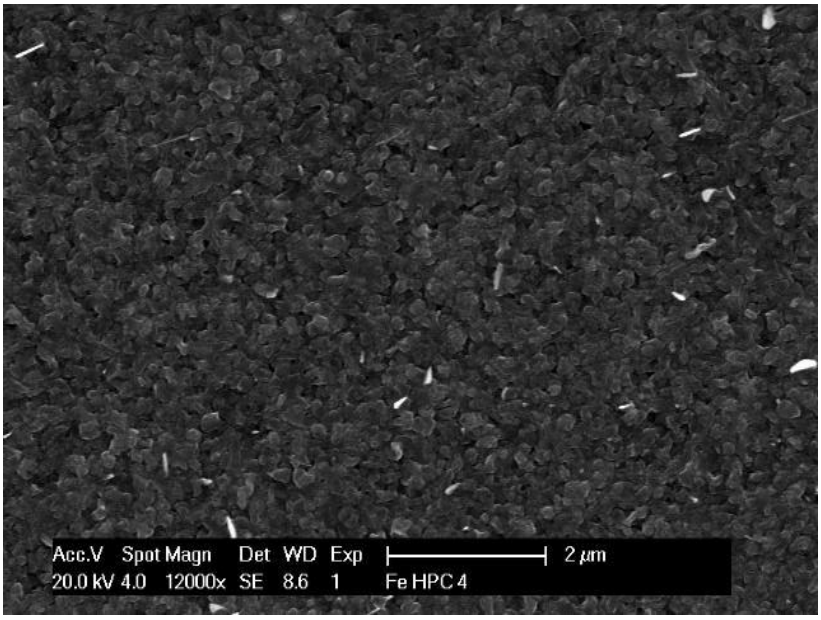

Fig. 63 SEM magnification of the image 62

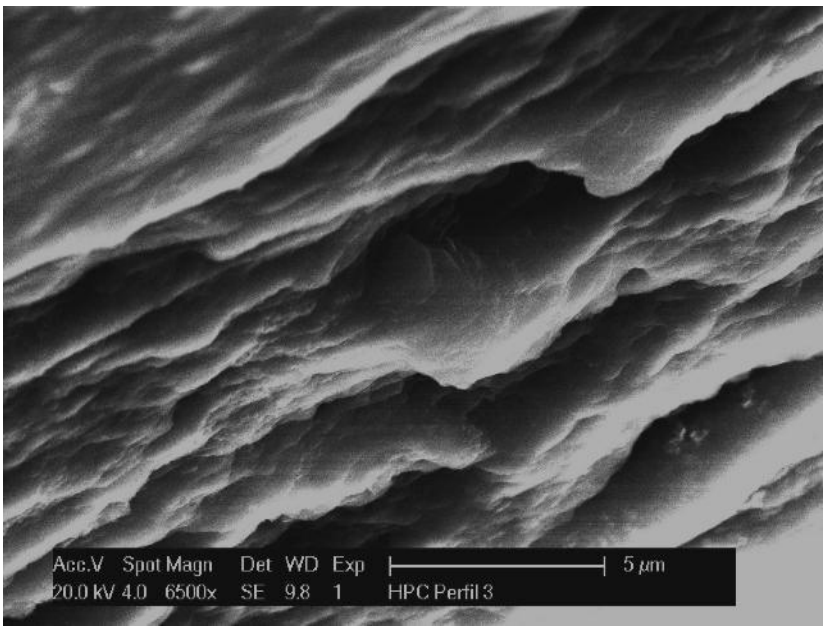

Fig. 64 SEM image of the edge for the sample shown in figure 62

A scanning electron microscopy image from the edge of the coating is shown in fig.63. The film structure looks like irregular elevations constituting of a species of an amorphous mass with different form and slopes.

2. ESMA/EDX measurement of element distribution

Additional characterization of film composition was done on the sample surface with ESMA and EDX. Fig.65 shows an image of the element distribution of

zirconium and oxygen. The brightness corresponds to the intensity of the observed element. The picture on the left hand side shows a homogeneous distribution of the main precursor element zirconium, verifying the uniformity of the deposition process. There is a light texture visible in the oxygen picture on the right hand side that may arise from deeper coating regions, probably the interface zone in contact to the iron/iron oxide substrate surface. Additional SIMS measurements were done to determine the nature of this effect (see chapter SIMS).

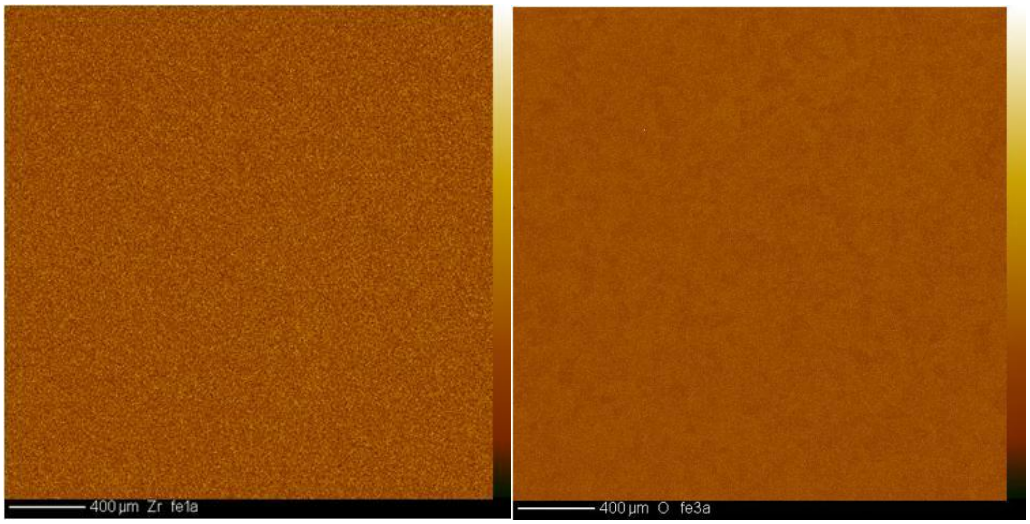

Fig. 65 ESMA of zirconium and oxygen made on coated samples

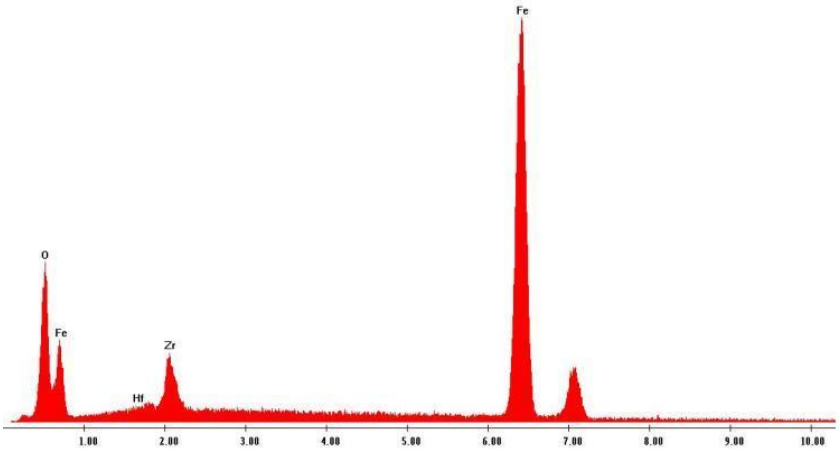

Fig. 66 EDX of ZrO_2 coating prepared with HPC=0.004g/l as stabilizer heated at 673K

In fig. 66 the K_L peaks of Zr, Fe, O and Hf (usually accompanied with Zr) are shown as received from EDX measurement. The small peak next to the bigger Fe signal corresponds also to a low intensity iron signal. Scans were made in different parts of the surface showing the same results. This method imparts a qualitative identification of the coating elements. This characterization proves the existence of a zirconium oxide layer on the coating surface. EDX measurements were also used at TEM and XPS characterization.

3. X-ray photoelectron spectroscopy (XPS) analysis

A problem of thin film analysis is the fact that many methods such as EDX deliver information from a certain depth of the material depending on the energy of the exciting ions or photons. In order to characterize the element composition in the upper surface region of the coating (few nanometers) XPS has been applied. Samples coated with zirconium n-propoxide and stabilized with acetyl acetone and hydroxypropyl cellulose have been characterized.

3.1 Samples prepared with acetyl acetone

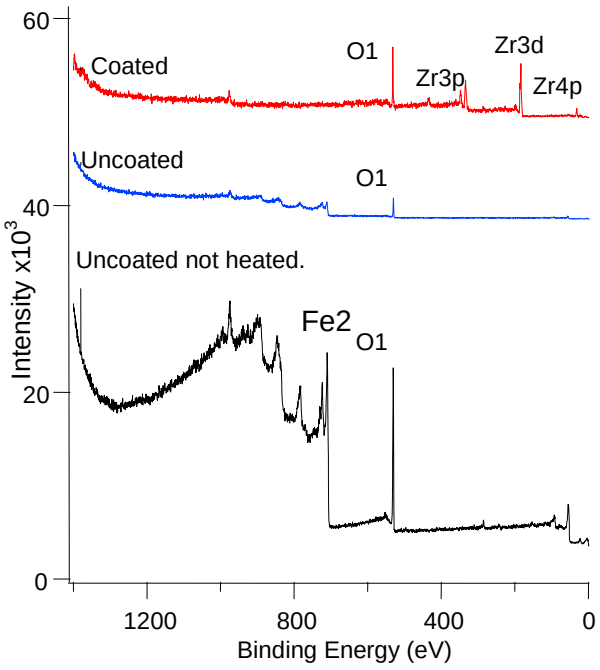

Fig. 67 XPS overview of coated and uncoated iron samples

Fig.67 shows different XPS results for coated and uncoated iron samples prepared with zirconium n-propoxide and acetyl acetone. All samples were sputtered to clean the surface. The curve corresponding to coated iron which was heated at 573K shows intensities of zirconium and oxygen. The Kα signal of Zr3d spectrum and weaker intensities as Zr3p and Zr4p can be clearly identified at low binding energy. The signal of oxygen O1s spectrum is also observable around 520 eV which indicates formation of zirconium oxide on the surface. Uncoated iron heated at 573K and the sample kept at room temperature (not heated) show only oxygen and metallic iron (Fe2p) spectra as an effect of iron oxidation. Both samples were used as comparison and to observe possible iron oxide formation on the sample surface when the sample is heated at the same temperature.

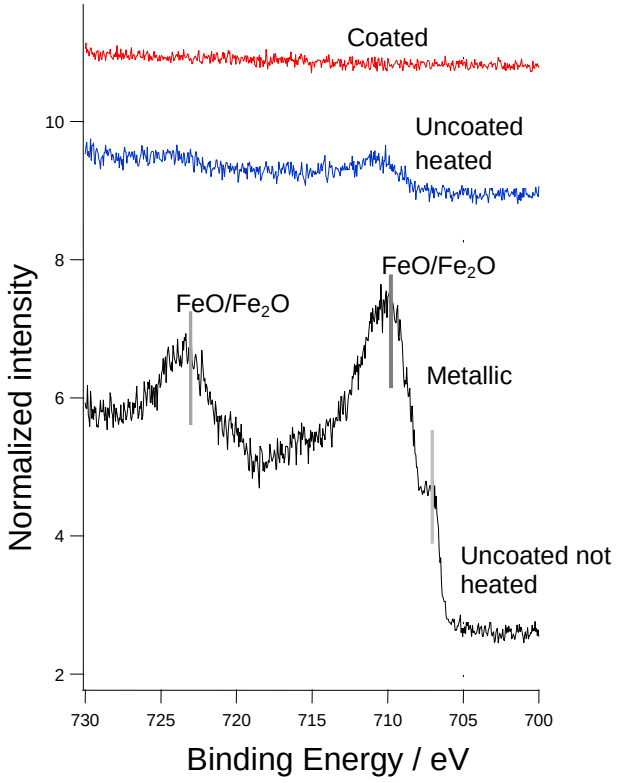

Fig. 68 Fe 2p spectrum of the Fe samples (spectra normalized to the background intensity at ~702eV)

Fig. 68 shows a Fe2p spectrum for the samples described above. Metallic iron is identified at a binding energy of 707 eV and iron oxides (FeO/Fe_2O_3) are localized at binding energies of 710.9 and between 724-725 eV according to the NIST online database and the XPS Handbook [82]. This result can be also indexed as the phase Fe_3O_4 as result of the iron oxidation. In the case of uncoated heated sample only a small peak of iron oxide can be seen around 710 eV, probably because of magnetic interference with the detector during the measurement. However, for the coated sample it is not easy to distinguish at this depth the existence of iron oxide.

3.2 Samples prepared with Hydroxypropyl cellulose (HPC)

Fig. 69 shows an overview of one iron sample prepared with zirconium n-propoxide and HPC = 0.004 g/l and of an uncoated not heated sample as well. The coated sample was heated at 673K. Signals of Fe, Zr, C and O are emitted which indicate the existence of a very thin ZrO_2 layer on the surface of the Fe sample. According to the binding energy, Fe is oxidized and metallic Fe is localized at ~707eV. The existence of iron oxide on the upper coating surface can be a product of diffusion processes between substrate and coating during the heating procedure or of the surface roughness.

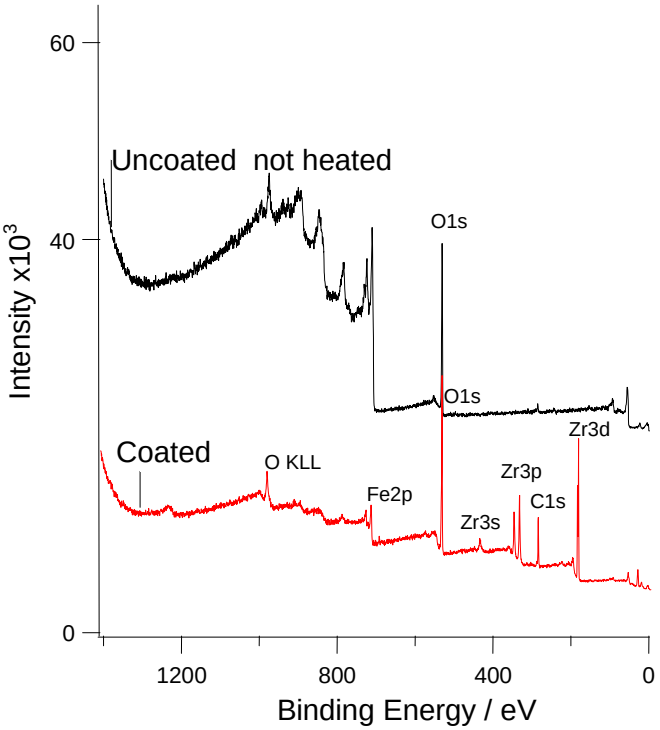

Fig. 70 Survey spectra of coated and uncoated iron samples prepared with HPC as stabilizer

Emissions of FeO and Fe_2O_3 can be observed at binding energies of 710.9 and 724 eV approximately. According to the data base for Fe2p spectrum [82] Fig.71, iron oxide peaks can be indexed with respect to the orientation of the spin in the orbital p as the doubling $2p_{1/2}$ and $2p_{3/2}$, respectively (fig.72).

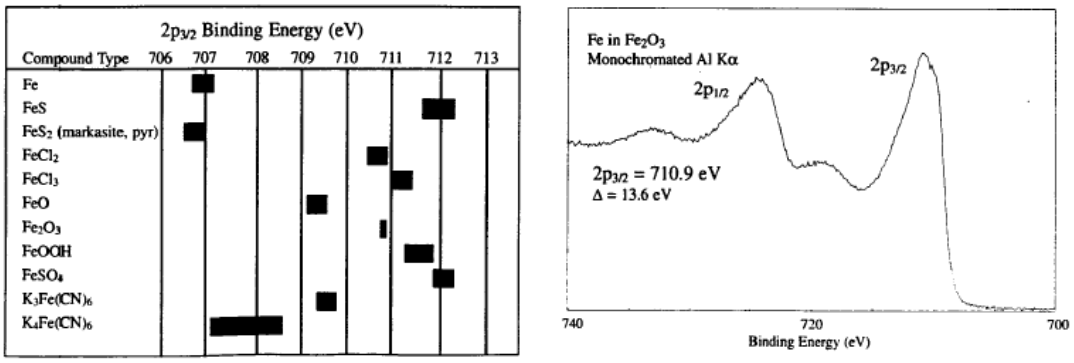

Fig. 71 Binding energies of iron [82]

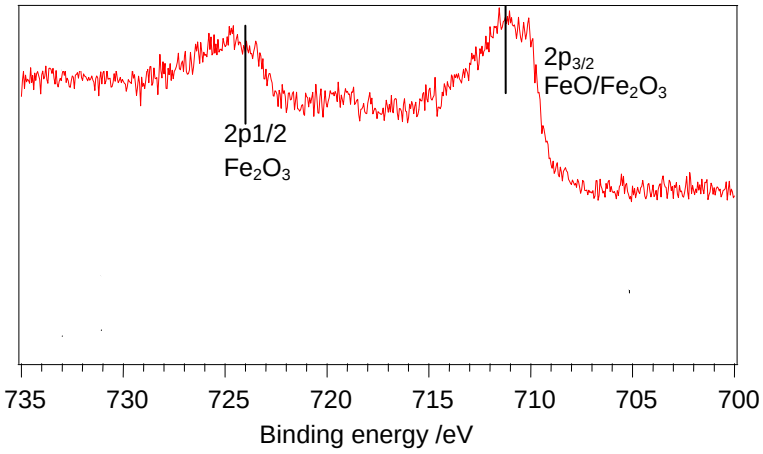

Fig. 72 Fe 2p spectrum of Fig. 70

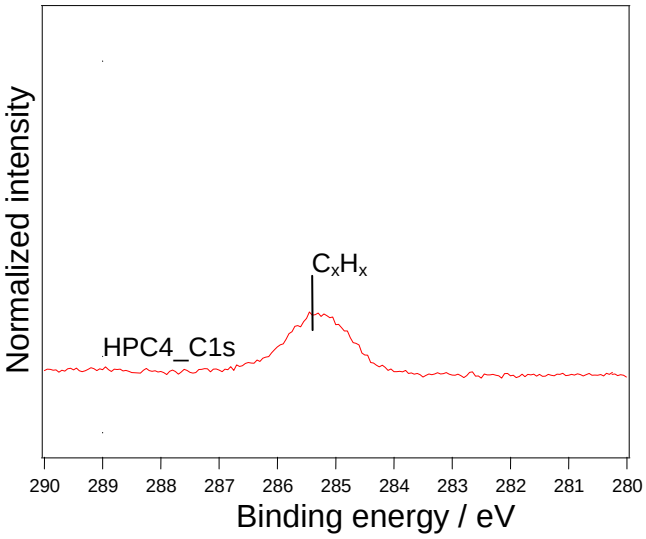

Fig. 73 Carbon C (1s) spectrum of the Fig. 70

The C (1s) spectrum in fig. 73 confirms the existence of remaining organic compounds in the coating material after heating at 673 K. The observed peak can be related to the carbon between the binding energies of 286 and 284 eV. According to the carbon data base this emission corresponds to carbon and hydrogen (C_xH_x) compounds like: C-O-H, C-H or C=O which are residues of the HPC polymer as described by [39,100].

Table 5. Binding energies of zirconium [82]

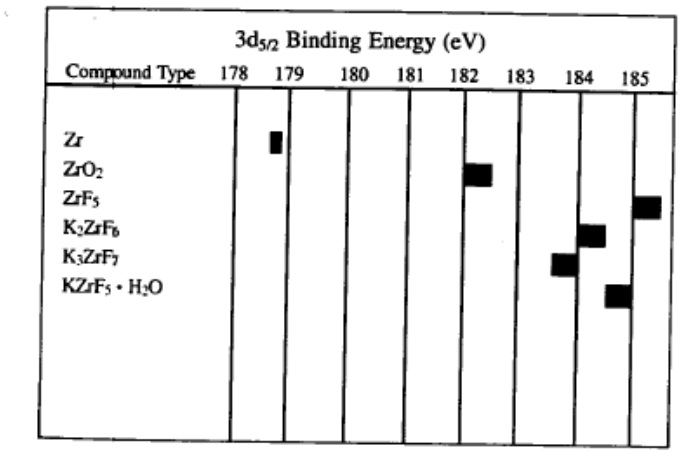

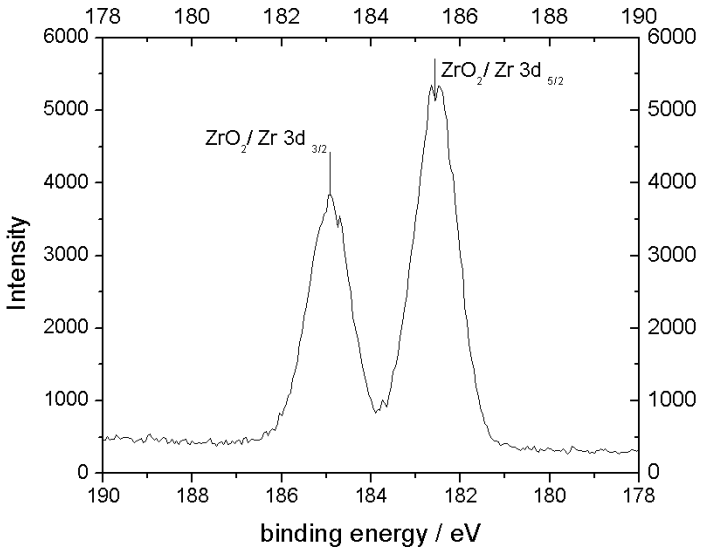

Fig. 74 Zr 3d spectrum of the coating in fig.70

Table 5 shows the binding energies of zirconium components obtained from the XPS database [82]. According to these values the zirconium emissions shown in the fig. 74 and localized at the binding energies of 182.3 and 185 eV, are zirconium oxide (ZrO_2). The orientation of the spin allows to achieves these as ZrO_2 (Zr $3d_{5/2}$ and $Zr3d_{3/2}$) coupling, respectively.

4. Crystalline structure analysis with X-ray diffraction (XRD)

The influence of heating temperature on the crystalline structure of the zirconium oxide coatings was investigated with X-ray diffraction. Samples were coated with zirconium propoxide and acetyl acetone as stabilizing agent and heated at 573, 673, 773 and 873 K for one hour.

4.1 Samples prepared with acetyl acetone

Fig.75 shows a comparison of X-ray diffraction measurements of two iron samples coated with zirconium tetra-propoxide and acac after heating at 573 and 673 K, respectively. An inclination angle of omega ω = 3°, using a theta /2° constant was applied. At 673 K the films reflect more crystalline ZrO_2 in tetragonal and monoclinic phases than for samples treated for two hours at 573 K. It is supposed that the phase transformation of crystalline (tetragonal-monoclinic) zirconium oxide occurs at heating temperatures between 673-773 K [56]. This explains the appearance of the K_α reflex of ZrO_2 at approximately 28° for the sample treated at 673 K. This reflex is hardly visible in the diffractogram of the 573 K sample because this temperature is too low to form greater amounts of crystalline phases.

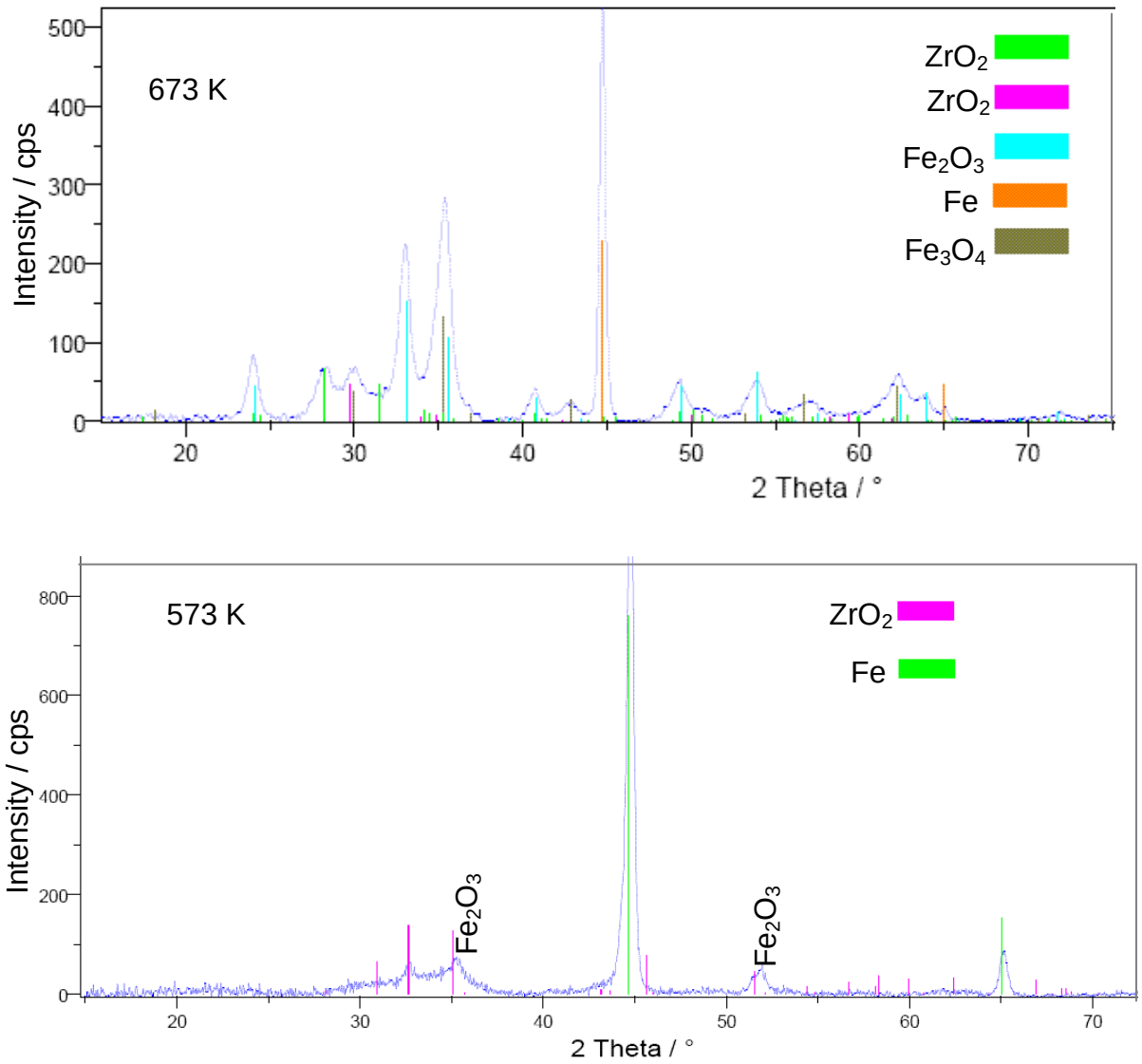

Fig. 75 XRD comparison at omega ω = 3° of coated iron samples heated at 573 and 673 K for 1 h in furnace

Both graphs shows also iron and iron oxide reflexes. At 573 K only α-Fe_2O_3 could be observed. When the temperature is further increased up to 673 K an additional phase of magnetite (Fe_3O_4) can be observed. The appearance of Fe reflexes results from X-ray reflections at deeper layers of the coating and the substrate surface.

4.2 ZrO_2-acac samples heated at higher temperatures

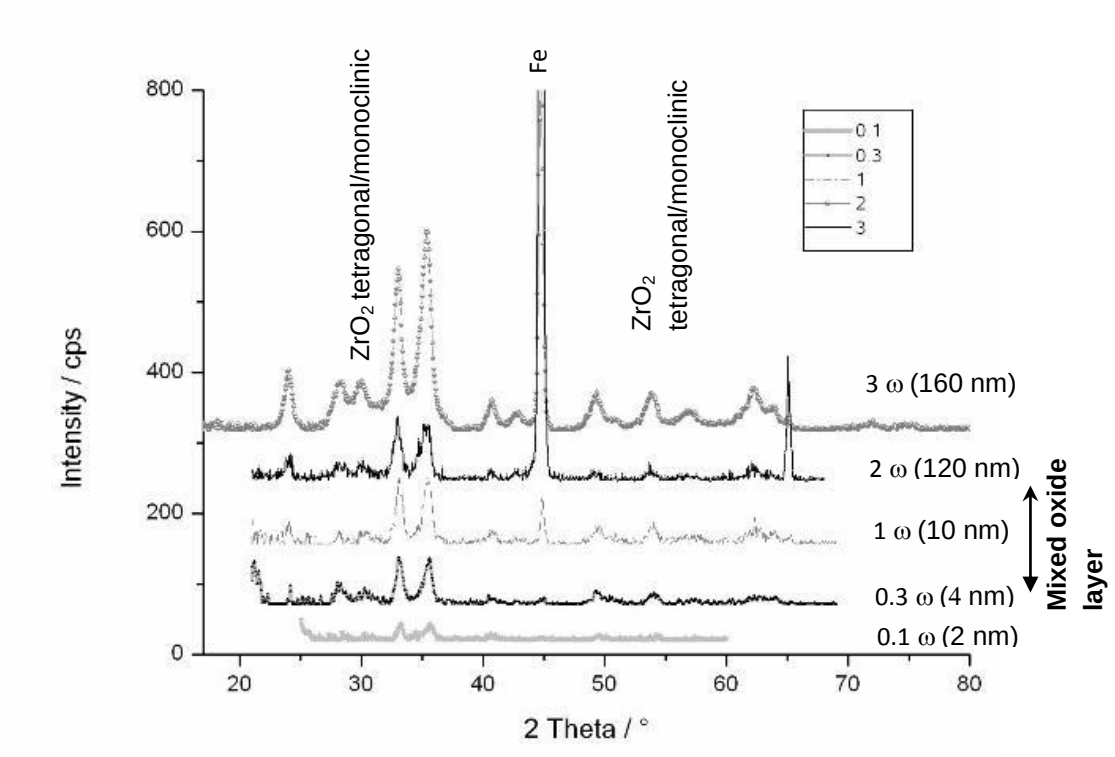

Fig. 76 XRD scans at incidence angles omega = 0.1°; 0.3°; 1°; 2° and 3° of ZrO_2-coatings after heating at 673 K

XRD measurements were made at different incidence angles to obtain information about the crystalline structure at different depths in the coating material. Higher incidence angles represent reflexes from deeper film regions. As can be seen in Fig.76 with an inclination angle of omega $\omega = 0.1°$, ZrO_2 reflexes appear from the upper few nanometres of the coating surface. This reflex is clearly detectable at approximately 28° through the Kα reflex of zirconium oxide. At greater depths additional ZrO_2 reflexes with less intensity can be observed at 51 and 52° degree. However the clearest indication of crystalline phases corresponds to the high intensity reflex. Iron oxide phase's magnetite and hematite (Fe_3O_4, Fe_2O_3) appear at the same inclination angle. It can be seen in the diffractogram that in deeper film regions (120 – 160 nm) at the interface zone both reflexes from iron / iron oxide and zirconium oxide appear together. This might indicate the formation of a mixed layer consisting of iron oxide and zirconium oxide as well.

To verify whether these oxide reflexes originate from the same depth the relative position of this layer was calculated for a coated iron sample treated at 673 K in relation to the Kα reflex of ZrO_2 and Fe_2O_3 reflected at different inclination angles [13]. This means that the thickness was estimated with X-ray diffraction by the penetration depth of photons with an energy of 8000 eV as a function of the incidence angle ω. Below a certain angle of incidence only the reflections of the film were visible. The mixed oxide layer is located approximately between 4 nm and 120 nm from the coating surface as indicated in with the arrow in fig. 76. The formation of the mixed interlayer is most likely a product of the diffusion processes between the coating material and the bulk iron substrate during the heating procedure. It is supposed that the mixed layer consists of both crystalline and amorphous phases of zirconium and iron oxide which will be described in the next chapter.

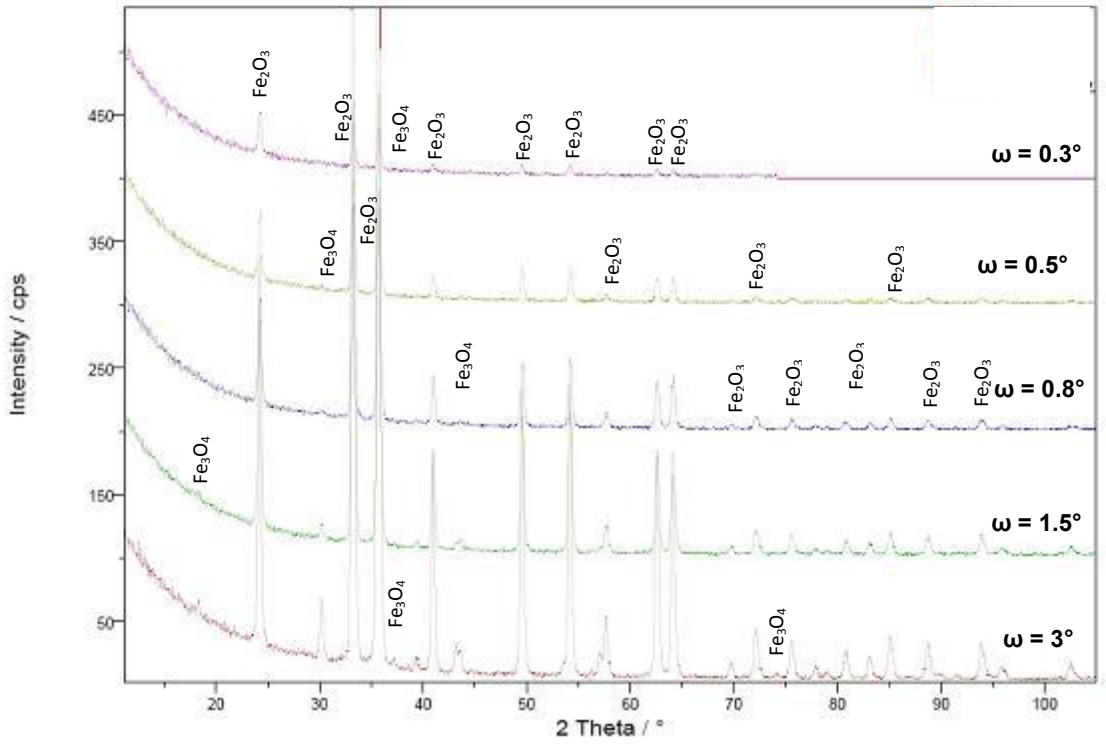

Fig. 77 XRD of uncoated iron measured at ω = 3 and heated at 873 K

In addition supplementary X-ray diffraction measurements were carried out for samples treated at higher oven temperatures between 673–873 K. This experiment was made without coating to investigate the behaviour of growth

and possible influence of iron oxides on the film properties. Samples showed a formation of more iron oxide reflexes of hematite and magnetite as shown in fig.78. The increase of the intensity of the signal of iron oxide can be related to increased oxidation. These intensities are proportional to the heating temperature and to the inclination angle omega as can be observed in fig. 77. Likewise new reflexes appear with increases of the incidence angle. They are localized in a major proportion in deeper layers and are related to magnetite (Fe_3O_4). However, hematite (Fe_2O_3) is found throughout the sample. This effect can increase the oxide thickness as observed from removing the samples from the oven. This effect is also present in coated samples as shown in fig.76. When the samples were heated up to 873 K, defects on the edges with some stress-related cracks were observed. These can be undesirable for low temperature application.

4.3 Samples prepared with Hydroxypropyl cellulose

As described in the last chapter, the use of a stabilizer in the sol preparation has a major effect on the crystalline structure of the coating even at lower temperature [24]. Since HPC is known to promote the formation of crystalline nanoparticles, further investigations should prove whether any of such structures can be found in the prepared zirconium oxide coatings and whether they have a beneficial effect on the protective properties of the HPC samples with lowest porosity.

4.3.1 Effect of HPC concentration

Fig. 78 shows X-ray diffraction measurements of iron samples coated with zirconium propoxide and HPC as stabilizing agent. The concentration of HPC was varied from 0.002 to 0.008 g/l ethanol and the heating temperature was 673 K. All samples were measured at an incidence angle of $\omega = 3°$ and for HPC = 0.004 g/l inclination angle $\omega = 5°$ was also used to increases the detection range. The reflexes of crystalline (ZrO_2) were identified according to the crystal data base from the software and literature as monoclinic (a: 5.15070; b: 5.20280; c: 5.31560, β: 99.196; S.G.:$P2_{1/a}$) and cubic (a: 5.106=b=c)

[81,85,101]. These reflexes can be observed in fig.78 around 28° and are indicated with arrows.

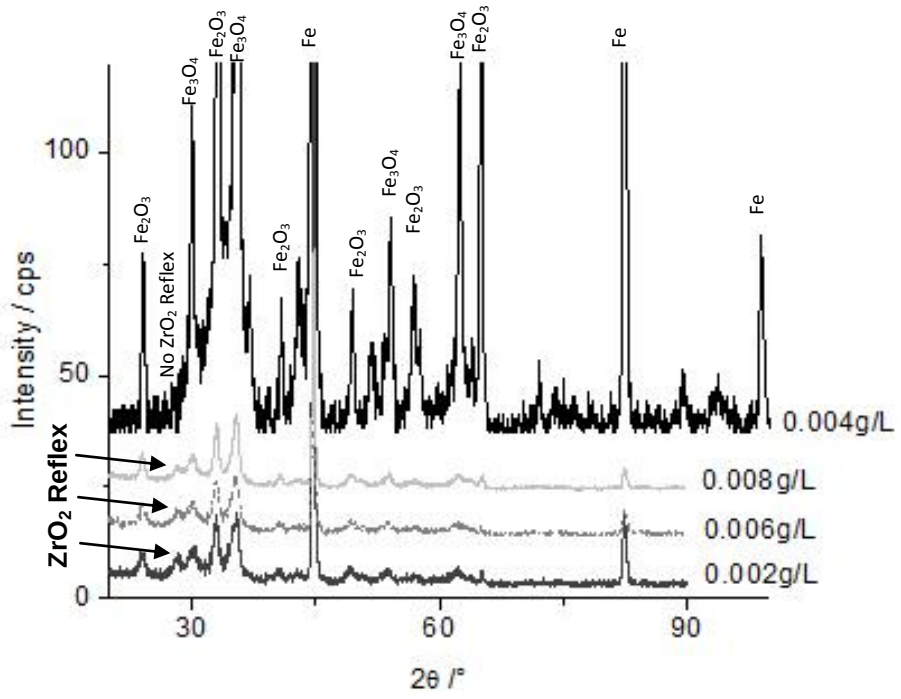

Fig. 78 Comparison of HPC (80,000 g/mol) samples measured at ω = 3° and heated at 673K

It can be seen that even a small variation of the stabilizer concentration specifically with HPC = 0.004 g/l has a significant effect on the crystalline structure of the coating. ZrO_2 reflexes for the HPC concentrations 0.002; 0.006 and 0.008 g/l can be easily identified. So the stabilizing agent promotes the formation of crystalline structure at lower heating temperatures [39].

There is one sample coated with a HPC concentration of 0.004 g/l that does not show the peak corresponding to the zirconium oxide phase at 28°. Possible explanations for this behavior are: a) the film structure is completely amorphous; b) the iron and iron oxide reflexes overlap and cover the reflexes of zirconium oxide; c) the texture or amount of crystalline material is too low for detection and d) the crystalline particles have a very small size and appear to be polycrystalline and undetectable by the X-ray diffraction measurements. In

order to find an appropriate explanation to this question, TEM measurements were made and they will be discussed in the following chapter.

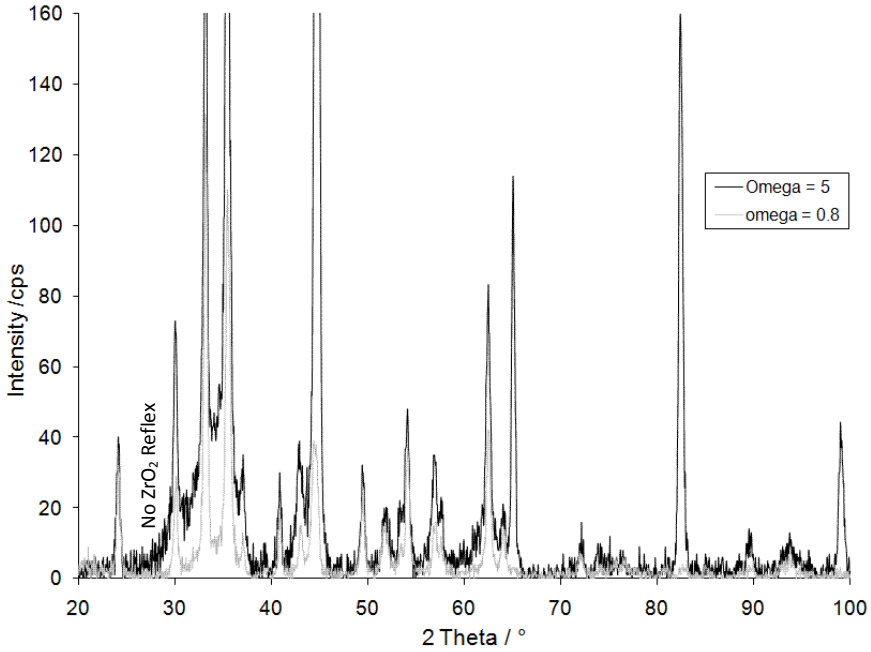

Fig. 79 Comparison of coated iron heated at 673 K (HPC = 0.004 g/l; 80 MW measured at $\omega = 5°$ and $\omega = 0.8°$

Fig.79 shows X-ray diffraction scans for two iron samples coated with zirconium n-propoxide and HPC as stabilizing agent. The samples were measured at incidence angles of $\omega = 5°$ and $\omega = 0.8°$ in order to detect zirconium oxide reflexes from different depths of the coating. However, no reflexes of crystalline zirconium oxide could be detected, neither in the upper region of the coating nor at the interface, close to the substrate. Only peaks corresponding to the phases Fe and Fe_2O_3 and Fe_3O_4 could be detected. This result supports the assumption that a HPC concentration of 0.004 g per liter of ethanol changes the internal structure of the coating material significantly. Further TEM measurements were carried out to reveal whether ZrO_2 is either amorphous or nanocrystalline.

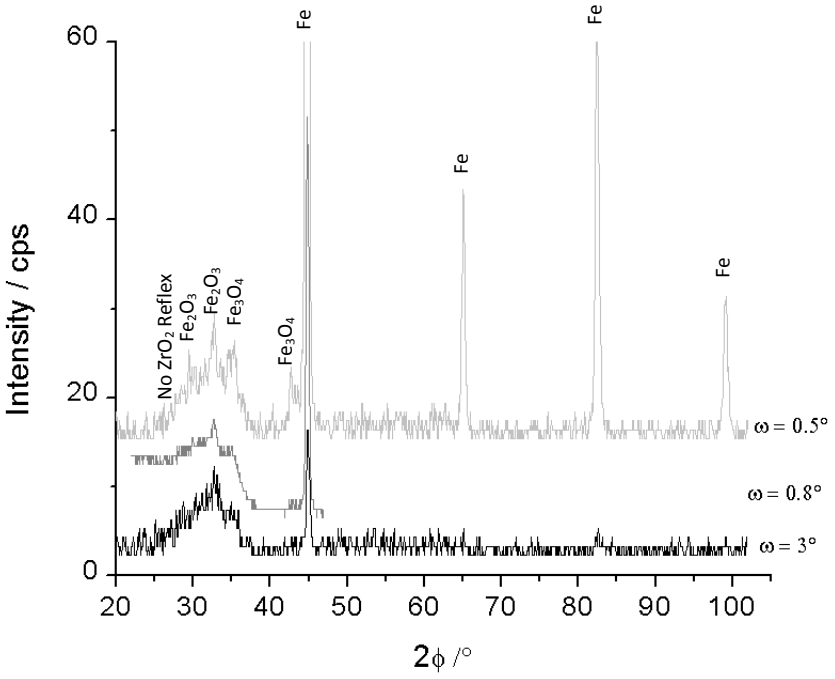

Fig. 80 XRD comparison for coated iron heated at 573 K (HPC = 0.004 g/l; 80 MW measured at ω = 0.05°; 0.8° and 3°

In order to investigate the effect of HPC in samples heated at a lower temperature like 573 K, XRD scans were made using three different incidence angles as shown in fig. 80. The higher intensities are found at an incidence angle of ω = 0.5° but only the phases Fe; Fe_2O_3 and Fe_3O_4 are detected. At this incidence angle the signals are received from a few nanometers of the coating surface and through the other two angles the information is received from deeper layers. However, no reflexes of ZrO_2 are detected at this heating temperature.

4.3.2 Effect of heating temperature

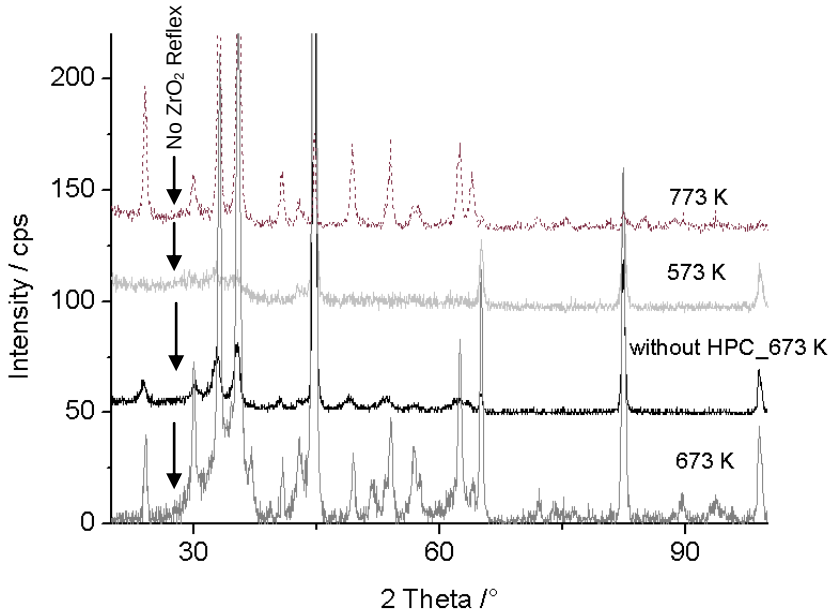

Fig. 81 XRD of coated iron heated at different temperatures and measured at $\omega = 3°$

Fig. 81 shows X-ray diffraction graphics for coated samples with zirconium propoxide together with and without HPC as stabilizer. They were heated at different temperatures in a furnace to investigate the effect of HPC and temperature on the crystalline structure. According to the fig.81 a similarity for all samples can be observed: no ZrO_2 reflexes are detected between 28-30° where the signal of ZrO_2 K-α always appears as observed in the case of acetyl acetone. Although in some cases the temperature is higher than 573 K for coated samples and heated at 673 and 773 K ZrO_2 crystalline is not detectable with X-ray diffraction.

4.4 Comparison HPC-acac coatings

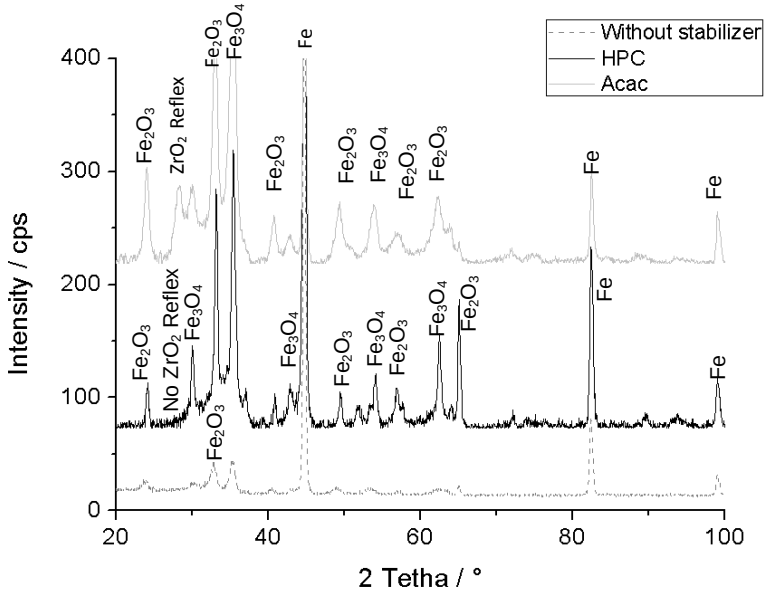

Fig. 82 Comparison between HPC, acac and no stabilized coatings

For better understanding the effect of the stabilizers a comparison of samples prepared with HPC, acac and a sample prepared without stabilizer is shown in fig. 82. All samples were heated at 673 K. The curve of acetyl acetone shows the crystalline phase of ZrO_2 around 28° corresponding to monoclinic and/or tetragonal as described above. However, in the case of HPC no reflexes of zirconium oxide crystalline have been detected.

On the other hand, the fact that the sample treated without HPC does not show crystalline ZrO_2 is probably related to the instability of the precursor zirconium propoxide during the polycondensation phase. Because of the absence of a stabilizer the phase transformation from amorphous to crystalline can not take place at low temperatures [56]. It is known that during the sol-gel process in the gelation and polycondensation stages the formation of the final structure begins and will be finalized during the heating step. However, zirconium materials require higher temperatures as 1443 K and 2643 K to reach crystalline phases, like tetragonal and cubic, respectively. The monoclinic phase is considered the low-temperature phase of stabilized zirconium oxide produced by displacive transformation of the tetragonal form between 1273-1473 K [56]. Usually higher

temperatures are necessary to reach crystalline structures; however, the use of stabilizing agents during the sol-gel process reduces the transition temperature allowing synthesis of crystals at lower temperatures [39]. In the case of HPC the double function with hydrophilic and hydrophobic parts stabilizes the zirconium oxide particles in nanocrystalline structures that could interferes its detection via XRD [31,32]

5. SIMS analysis

SIMS measurements were performed to obtain a more detailed view on the position of different layers and structures inside the coating material. The distribution of elements was investigated by means of depth profiles of the coated samples.

5.1 Zirconium oxide coatings prepared with acac

Fig. 83 shows a depth profile for a sample prepared with acetyl acetone as stabilizer. The molar ratio of precursor solution to acetyl acetone was 1:1.5. As shown in the graph, the expected elements of the coating material are all present in the film. An abrupt rise of iron intensity can be observed between 400 and 500 s sputter time that can be attributed to the formation of α-Fe_2O_3 which was found in the XRD-analysis. At the same time the intensity of zirconium decreases and remains constant together with iron until the substrate is reached after 1500 s. Obviously, the lower part of the coating contains a high amount of iron which wouldn't be expected from a homogeneous ZrO_2 film. Diffusion processes during the heating procedure between substrate and coating material must be responsible for the formation of this mixed layer that consists of iron oxide and zirconium oxide, as well.

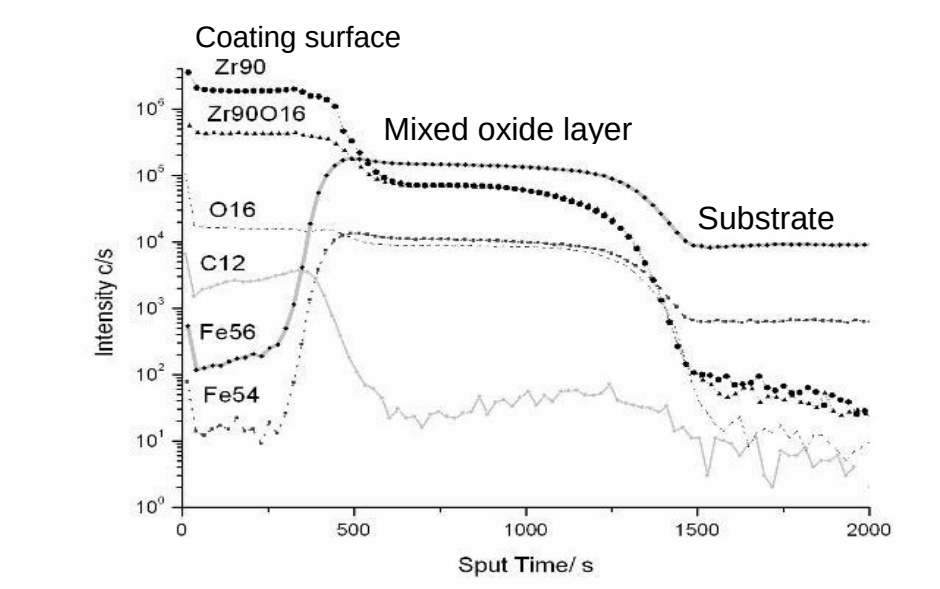

Fig. 83 Depth profile of acac-coated iron sample heated at 573 K for 1 h

As revealed by XRD, at 573 K the zirconium oxide layer remains amorphous, because the transition temperature has not been reached yet. There is also a certain amount of remaining organic components present as can be seen from the intensity of the C12 curve.

5.1.1 Effect of time and heating temperature

To get a better understanding of the mechanisms that are responsible for the formation of the mixed oxide layer the influence of heating temperature and time was further investigated with SIMS.
Fig. 84 shows the depth profile of a sample that has been treated in the same way as the one discussed in fig. 83 except for the heating time which was increased for another hour. The substrate is now reached after 2000 s compared to 1500 s afer heating for one hour.

Apparently, the thickness of the coating has increased but since the thickness was the same for both samples prior to the heating step, this effect must be a result of increased diffusion in either direction. This is supported by the thickness of the mixed oxide layer which has also expanded and ranges now up

to 1700 seconds of sputtering time. Correspondingly, the upper ZrO_2 region is reduced to almost the half of the thickness as in fig.83, the rise of iron intensity now appears already after 300 s.

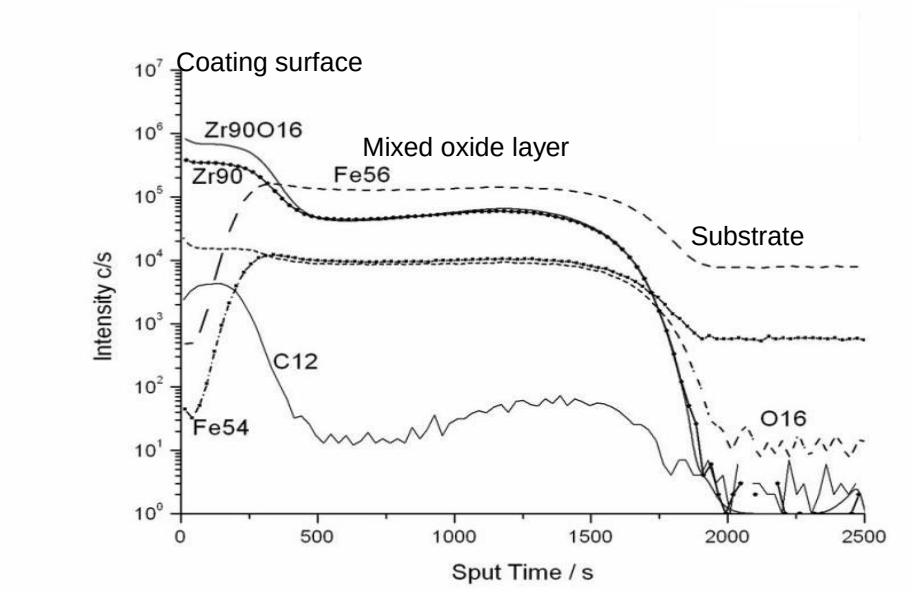

Fig. 84 Depth profile of acac-coated sample heated at 573 K for 2 h

Even a stronger effect than heating time can be found for the heating temperature as displayed in fig. 85. After heating at 673 K for 1 hour the overall film thickness seems to be the doubled compared to the 573 K sample (fig. 82). It takes now 4000 s of sputter time to reach the bulk substrate material and the mixed oxide layer has broadened further and expands now over almost the whole coating thickness.

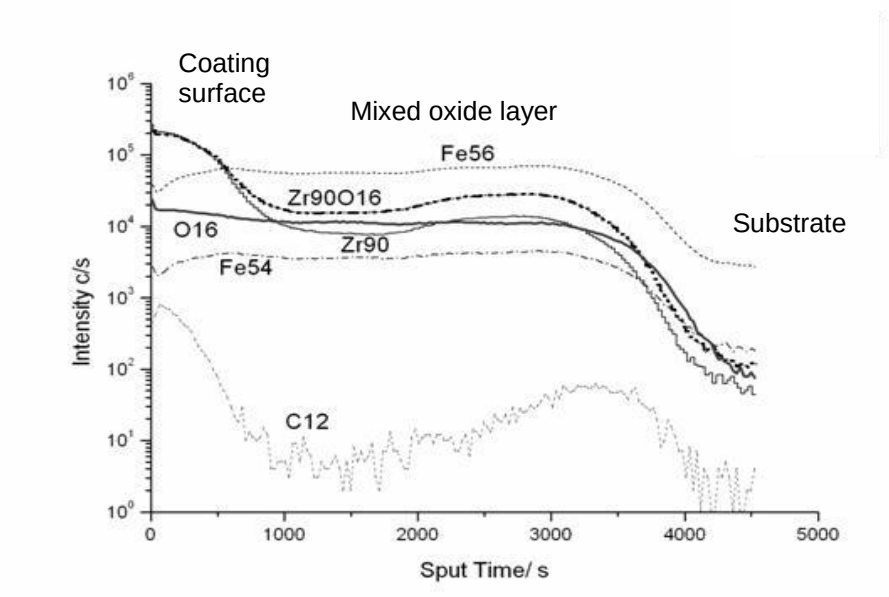

Fig. 85 Depth profile of coated iron heated at 673 K for 1h in furnace

At 673 K the diffusion is much more distinctive than after the increase of heating time and the mixed oxide layer which contains a high amount of crystalline ZrO_2 now expands deeper into the bulk substrate material. According to the electrochemical results of the 673 K samples it appears that the formation of the mixed layer plays a major role in the observed decrease of film porosity (see chapter 1 Results).

5.1.2 Effect of acetyl acetone concentration

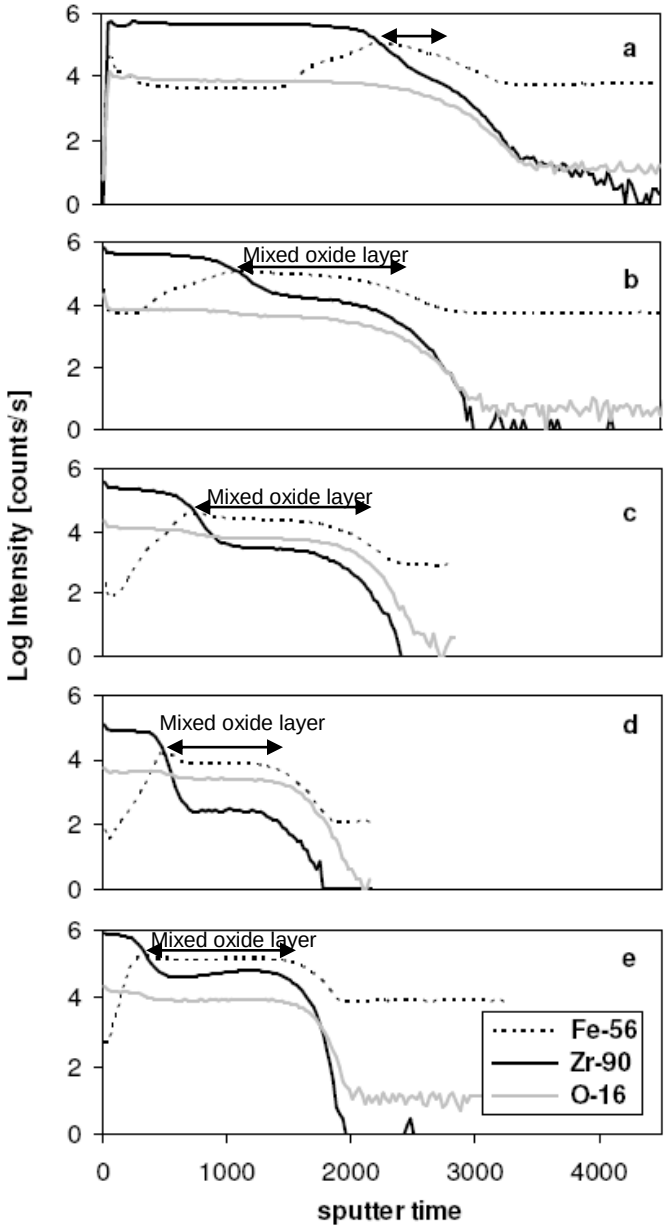

Fig. 86 SIMS profiles of coated samples with different molar ratios of acetyl acetone after heat treatment at 573K: **a)** acac:0 **b)** acac:0.5 **c)** acac:1.0 **d)** acac:1.2 **e)** acac:1.5 [24]

Fig.86 shows a series of SIMS depth profiles of samples with increasing acetyl acetone concentration in relation to the precursor zirconium n-propoxide. Only the intensities of the relevant elements of coating and substrate are shown:

Zr90, Fe56 and O16. It can be seen that the overall film thickness depends strongly on the acetylacetone concentration, as the sputter time until the substrate is reached decreases with rising acac-concentration. This effect was also verified with profilometry thickness measurements.
The thickness of the final coating decreases from 200 ±10 nm for samples prepared without acac down to 70 ±10 nm for samples prepared with a molar ratio precursor/acac of 1:1. More or less addition of acetyl acetone than 1:1 can contribute either to the formation of a $[Zr(O^{i}Pr)(acac)_3]$ complex without trans-stabilization or the regression to the instable precursor $Zr(O^{n}Pr)_4$ and a destabilization of the film structure will be inevitable as described in [36,102]. The formation of these instable compounds could affect the reactivity and evaporation rate of the constituents connected to the metal atoms during the heating process leading to a thinner or thicker structure. Interestingly the sample without acetyl acetone shows the smallest mixed oxide layer and the highest overall film thickness but also the highest porosity as the electrochemical experiments revealed.

Apart from the film thickness the general structure of the coating is the same for all samples: a zirconium oxide layer at the surface, followed by a mixed layer of zirconium and iron oxide and finally the iron substrate. The rise of the iron intensity shortly before the zirconium intensity drop is another indication for the presence of the mixed oxide layer, because the higher concentration of oxygen in this layer increases the number of secondary ions of iron, leading to a higher signal.

Similar to the samples discussed before the pure zirconium oxide part decreases continuously whereas the mixed oxide layer grows with increasing acetyl acetone concentration.

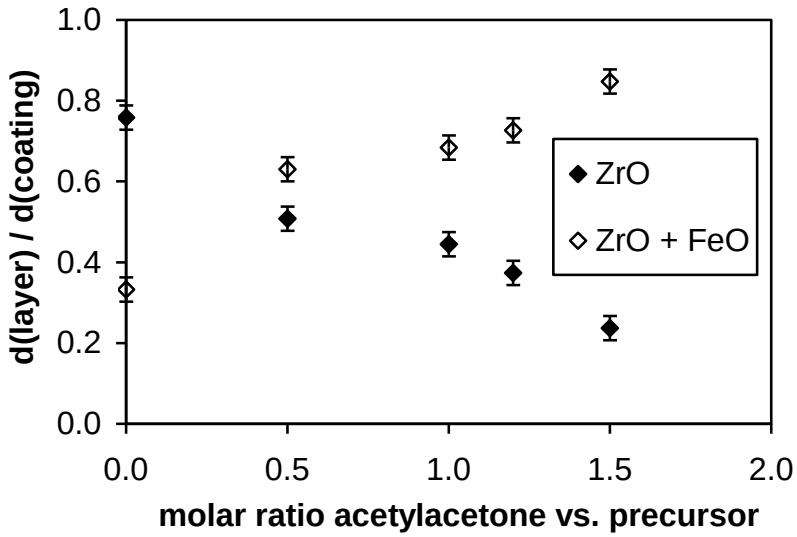

Fig. 87 Thickness ratios of d(ZrO) / d(coating) and d(mixed oxide) / d(coating) depending on the acetyl acetone content [24]

In fig. 87 the part of each layer of the overall coating thickness is displayed for better visualization. The thickness ratios were calculated from the ratios of sputter times. It can be clearly seen that the part of the mixed oxide layer increases with higher stabilizer concentration in the same way as the part of pure zirconium oxide decreases. It is known that stabilizing agents can act as chelating or bridging ligands and therefore their concentration determines the number of substituents and reactive sites at the precursor molecule. Higher concentrations promote monomeric precursors with a higher number of substituents [33,103]. Obviously these stabilized precursor molecules lead to film structures that offer a high mobility of zirconium, iron and oxygen during the heating step and therefore the final coating contains an expanded layer of both iron and zirconium oxide. If this mixed layer also contributes a low porosity then one should expect the lowest current densities at higher acac-concentrations. Unfortunately the decreasing film thickness that is found at higher acac-amounts has a contrary effect on the porosity. Since thinner films usually provide less protection than thicker films in the case of acac there should be an optimum concentration at which both effects are in balance, leading to a

minimum porosity. This behavior was exactly observed in the potentiodynamic scans. Porosity decreased with increasing acac-concentration until a minimum value at an acac/precursor ratio of 1:1. Further addition of stabilizer resulted in higher porosities again.

5.2 Zirconium oxide coatings prepared with HPC

Samples prepared with HPC have shown a lower porosity than acac-films according to the potentials scans. Therefore a significant difference in the film structure and element composition compared to acac can be expected. For this reason samples with different amounts of HPC were also investigated with secondary ion mass spectrometry.

5.2.1 Effect of HPC concentration

Changes of the film structure in dependence on the HPC concentration with a molecule mass of 80,000 g/mol were analyzed.

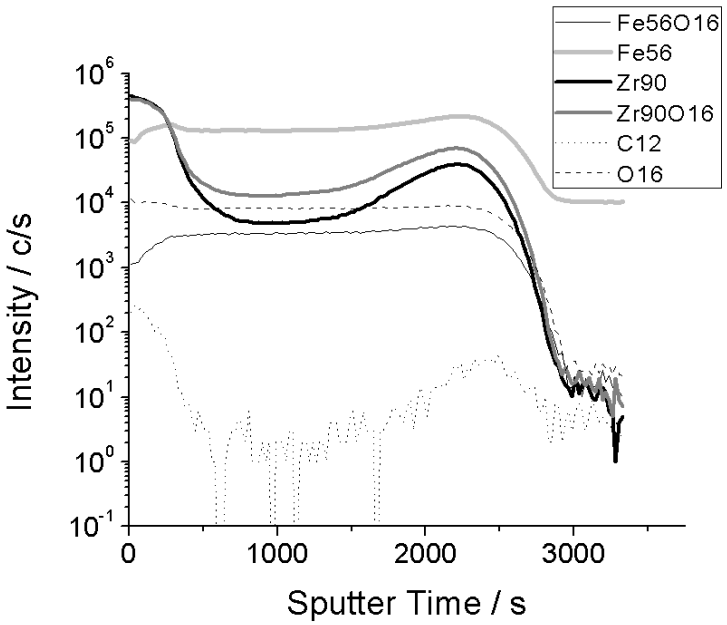

Fig. 88 SIMS depth profile of ZrO_2 coating prepared with HPC = 0.002 g/l and heated at 673 K

In fig. 88 the element distribution is shown for a coated iron sample prepared with zirconium propoxide and 0.002 g/l of a HPC (80,000 g/mol) because this molecule size showed the best protective properties. The graph looks similar to the acac depth profile, with increased iron/zirconium intensities in the interface region between coating and substrate which are probably a result of increased diffusion during the heating step. Carbon is also observed and can be attributed to remaining polymer fragments of HPC which are still present in small portions inside the coating.

An iron sample coated with zirconium propoxide (0.1M) and HPC = 0.004 g/l, heated at 673 K is shown in fig. 89.

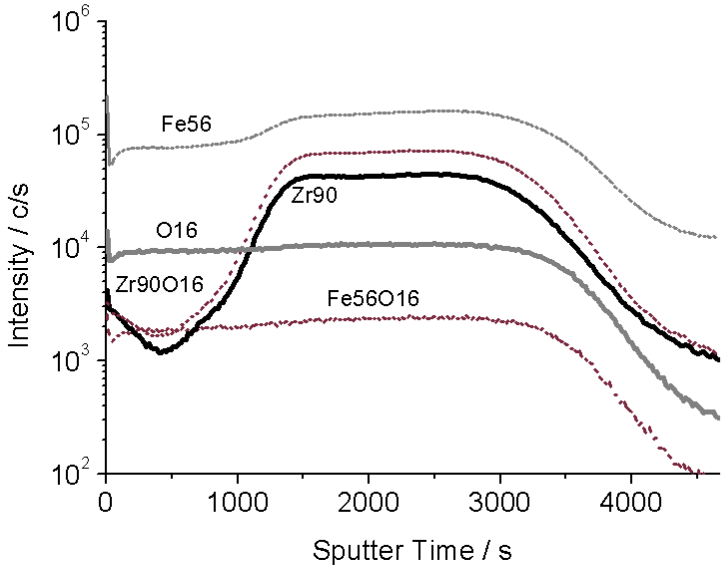

Fig. 89 SIMS depth profile of iron sample coated with ZrO_2 (0.1M)-HPC (0.004 g/l) and heated at 673K

The intensities of zirconium (Zr90) and zirconium oxide (Zr90O16) are very low in the upper coating region until 2000 s of sputter time. Instead the mixed oxide layer seems to extend over a much wider range far beyond the interface zone. High intensities for both zirconium and iron are now found between 1200 and 3800 s before the iron substrate is reached around 4000 s.

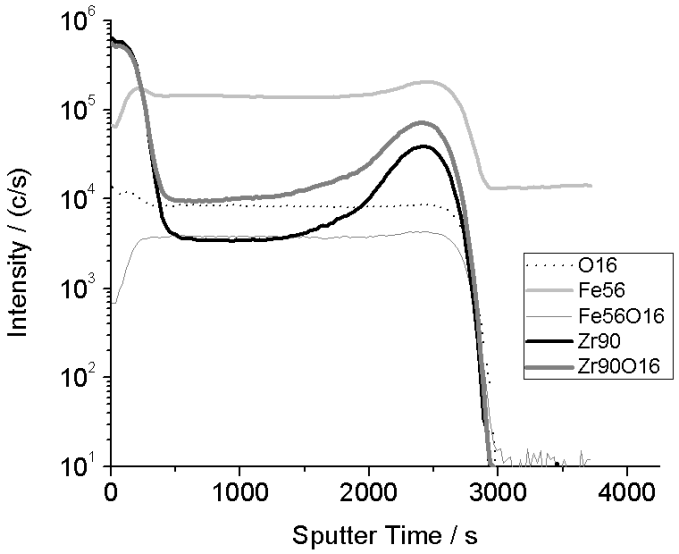

Fig. 90 SIMS depth profile for iron sample coated with zirconium propoxide-HPC = 0.006 g/l and heated at 673 K

The sample coated with 0.006 g/l HPC (fig. 90) looks very similar to the 0.002 g/l sample (fig. 88). There is a small layer of more or less pure zirconium oxide at the top of the coating then the Zr-intensity drops and rises again in the region close to the phase boundary between substrate and coating. Although the mixed oxide layer appears directly after the thin layer of zirconium oxide, higher concentrations of zirconium and iron are only found in the interface region, similar to the 0.002 g/l sample.

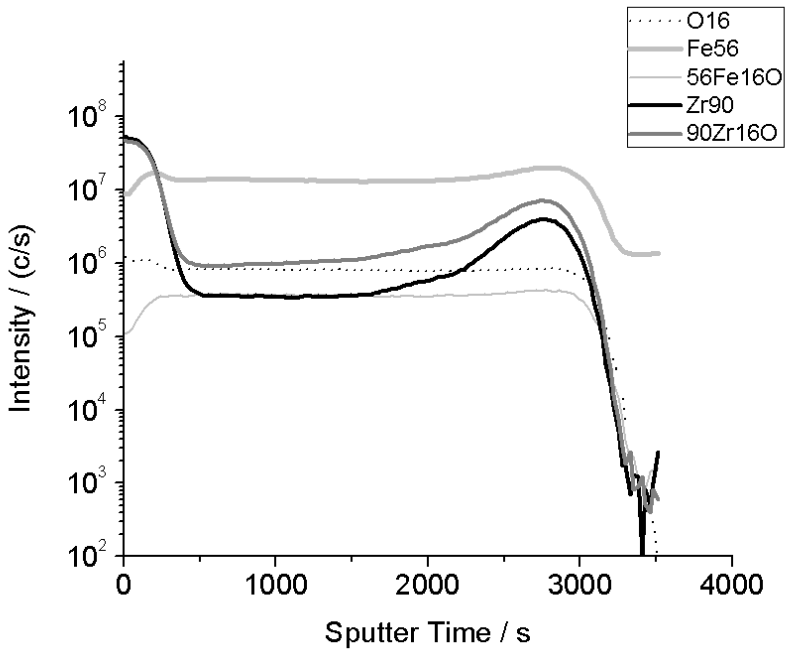

Fig. 91 SIMS depth profile for iron sample coated with ZrO_2-basis-HPC = 0.008 g/l and heated at 673K

The 0.008 g/l sample looks alsmot identical in fig. 91. Again there is a small layer of zirconium oxide, followed by a mixed phase with lower zirconium concentration at the beginning of the mixed layer and high concentrations of iron and zirconium in the interface region.

It appears that the correlation between HPC-concentration and extension of the mixed oxide layer is not as linear as in the case of acac. Also a significant dependence of film thickness on the stabilizer amount cannot be found for HPC. Instead the structure changes at a specific HPC/precursor ratio. At this ratio the steric control of the HPC component seems to direct the degree and shape of network formation in a way that promotes the growth of an expanded mixed oxide layer. The corresponding potential scans showed that the lowest film porosity is achieved at exactly the same HPC-concentration of 0.004 g/l that yields the extended mixed oxide layer. Since a similar observation was already found for acac-coated samples this is a strong indication that the formation of a mixed oxide phase is also responsible for the low-porous nature of the coating.

5.2.2 Effect of heating temperature

Iron samples were prepared at three temperatures 573, 673 and 773 K in order to investigate the effect of temperature on film structure. Fig. 92 shows a depth profile of iron sample coated with ZrO_2-basis-HPC heated at 573 K in a furnace for one hour. The film profile indicates a coating formed by a surface of zirconium oxide which thickness reaches 1000 s follows by the mixed oxide layer (zirconium, oxygen and iron) with a thickness of 1500 s and finally the iron substrate.

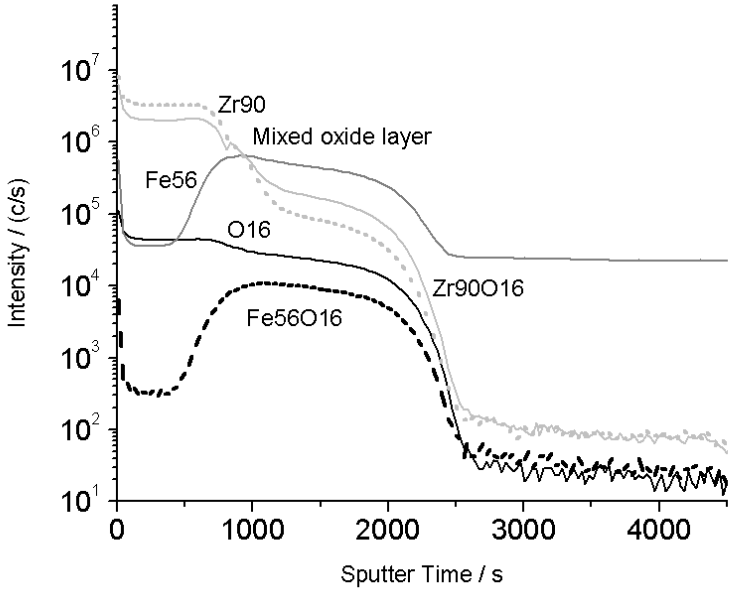

Fig. 92 SIMS depth profile for coated sample with ZrO_2-basis – HPC 0.004 g/l and heated at 573 K

As can be observed this is the typical structure for zirconium oxide coatings on iron revealed also for samples treated with acetyl acetone. At 573 K the coating structure appears to be amorphous according to the X-ray results.

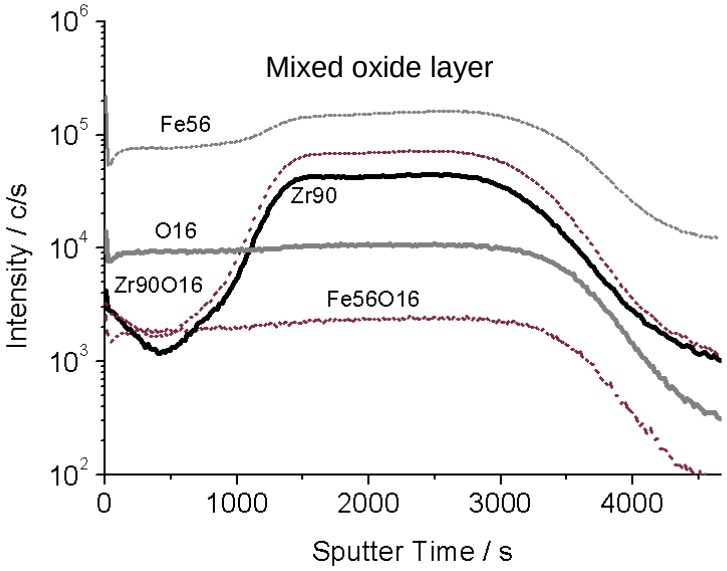

Fig. 93 SIMS profile for iron sample coated with ZrO_2-HPC = 0.004 g/l treated at 673 K

Fig. 93 displays a depth profile for coated iron treated at 673 K. The structure shows a thicker mixed oxide layer (3500 s) about twice than for the sample heated at 573 K.

However, the intensities of Zr90 and Zr90O16 arise until 1500 s remaining constant until the substrate appears. This behavior has been not observed for the sample treated at 573 K. An increase of the temperature, result in a thicker mixed oxide layer with significant reduction of the porosity. High diffusion of zirconium into deeper layer and iron oxide towards coating surface is observed.

The steric effect of HPC could also influence part of this structure in connection with the temperature increases. During this process the oxygen-metal-oxygen bridges distance will be reduced, allowing easily particles diffusion which remain adhered on the substrate surface.

To verify the correlation between thickness of the mixed oxide layer and temperature effect, a temperature of 773 K was tested and the coating depth profile is shown in fig. 94.

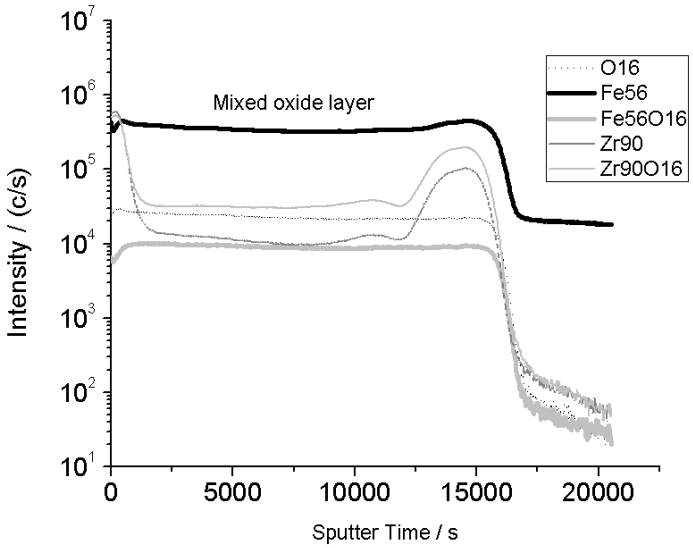

Fig. 94 SIMS depth profile of iron sample coated with ZrO_2-basis-HPC = 0.004 g/l heated at 773 K

As can be clearly seen in the graph the effect of diffusion is much more dominant at the higher temperature of 773 K. Not only the mixed layer thickness has increased, but also the overall film thickness has growth by factor 3. However, this increase of film thickness has not significantly contributed to the reduction of porosity compared to the 673 K samples.

5.2.3 Effect of HPC molar weight

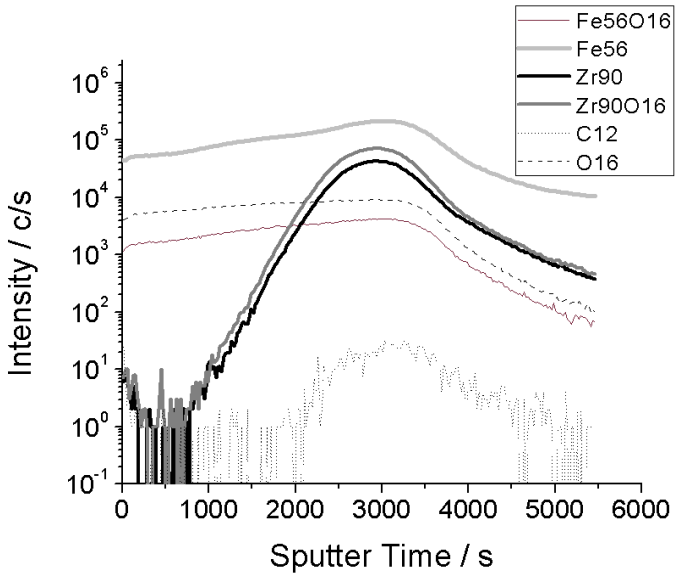

Fig. 95 Depth profile of ZrO_2 coating prepared with HPC=0.004 g/l (100MW) and heated at 673 K

Coatings prepared at this concentration but with a higher HPC molar weight show a similarity in the structure: the ZrO_2 intensity increases from the coating surface toward the mixed oxide layer with a major deposit localized direct onto substrate surface as shown in fig.95. A higher molar weight than 80,000 g/mol does not enhance the protection ability of the film much more than HPC with lower MW, however, the film structure showed in this graph reveals few changes on the thickness and element distribution of the mixed oxide layer. This result is an effect of the length of the polymeric molecules because of lower steric stabilization and flocculation of particles during the polycondensation phase [4,33,34,104].

Fig.96 shows a depth profile for coatings prepared with a HPC molecule of higher molar weight (370,000 g/mol).

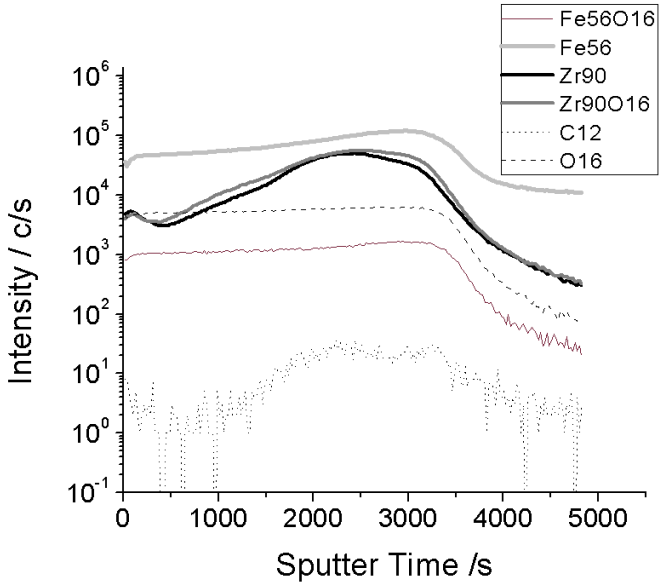

Fig. 96 Depth profile of a ZrO_2 coating prepared with HPC = 0.004 g/l (370MW) and heated at 673 K

The graph shows the same behavior of the other molar weight molecules prepared at the same HPC concentration and heated at the same temperature. However, in this case a major presence of ZrO_2 can be observed on the coating surface. That probably is the result of the bigger HPC molecule that does not contribute in high manner to the diffusion of Zr into inner layers. It was observed in electrochemical porosity investigation that higher molar weights of HPC have a contrary effect and do actually increase the film porosity. It is known that big polymeric molecules are not desirable for steric stabilization because they can promote particle flocculation instead of dispersion [34].

6. Crystalline analysis with TEM

It was found in the XRD analysis of HPC coatings that the crystalline structure changed at a certain concentration of the stabilizing agent. At 673 K and above all samples showed a crystalline phase of zirconium oxide except for a HPC concentration of 0.004 g/l. Since HPC is known to promote the formation of nanocrystalline particles which can be too small to be detected by XRD this might be a reasonable explanation for the exceptional structure in this case. Finally the verification of the coatings crystalline structure was done with TEM

measurements. Due to the complexity of sample preparation and availability of TEM equipment only the most relevant samples have been analyzed. HPC samples were prepared with a concentration of 0.004 g/l (molar weight of 80.000 g/mol) and heated at 673 K for one hour. Another sample was prepared with acetylacetone as stabilizing agent under the same conditions with a precursor/acac ratio of 1:1.

6.1 TEM measurements of ZrO_2-acac

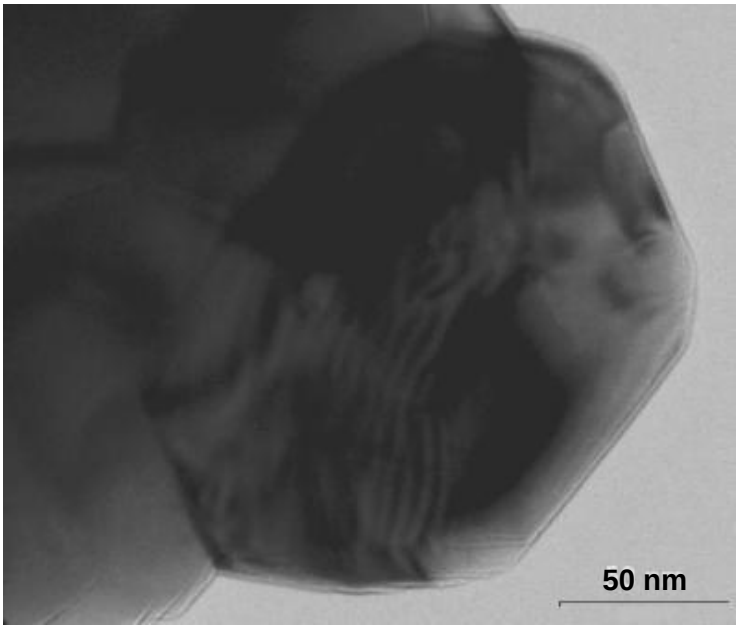

Fig. 97 High resolution TEM image of iron oxide crystal of ZrO_2-basis-acac coating heated at 673 K [44]

Fig. 97 shows a crystalline iron oxide particle with a size of 170 nm approximately. This high resolution image was obtained by TEM measurements of small pieces of the film. This part of the coating is related to the mixed oxide layer revealed in the SIMS depth profile for zirconium oxide coatings prepared with acetyl acetone as stabilizing or chelating agent. The presence of these iron oxide particles also proves the strong diffusion effects that appear during the heating procedure.

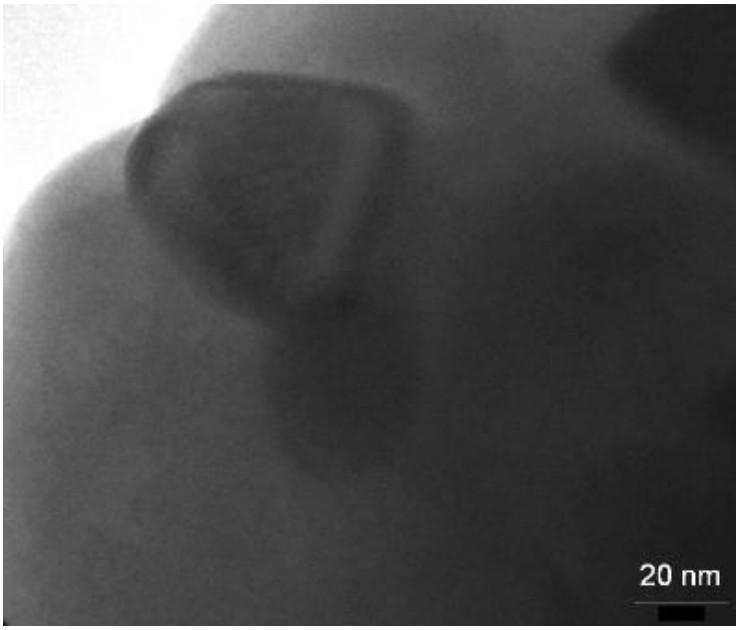

Fig. 98 Crystalline ZrO_2 particle received from TEM measurement of a ZrO_2-acac coated sample heated at 673 K [44]

In the fig.98 a crystalline zirconium oxide particle is shown. The size of the particle is around 70 nm. According to EDX scans made in this region the K-α signal of the elements zirconium and oxygen were detected. That proves the results of the X-ray diffraction, where monoclinic and tetragonal ZrO_2 phases have been reflected. From the shape and orientation of this crystal it could be identified as monoclinic ZrO_2. This high resolution TEM image is also a part of the mixed oxide layer which is formed after heating the coating at 673 K.

6.2 TEM analysis of ZrO_2-HPC

Fig.99 shows the electron diffraction map of a zirconium oxide coating prepared with 0.004 g/l HPC and heated at 673 K for one hour.

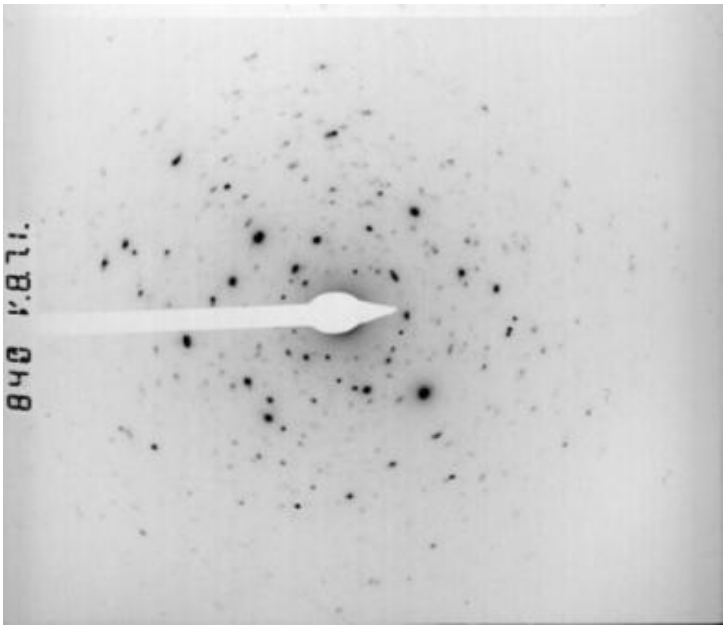

Fig. 99 Electron pattern of mixed oxide layer in a ZrO_2/HPC coated sample (0.004 g/l)

The image of the mixed oxide layer reveals the existence of dispersed crystallites immersed in an amorphous region that consists of zirconium, iron and oxygen, as revealed by EDX analysis. The small black points are related to the different reflexes received from the electrons localized in determined crystalline particles.

The size of the black points could be an indication of the distribution and size of the crystals in the mixed oxide layer. For better understanding detailed high resolution images of this region have been taken.

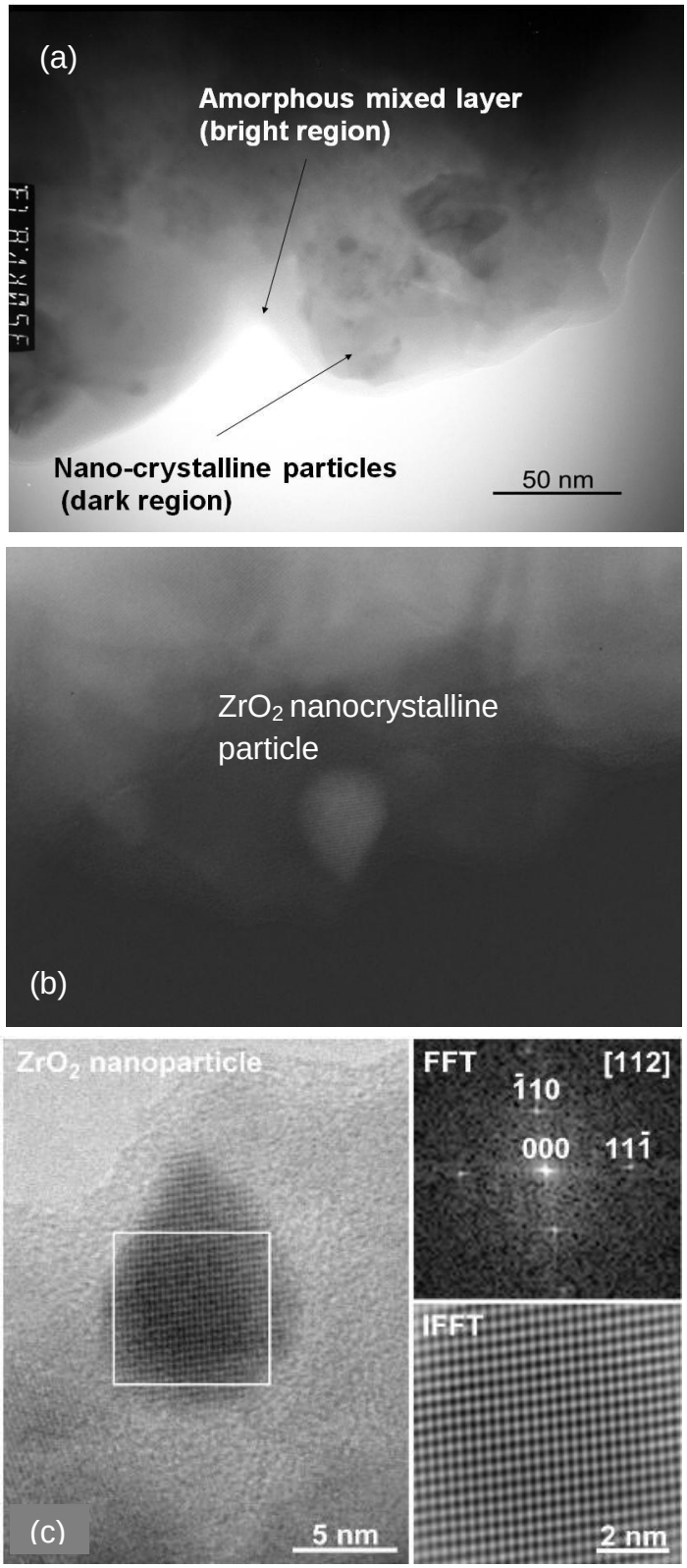

Fig.100 High resolution TEM image of a) amorphous phase of mixed oxide layer b) dispersed ZrO_2 nanocrystal c) enlarged section of the amorphous mixed layer of ZrO_2-FeO_x with finely immersed nanocrystalline ZrO_2 particles [44]. In the

upper right: Fourier-filtered image of the selected region; lower right: diffraction pattern of monoclinic ZrO_2 particle with [112] orientation.

In fig.100 high resolution TEM images of ZrO_2/HPC coatings are shown. Picture a) is an image of the mixed oxide layer. It can be seen that two regions can be distinguished inside the mixed layer as indicated with arrows. One part is formed by an amorphous layer on the boundaries. EDX made on this region revealed the presence of iron, zirconium and oxygen. However, other regions can be found with agglomerations of nanocrystalline zirconium oxide particles as shown in the figure. Therefore the mixed oxide layer of coatings prepared with 0.004 g/l HPC can be considered as an amorphous region with immersed nanocrystalline ZrO_2 particles. According to the SIMS results this interlayer shows an increased zirconium oxide concentration in the near substrate surface region. This is most likely due to the steric effect of HPC which promotes the formation of a network structure that allows a high mobility of zirconium and iron ions, as well [44].

According to the steric stabilization of HPC the bonding distance between the zirconium atoms and the adjacent oxygen atoms is reduced resulting in the formation of nanocrystalline particles [34,105,106].

Image b) is a magnification of a nanocrystalline zirconium oxide particle immersed in the amorphous layer. In picture c) of fig.83 the results of crystal structure analysis can be seen. On the upper right-hand side the crystal orientation is shown as a Fourier-filtered image and in the lower right corner as an electron pattern. The analysis of this pattern with Gatan DigitalMicrograph software and verification with the PIES program allowed the identification of the particle's crystal structure as monoclinic ZrO_2 with a [112] orientation [44]. The size of this crystal is approximately 10 nm. Further XRD results for other HPC concentrations showed reflexes of cubic phase as well.

IV. Corrosion characterization

Potential scans already proved that it is possible to reduce the film porosity of zirconium oxide coatings significantly with the right choice of stabilizing agents. Therefore additional electrochemical corrosion tests were done with acac- and HPC-stabilized coatings to investigate their actual corrosion resistance in different aqueous media. Samples with both stabilizers were prepared under the optimum conditions for the formation of low-porous films as they were found during the potential scan experiments. Acetylacetone samples were prepared with a stabilizer/precursor ratio of 1:1 and heated at 673 K. HPC-samples were deposited from a sol containing 0.004 g HPC per liter ethanol. The overall corrosion performance was investigated with linear scans and electrochemical impedance spectroscopy in a mild acetate-buffer as it was used for porosity evaluation and in a 0.05 M sodium chloride solution, as well. The results are discussed in the following chapter.

1. Linear polarization

1.1 Zirconium oxide coatings with acac

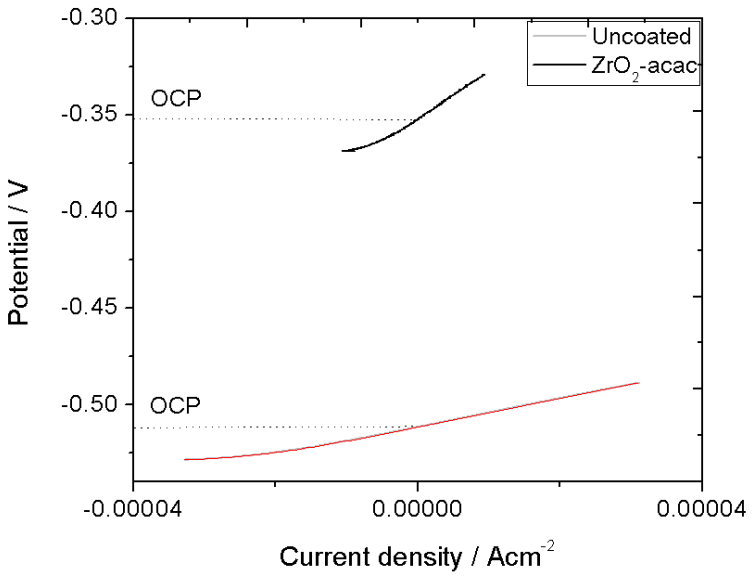

Fig.101 Linear polarization curves of uncoated iron and ZrO_2-acac sample measured in NaCl = 0.05 M

A linear polarization resistance curve of zirconium oxide–acac coating is shown in fig.101. In comparison to the uncoated sample, an anodic shift of the curve reflects the tendency of good corrosion protection. The slope of the curve allows the calculation of the polarization resistance (Rp) and with the values of corrosion current (I_{corr}) and corrosion potential (E_{corr}), the corrosion rate (k) can be calculated from equation (29). Higher inclinations mean increased corrosion resistance [79,107]. According to the software analysis the values of Rp and k for uncoated iron were: Rp = 699.7 Ohm and k = 0.11 millimeter per year (mmpy). In the case of ZrO_2-acac coated samples the resistance was increased to: Rp = 2265.6 Ohm and the corrosion rate was reduced down to k = 0.035 mmpy. This means an improvement of polarization resistance and corrosion rate by factor 3. This result matches the observations of the porosity evaluation.

1.2 Zirconium oxide coatings with HPC

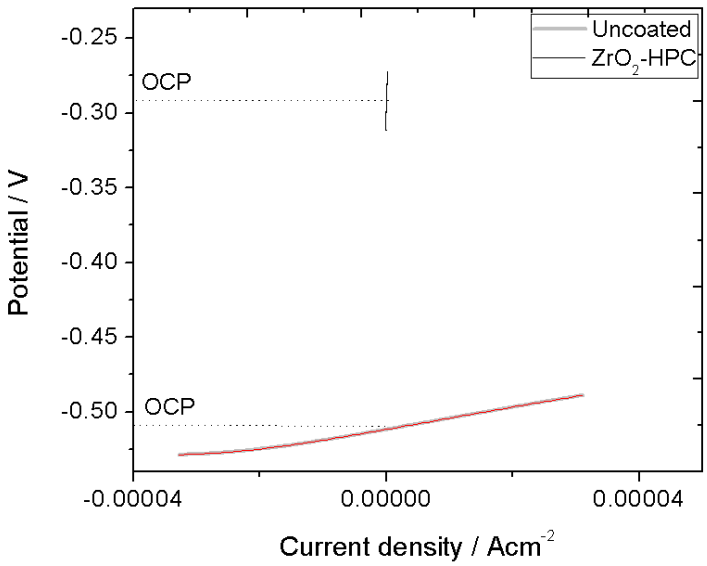

Fig.102 Linear polarization of uncoated and ZrO_2-HPC coating measured in NaCl = 0.05 M

This graph displays a linear polarization comparison of uncoated iron and a coated sample prepared with HPC after heating at 673 K. In comparison with the uncoated iron the ZrO_2-HPC samples shows an almost vertical inclination and a strong OCP-shift towards anodic direction, which both indicate a very

good corrosion resistance. The polarization resistances and corrosion rates calculated from the graphs are: uncoated iron: Rp = 699.7 Ohm and *k* = 0.10 mmpy; ZrO_2-HPC: Rp = 140712.4 Ohm and *k* = 0.00052 mmpy. It can be seen that the polarization resistance of the coated sample was even further increased when HPC was chosen as stabilizing agent. The corrosion rate was reduced by three orders of magnitude and the polarization resistance raised almost 4 orders of magnitude. The strong improvement of corrosion resistance can be again correlated with the very low average porosity of HPC films.

2. Electrochemical impedance spectroscopy

In analogy to the porosity study, impedance measurements were made in the same buffer solution of sodium acetate/ acetic acid and additional samples have been submerged in 0.1 M and 0.05 M NaCl solution.

2.1 Coatings in buffer sodium acetate/acetic acid

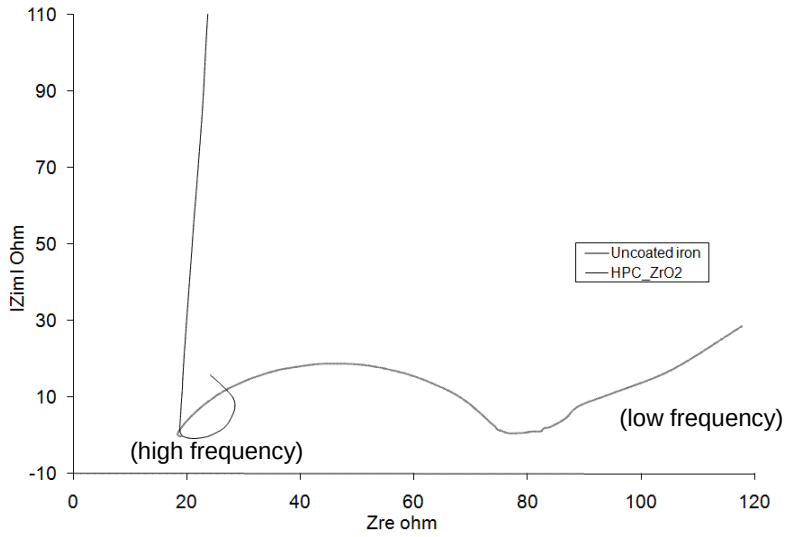

Fig. 103 Nyquist diagram of uncoated iron and ZrO_2-HPC coating measured in buffer solution of sodium acetate/acetic acid (0.1/0.01)

In fig.103 a typical semi circle in the complex plane plot (Nyquist plot) for uncoated iron is observed from 20 to approximately 80 Ohm. According to

literature this shape corresponds to a capacitive reactance [79]. This means that the polarity alternates so rapidly that the EDL does not change its composition and that not impede corrosion of the metal surface and the uncompensated solution resistance is the only component that contributes to the resistance. However, towards low frequency range, the semi circle tends to open in a straight line with a slope of 45°. This portion of line can be related to Warburg diffusion that takes place at low frequency. Thereby, a diffusion of active species occurs between the flat working electrode and the electrolyte. The polarization is due to the combination of kinetic and diffusion processes. The actual polarization resistance can be calculated from the difference between the low frequency and the high frequency end of the semi-circle. Other physical explanation for the 45° line can be attached to modifications of the sample surface which probably was covered with a thin passive layer product of iron oxide compounds.

The curve related to the ZrO_2-HPC coating shows negative impedance values at high frequencies. This is a result of the charge resistance of the EDL caused by the effect of an induction generated by the applied AC voltage. Adsorption or desorption reactions of surface active species on the metal surface can also produce induction. The induction can appear both at low or high frequencies [46]. As can be seen the resistance to charge is reflected in a steep line which indicates a high impedance magnitude. The upper end of the Y-axis is not shown to avoid compression of the uncoated-iron-plot. The high impedance of the HPC-sample can be much better visualized in the Bode plot of fig. 106.

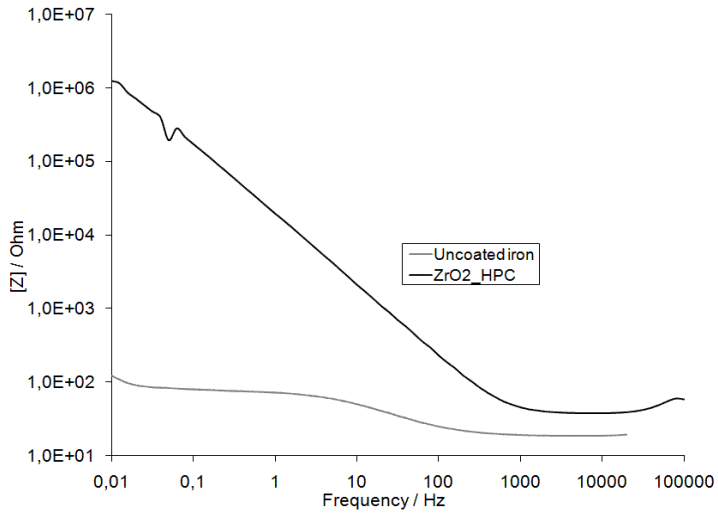

Fig. 104 Bode Plot of the samples described in fig.103

Both axes are plotted in common logarithm. At high frequency range only the uncompensated electrolyte contributes to the resistance. However, as soon as the frequency decreases the overall corrosion resistance increases too, because more elements offer additional resistance to the applied voltage such as the corrosion resistance (R_{corr}) and coating resistance (R_{coat}). The orientation of the uncoated iron line at low frequency is related to the Warburg diffusion shown in Nyquist diagram. Likewise the invariability of coated sample curve indicates very few reactions or no oxidation changes on the coating surface. The small peak at 0.1 Hz can be related to noise interference with the equipment. The corrosion resistance was increased by a high magnitude in comparison with the uncoated iron and can be obtained by the intersection of the curve with the Y-axis at low frequency (approximately $1x10^6$ Ohm/cm^{-2}). This result is in agreement with the corresponding potential scans of HPC-samples.

2.2 Coatings in NaCl = 0.05 M

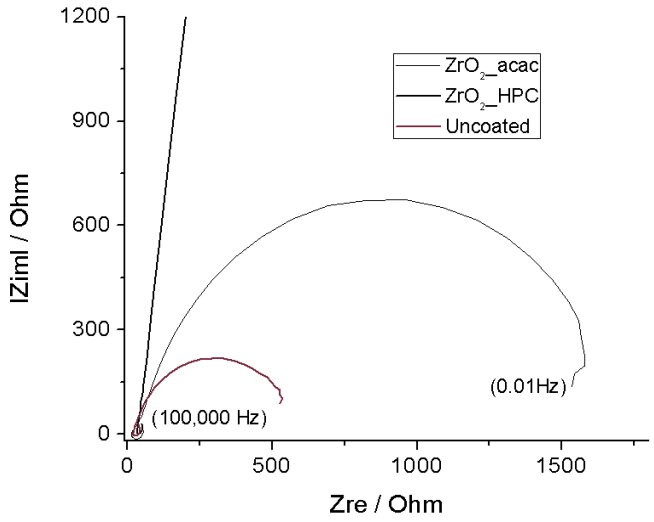

Fig. 105 Nyquist diagram of ZrO_2-acac, ZrO_2-HPC and uncoated iron measured in NaCl = 0.05 M

Further impedance measurements were done in a more aggressive 0.05 M NaCl solution which are shown in fig.105 and 106. The Nyquist diagram displays a typical semi circle for uncoated iron, which indicates that corrosion on the sample surface is present and only the uncompensated electrolyte resistance acts as corrosion resistance. In the case of the acetyl acetone-ZrO_2 coating an increase of the corrosion resistance can be observed by the increasing radius of the large semi circle. In the real impedance magnitude the polarization resistance of the acac-ZrO_2 coating is around 1600 Ohm/cm^{-2}. In the case of ZrO_2-HPC coating a large straight line with almost vertical slopes found that indicates very high impedance. The value of the polarization resistance is around $1x10^6$ Ohm, approximately. Obviously the low porosity observed in the potential scans is responsible for the better protection performance of the HPC-coatings.

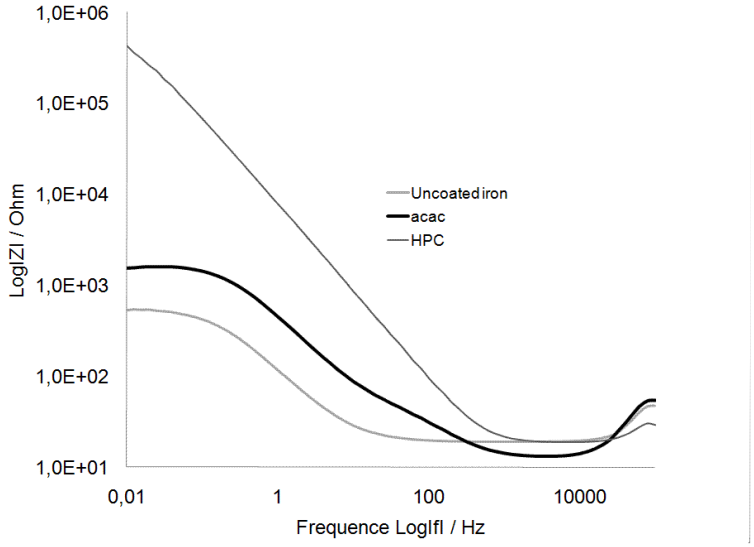

Fig. 106 Corresponding Bode plot magnitude graphic of samples described in fig. 105

The corresponding Bode plot is shown in fig.106. The curves of uncoated iron and ZrO_2-acac remain constant at the low-frequency end which indicates that not structural changes occurr on the sample surface. However, above 1 Hz the curves show a constant slope due to changes on the surface like film delamination or corrosion processes at the exposed area. In the case of ZrO_2-HPC the curve appears as a straight line with negative slope. The increase of the corrosion resistance from higher frequencies towards lower frequencies indicates a relatively stable film structure. The corrosion resistance is in the range close to $1x10^6$ Ohm/cm^2 which is very high compared to the acac sample and even more compared to uncoated iron. A low frequency is blocked by the corrosion and coating resistance. In the middle frequencies range EDL and electrolyte offers also resistance, that way the corrosion resistance at low frequency is the sum of all resistances [46,49]. At high frequency range the coating and corrosion resistance and EDL as well look like they do not exist, reflecting very low resistance because the impedance is dominated by the capacitive element of the uncompensated electrolyte [46]. The linear scan experiments and the electrochemical impedance tests both support the results from electrochemical porosity evaluation. Zirconium oxide coatings prepared with acetylacetone already show good corrosion protection but it can be even

further improved when the precursor solution is stabilized with HPC. Corrosion tests and porosity evaluation show a very high corrosion resistance which is due to very low average film porosity.

Summary

Thin zirconium oxide coatings have been successfully deposited on iron substrates via sol-gel route at low temperature. Electrochemical investigations of these films have shown a significant reduction of the Fe substrate dissolution current density, indicating a good protection ability of the coating material. It was found that the film porosity which is a crucial parameter for good corrosion protection can be successfully reduced by the use of the stabilzing agents acetyl acetone and HPC. In the case of acetyl acetone the dissolution current densities could be reduced by 3 orders of magnitude compared to the uncoated metal substrate. With the use of HPC a redution by 5 orders of magnitude could be achieved. Additional corrosion test with linear scans and electrochemical impedance spectrometry verified the good protection ability of the stabilized zirconium oxide coatings.

Structure characterization of the deposited films revealed common parameters for both stabilizing agents that promote the formation of low-porous film structures, although the individual mechanisms are quite different for acetylacetone and HPC.

In both cases there exists an optimum ratio between the amount of stabilizing agent and alkoxide precursor that leads to the formation of a film structure with a minimum porosity. For acac-stabilzed coatings there are two contrary effects that determine the optimum ratio. With increasing acac-concentration on the one hand the film porosity is lowered while on the other hand the overall film thickness is also reduced which weakens the benefit of reduced porosity. This dependence of film thickness on stabilizer concentration was not found for HPC.

It could be shown that at certain stabilizer/precursor ratios a mixed phase of zirconium oxide and iron oxide is formed in the coating which is responsible for the reduction of film porosity. The formation of this phase can be attributed to the presence of the stabilizing agents which control the reactive sites.

A crystalline structure was achieved in ZrO_2-acac coatings, but ZrO_2-HPC films showed at the optimum concentration an amorphous mixed oxide layer containing nanocrystalline ZrO_2 particles. The correlation between growth of the mixed oxide phase and decrease of dissolution current density suggests that it

is the mixed oxide phase with ZrO_2 nanoparticles, initiated by the stabilizers, that is responsible for the reduction of film porosity and the good protection properties of the films.

It is well known that corrosion may occur along pores and cracks and also along grain boundaries. A chemically stable low-porous amorphous coating, as obtained unter the described circumstances, therefore offers a very effective protection to the substrate.

References

1. J.J. Ebelmen, Ann, 57 (1846) 331.
2. M.A. Aegerter and M. Mennig, Sol-gel technologies for glass producers and users, Kluwer Academic Publishers, (2004), Massachussetts, USA.
3. E.M. Rabinovich, in Sol-Gel Technology for Thin Films, Fibers, Performs, Electronics and Speciality Shapes, L.C Klein, (1988), New Jersey, USA.
4. C.J. Brinker, G.W. Scherer, Sol-gel science: The physic and chemistry of sol-gel processing, Academy Press, (1990), San Diego, USA.
5. V.G. Kessler, G.I. Spijksma, G.A. Seisenbaeva, S. Håkansson, D.H.A. Blank, H.J.M. Bouwmeester, J. Sol-Gel Sci. Technol. 40 (2006) 163-179.
6. J. Livage, M. Henry and C. Sanchez, Sol-Gel Chemistry of Transition Metal Oxides, Prog. Solid St. Chem., 18 [4] (1988), 259-342.
7. M. Chatry, M. Henry, M. In, C. Sanchez and J. Livage, The Role of Complexing Ligands in the Formation of Non-Aggregated Nanoparticles in Zirconia, J. Sol-Gel Scie. Technol., 1 (1994) 233-240.
8. R. Kreiter, M.D.A. Rietkerk, B.C. Bonekamp, H. M. van Veen, V.G. Kessler, J. F. Vente, Sol–gel routes for microporeuse zirconium and titania membranes, J. Sol-Gel Sci. Technol., 48, (2008), 203-211.
9. V. Baran, Hydroxyl ion as a ligand, Coordin. Chem. Rev., 6, (1971), 65-93.
10. H. Choi, S. H. Wang, Sol-gel-derived magnesium oxide precursor for thin-film fabrication, Mater. Res. Soc. 15, (2000), 842-845.
11. N. Özer, Electrochemical properties of sol-gel deposited vanadium pentoxide films, Thin Solid Films, 305, (1997), 80-87.
12. M. Yang, C. Zhou and D. Jiang, Comparison of different strategies to realize highly reflective thin film coatings at 1064 nm, Infra. Phys. Technol., 51, (2008), 572-575.

13. V. G. Kessler, G. A. Seisenbaeva, M. Unell and S. Håkansonn, Chemically Triggered Biodelivery Using Metal-Organic Sol-Gel Synthesis, Angew. Chem. Int. Ed., 47, (2008), 8506-8509.

14. E. Eisenbarth, D. Velten, M. Müller, R. Thull and J. Breme, Nanostructured niobium oxide coatings influence osteoblast adhesion, J. Biomed. Mater. Res. Part A, 79, (2006), 166-175.

15. R. Romero Pareja, R. López Ibáñez, F. Martín, J.R. Ramos-Barrado, D. Leinen, Corrosion behaviour of zirconia barrier coatings on galvanized steel, Surf. Coat. Technol, 200, (2006), 6606-6610.

16. H. Li, K. Liang, L. Mei, S. Gu, S. Wang, Oxidation protection of mild steel by zirconia sol–gel coatings, Mater. Lett., 51, (2001), 320-324.

17. A. Nazeri, S.B Qadri, Alumina-stabilized zirconia coatings for high-temperature protection of turbine blades, Surf. Coat. Technol., 86, (1996), 166-169.

18. F. Sittner, W. Ensinger, Ion permeability of amorphous hydrogen- and fluorine-containing carbon films formed by plasma enhanced chemical vapour deposition, Nuclear Instruments and Methods in Physics Research Section B, 257, (2007), 737-740.

19. K. Bobzin, E. Lugscheider, M. Maes and P. Immich, Developing PVD zirconium-oxide coatings for use of thixoforming of steel, Internat. J. of Microstruct. and Mater. Proper., 3, (2008), 262 – 270.

20. A. Amadeh, B. Pahlevani and S. Heshmati-Manesh, Effects of rare earth metal addition on surface morphology and corrosion resistance of hot-dipped zinc coatings, Corr. Sci., 44, (2002), 2321- 2331.

21. S.G. Shyu, T.J. Smith, S. Baskaran and R.C. Buchanan in Better Ceramics Through Chemistry III, eds. C.J. Brinker, D.E, Clark and D.R. Ulrich, Mat. Res. Soc., (1988), 767.

22. P. T. Nguyen, Korrosionsschutz von Eisenwerkstoffen durch intrinsisch leitfähige Polymere, Doctoral Thesis, Techn. Uni. Dresden, 2003, Germany.

23. F. Sittner, W. Ensinger, Electrochemical investigation and characterization of thin - film porosity, Thin Solid Films, 515, (2007), 4559-4564.

24. R. Ugas-Carrión, F. Sittner, C.J. Ochs, S. Flege, W. Ensinger, Characterization of the porosity of thin zirconium oxide coatings prepared at low temperatures, Thin Solid Films, 517 [6], (2009), 1967-1969.

25. M. L. Zheludkevich, I. Miranda Salvado and M.G.S. Ferreira, Sol-Gel Coatings for Corrosion Protection, J. Mater. Chem., 15, (2005), 5099-5111.

26. P. B. Kirk, M.J. Filiaggi, R.N.S. Sodhi, R. M. Pilliar, Evaluating sol-gel ceramic thin films for metal implant applications: III. In vitro aging of sol-gel-derived zirconia films on Ti-6Al-4V, J. Biomed. Mater. Res. (Appl Biomater), 48, (1999), 424-433.

27. C. J. Ochs, F. Sittner, R. Ugas-Carrión, M. Yekehtaz, S. Flege, W. Ensinger, Structural and electrochemical characterization of zirconium and silicon based sol-gel coatings for corrosion protection, Current Topics in Electrochemistry, 13, (2008), 59-65.

28. M. Yekehtaz, K. Baba, R. Hatada, S. Flege, F. Sittner, W. Ensinger, Corrosion Resistance of Magnesium Treated by Hydrocarbon Plasma Immersion Ion Implantation, Nuclear Instruments and Methods in Physics Research Section B 267, (2009), 1666-1669.

29. G. Kickelbick, Hybrid Materials. Synthesis, Characterization, and Applications. Wiley-VCH, (2007), Weinheim, Germany.

30. F.C.M. Woudenberg, Nanostructured oxide coatings via emulsion precipitation. Thesis, University of Twente, Enschede, Netherlands, 2001.

31. J. Shi, CISM, Steric stabilization, Literature Review, Ohio State University, 06502, 2002.

32. A.A. Parker, G.H. Armstrong and D.P. Hedrick, NMR and sedimentation studies ofa polymeric steric stabilizer for alumina, J. Appl. Polymer Sci., 47, (1993), 1999-003.

33. G.H. Armstrong, L. Johnson and A.A. Parker, Effect of polymeric steric stabilizers on the settling of alumina, Journal of Applied Polymer Science, 52, (1994), 997-1004.

34. D.H Napper, Polymeric Stabilization of Colloidal Dispersions, Academic Press, (1983), New York, USA.

35. G.I. Spijksma, G.A. Seisenbaeva, A. Fischer, H.J.M Bouwmeester, D.H.A. Blank and V.G. Kessler, The molecular composition of non-modified and acac-modified propoxide and butoxide precursors of zirconium and hafnium dioxides, J. Sol- Gel Sci. Technol., 51, (2009), 10-22.

36. G.I. Spijksma, H.J.M. Bouwmeester, D.H.A. Blank, V.G. Kessler, Stabilization and destabilization of zirconium propoxide precursors by acetylacetone, Chem. Commun., (2004), 1874-1875.

37. G.I. Spijksma, L. Kloo, H. J.M. Bouwmeester, D.H.A. Blank and V.G. Kessler, Nona-coordinated MO6N3 centers M=Zr,Hf as a stable building block for the construction of heterometallic alkoxide precursors, Inorg. Chim. Acta, 360, (2007), 2045-2055.

38. S. Shukla, S. Seal, Phase stabilization in nanocrystalline zirconia, Rev. Adv. Mater. Sci., 5, (2003), 117-120.

39. S. Shukla, S. Seal, R. Vij and S. Bandyopadhyay, Polymer Surfactant Incorporated Ceramic Oxide Nanoparticles, Rev. Adv. Mater. Sci. 4, (2003), 1-9.

40. E. Berstein, M. G. Blanchin, R. Ravelle-Champuis and J. Rodriguez-Carvajal, Structural studies of phase transformations in ultrafine zirconia powders, J. Mater. Sci., 27, (1992), 6519-6524.

41. A.G. Gaynor, R.J. Gonzalez, R.M. Davis, R. Zallen, Characterization of nanophase titania particles synthesized using in-situ steric stabilization, J. Mater. Res., 12, (1997), 1755-1765.

42. R.J. Hunter, Zeta Potential in Colloid Science, Academic Press, (1981), New York, USA.

43. J.C. Sanders, M.C. Breadmore, Y.C. Kwok, K.M. Horsman and J.P. Landers, Hydroxypropyl Cellulose as an Adsorptive Coating Sieving Matrix for DNA Separations, Amer. Chem. Soc., 75, (2003), 986-994.

44. R. Ugas-Carrión, F. Sittner, M. Yekehtaz, S. Flege, J. Brötz and W. Ensinger, Influence of stabilizing agents on structure and protection performance of zirconium oxide films, Surf. Coat. Technol., 204 (2010), 2064-2067.

45. P. Marcus, Corrosion Mechanisms in Theory and Practice, Marcel Dekker, Inc., (2002), New York, USA.

46. W.S. Tait, An introduction to the electrochemical corrosion testing for practicing engineers and scientists, PairODaoes Publications, (1994), Racine, Wisconsin, USA.

47. L-S. Van Delinder, Corrosion Basis an Introduction, NACE Publication, (1984), Houston, USA.

48. R. G. Kelly, J. R. Scully, D. W. Shoesmith and R. G. Buchheit, Electrochemical Techniques in Corrosion Science and Engineering, Marcel Dekker, Inc., (2003), New York, USA.

49. K-H. Tostmann, Korrosion Unsachen und Vermeidung, Wiley-VCH, (2001), Weinheim, Germany.

50. G.H. Koch, M.P.H. Brongers, N.G. Thompson, Y.P. Virmani, J.H. Payer, Corrosion Costs and Preventive Strategies in the United States, Publication No. FHWARD-01 (Washington, D.C.: FHWA, (2002) 156.

51. H. Huber, P. Crimmann, D. Bendix, K. Roth, Neuentwicklung eines Korrosionstestsystems: Hochtemperaturmikroben als Prüfingenieure, Uni Regensburg, ATZ Entwicklungzentrum, (2006) pp. 2.

52. H. A. Videla, Manual of Biocorrosion, Press by CRC Lewis, Inc., (1996), Florida, USA.

53. P. Atkins and J. De Paula, Atkins´ Physical Chemistry, Oxford University Press, 8th edition, (2006), Oxford, Great Britain.

54. A. Courtney, Ch 412 Advanced Inorganic Chemistry, Western Oregon University press, (2001), USA.

55. http://www.corrosion-doctors.org

56. S. Li, W.T. Zheng, Q. Jiang, Size and pressure effects on solid transition temperatures of ZrO_2, Scripta Materialia, 54, (2006), 2091–2094.

57. T. K. Gupta, J. H. Bechtold, R. C. Kuznicki, L. H. Cadoff and B.R. Rossing, Stabilization of tetragonal phase in polycrystalline zirconia, Journal of Material Science, 12 (1977), 2421-2426.

58. W. Córdova-Martínez, E. De la Rosa-Cruz, L. A. Díaz-Torres, P. Salas, A. Montoya, M. Avendaño, R. A. Rodríguez and O. Barbosa-García, Nanocrystalline tetragonal zirconium oxide stabilization at low temperatures by using rare earth ions: Sm^{3+} and Tb^{3+}, Optical Materials, 20 (2002), 263-271.

59. F. Namavar, G. Wang, C. Li Cheung, R. F. Sabirianov, X.C. Zeng, W.N. Mei, J. Bai, J. R. Brewer, H. Haider and K. L. Garvin, Thermal stability of nanostructurally stabilized zirconium oxide, IOP Nanotechnology, 18, (2007), 415702.

60. N. El Habra, M. Bolzan, C. De Zorzi, M. Favaro, M. Casarin, C. Sada and G. Rossetto, Stabilized Zirconia-Based Materials for Solid Oxide Fuel Cells (SOFC) obtained by MOCVD and Aerosol-CVD, Online free paper, Electrochemical.Org/meeting.

61. Y. Kuo, Mixed Oxide High-k Gate Dielectrics - Interface Layer Structure, Breakdown Mechanism, and Memories, ECS 210th Meeting, (2006), Abstract 1115.

62. K. Schenk-Meuser, D. Velten, E. Eisenbarth, V. Biehl, H. Duschner, J. Breme, XPS analysis of sol-gel-generated mixed-oxide layers for biomedical application, Surface and Interface Analysis, 34 (2002), 59-62.

63. H. Hasuyama, Y. Shima, K. Baba, G. K. Wolf, H. Martin and F. Stippich, Adhesive and corrosion-resistant zirconium oxide coatings on stainless steel prepared by ion beam assisted deposition, Nuc. Instr. and Meth. Phys. Res. Sect. B: 127-128, (1997), 827-831.

64. P. Mechnich and W. Braue, ZrO_2-Environmental Barrier Coatings for Oxide/Oxide Ceramic Matrix Composites fabricated by Electron-beam Physical Vapor Deposition, electronic library, Deusches Zentrum für Luft und Raumfahr (2009).

65. G. Tian, J. Huang, T. Wang, H. He and J. Shao, Microstructure and laser-induced damage threshold of ZrO_2 coatings dependence on annealing temperature, Appl. Surf. Sci., 239, (2005), 201-208.

66. P.B. Srinivasan, J. Liang, C. Blawert and W. Dietzel, Dry sliding wear behaviour of magnesium oxide and zirconium oxide plasma electrolytic oxidation coated magnesium alloy, Appl. Surf. Sci., 256, (2010), 3265-3273.

67. R. Shacham, D. Mandler and D. Avnir, Electrochemically Induced Sol-Gel Deposition of Zirconia Thin Films, Chem. Eur. J., 10, (2004), 1936-1943.

68. K. S. Alber and J. A. Cox, Electrochemistry in Solids Prepared by Sol-Gel Processes, Mikrochim. Acta, 127, (1997), 131-147.

69. http://www.princeton.edu/~pccm/outreach/REU2006/REU2006Presentations/gilida.pdf

70. M. Stern and A. L. Geary, J. Electrochem. Soc., 104(1), (1957), 56-63.

71. M. Stern, Corrosion, 14 (10), (1958), 61-64.

72. http://wpcontent.answers.com/wikipedia/commons/4/4c/Cyclovoltammogram.jpg

73. C. H. Hamann and W. Vielstich, Electrochemie, 3., vollständige überarbeitete Auflage, Wiley-VCH, (1998), Weinheim, Germany.

74. Z. Ahmad, Principles of Corrosion Engineering and Corrosion Control, IChem^{E}, BH, (2006), Oxford, UK.

75. Gamry Instruments, © Copyright, Electrochemical impedance spectroscopy primer, (2005).

76. E. Barsoukov and J. R. Macdonald, Impedance Spectroscopy: Theory, Experimental and Applications, 2 ed. Wiley-Interscience, (2005), New Jersey, USA.

77. Tesis Doctoral, Universidad Politécnica Cataluña, http://www.tesisenxarxa.net/TESIS_UPC/AVAILABLE/TDX-0529101-130232/07CAP5.pdf

78. U. Rammelt, G. Reinhard, Characterization of active pigments in damage of organic coatings on steel by means of electrochemical impedance spectroscopy, Prog. Org, Coat. 24, (1994), 309.

79. P. A. Schweitzer, Fundamentals of Metallic Corrosion: Atmospheric and media corrosion metals, Corrosion Engineering Handbook 2 ed., CRC Press, (2006), Florida, USA.

80. P.J. Gellings and H.J.M Bouwmeester, The CRC Handbook of Solid State Electrochemistry, CRC Press, (1997), Florida, USA.

81. L. Spieß, R. Schwarzer, H. Behnken, G. Teichert, Moderne Röntgenbeugung, B.G. Teubner Verlag, (2005), Wiesbaden, Germany.

82. J. F. Moulder, W. F. Stickle, P. E. Sobol, and K. D. Bomben, Handbook of X-ray Photoelectron Spectroscopy, Physical Electronics, Inc., (1995), Eden Prairie.

83. H. Düsterhürft, M. Riedel and B.-K. Düsterhöft, Einführung in die Sekundärionmassenspektrometrie -SIMS-, B.G Teubner, (1998), Leipzig, Germany.

84. D.A. Skoog and J.J. Leary, Instrumentelle Analytik, Grundlagen Geräte-Anwendungen, Springer, (1996), Milan, Italy.

85. Ims6f synopsis, Cameca, Gennevilliers Cedex, 2000, France.

86. J. Als-Nielsen, D. McMorrow, Elements of Modern X-Ray Physics, John Wiley & Sons Ltd, (2001), New York, USA.

87. M. Fujimoto, T. Ohno, H. Suzuki, H. Koyama and J. Tanaka, Nanostructure of TiO_2 Nano-Coated SiO_2 Particles, J. Amer. Ceram. Soc, 10.1111/j.1551-2916.2005.00583.x.

88. H. Dun,W. Zhang, Y. Wei, S. Xiuqing, Y. Li and L. Chen, Layer-by-Layer Self-Assembly of Multilayer Zirconia Nanoparticles on Silica Spheres for HPLC Packings, Anal. Chem., 76, (2004), 5016–5023.

89. J. Voelkel, Improvement in Quality of Sol-Gel Derived Zirconia Multilayer Coatings by Polymeric Additive, Molec. Cryst. and Liq. Cryst., 354, (2000), 1563-5287.

90. H. Li, K. Liang, L. Mei and S. Gu, Oxidation resistance of mild steel by zirconia sol–gel coatings, Mater. Sci. and Eng. A, 341, (2003), 87-90.

91. E. Rubio, J. Almaral, R. Ramírez-Bon, V. Castaño and V. Rodríguez, Organic–inorganic hybrid coating (poly(methyl methacrylate)/monodisperse silica), Optic. Mater., 27, (2005), 1266-1269.

92. M.E. Pires de Souza, E. Ariza, M. Ballester, I. V. Pagotto Yoshida, L.A. Rocha, C.M. de Alvarenga Freire, Characterization of organic-inorganic hybrid coatings for corrosion protection of galvanized steel and electroplated ZnFe steel, Mat. Res., 9, (2006).

93. J.M. Keijman, Inorganic Organic Hybrid Coatings in the Protective Coatings Industry, former Technical Director Ameron BV, (2003), Netherlands.

94. S. Wang, C. Liu and F. Shan, Structural investigation of the zirconium-titanium based amino trimethylene phosphonate hybrid coating on aluminum alloy, Acta Metallurgica Sinica (English Letters), 22, (2009), 161-166.

95. S. Roux, P. Audebert, J. Pagettia and M. Roche, Electropolymerization of carboxylic acid functionalized pyrrole into hybrid zirconium–silicon oxopolymer sol–gel coatings, New J. Chem., 26, (2002), 298–304.

96. Q. Liu, L. Zhang, L. Cheng and Y. Wang, Chemical vapour deposition of zirconium carbide and silicon carbide hybrid whiskers, Mater. Lett., 64, (2010), 552-554.

97. A. Collazo, A. Covelo, C. Pérez, Structural transformation of silane-based zirconium-modified sol-gel coatings, Surface and Interface Analysis, (2010), 10.1002/sia.3186.

98. L. Téllez, J. Rubio, M. A. Valenzuela, F. Rubio and J. L. Oteo, Zirconium Effect on the Synthesis and Textural Properties of Organic Inorganic Hybrid Materials, Advan. Technol. Mater. Mater. Process. J., 8, (2006), 226-231.

99. D. L. Versace, O. Soppera, J. Lalevée and C. Croutxé-Barghorn, Influence of zirconium propoxide on the radical induced photopolymerisation of hybrid sol–gel materials, New J. Chem., 32, (2008), 2270 – 2278.

100. Y. Chen, H-W. Yang, Hydroxypropyl cellulose (HPC)-stabilized dispersion polymerization of styrene in polar solvents: Effect of reaction parameters, J. Poly. Sci. Part A: Poly. Chem., 30, (2003), 2765-2772.

101. F. H. Allen, The Cambridge Structural Database: a quarter of a million crystal structures and rising, Acta Cryst., B58, (2002), 380-388.

102. M. Sedlar and M. Sayer, Reactivity of Titanium Isopropoxide, Zirconium Propoxide and Niobium Ethoxide in the System of 2-Methoxyethanol, 2,4-Pentanedione and Water, J. Sol-Gel Sci. Technol., 5, (1995), 27-40.

103. G. I. Spijksma, D. H. A. Blank, H. J. M. Bouwmeester and V. G. Kessler, Modification of Different Zirconium Propoxide Precursors by Diethanolamine. Is There a Shelf Stability Issue for Sol-Gel Applications?, Int. J. Mol. Sci., 10, (2009), 4977-4989.

104. M. Niederberger and N. Pinna, Metal Oxide Nanoparticles in Organic Solvents: Synthesis, Formation, Assembly and Application, Springer, (2009), 217 p.67 illus, London.

105. S. Mezdour, A. Lepine, P. Erazo-Majewicz, F. Ducept and C. Michon, Oil/water surface rheological properties of hydroxypropyl cellulose (HPC) alone and mixed with lecithin: Contribution to emulsion stability, Coll. Surf. A: Physicochem. Eng. Asp., 331, (2008), 76-83.

106. A. Ain-Aia and P. K. Gupta, Effect of arginine hydrochloride and hydroxypropyl cellulose as stabilizers on the physical stability of high drug loading nanosuspensions of a poorly soluble compound, Int. J. Pharma., 351, (2008), 282-288.

107. P. R. Roberge, Corrosion Basics: An Introduction, NACE International, (2006), Houston, USA.

List of chemicals and materials

Iron 30 mm diameter 99,8 %, Typical Analysis: Mn <800, C <200, P <200, S <150 (ppm), ARMCO®, Goodfellow

Ethanol absolut 99.9 %, G CHROMASOLV®, Sigma-Aldrich

Acetylacetone ReagentPlus® , >= 99 %, Sigma-Aldrich

Glacial acetic acid purum ≥ 99.0 %, Fluka Analytical

1-Propanol ≥ 99.80 %, Sigma-Aldrich

Hydroxypropyl cellulose, powder, Aldrich, 80,000; 100,000 and 370,000 g/mol

Zirconium (IV) propoxide solution, purum ~70 % in propanol, Fluka

Phenyl-triethoxysilane = 98 % (GC) Aldrich chemistry

Curriculum Vitae

RUPERTO A. UGAS CARRION
urupert@hotmail.com

Study

2006 – October 2010 **Doktor-Ingenieurs (Dr.-Ing.)**, Chemistry and Material sciences Departments, Material analytics, TU-Darmstadt, Germany

Thesis "Study of stabilizing agents in thin sol-gel zirconium oxide protective coatings on iron materials

- Diploma, Chemical Engineer, Universidad de Oriente, July, 2003, Venezuela.

Thesis "Mathematical model for the bioremediation of contaminated soils with hydrocarbons in a bioreactor of packed bed"

Academic Courses

- German Course for Technical Presentation, Philipps Universität Marburg, 2008
- English intermediate stage Oral, TU-Darmstadt, 2008
- English intermediate stage Writing, TU-Darmstadt, 2007
- English high intermediate intensive, Dolphin Institute, Dublin, 2006
- German intensive Mittelstufe 6 months, Speak & Write School, Marburg, 2006
- Gas Measurement and Technology, ABB, Venezuela, 2005
- Gas Measurement and Technology, Repsol, Venezuela, 2005
- Gas Engineering Levels I, II and III, PDVSA, Venezuela, 2004-2005

Work Experience

2009 – 2010	Laboratory Assistant sol-gel and corrosion, Technische Universität Darmstadt
2004 – 2005	Chemical Engineer, Projects supervisor in construction and maintenance of gas and oil production and treatment installations and as district supervisor, Energy and Oil Ministry, Pdvsa, Venezuela
2004	Junior Professor in Chemistry, Technology Institute University of Táchira, Venezuela
2002 – 2003	Professor Assistant, Units Process Laboratory, Chemical Engineering, Universidad de Oriente, Venezuela
2001	Cense Supervisor, Cense -2001, National Statistics Institute, Venezuela

Languages

Spanish (native languish), German (fluent), English (advanced)

List of Publications

1. C. J. Ochs, F. Sittner**, R. Ugas-Carrión,** M. Yekehtaz, S. Flege and W. Ensinger, Structural and electrochemical characterization of zirconium and silicon based sol-gel coatings for corrosion protection, Current Topics in Electrochemistry 13, 59-65 (2008).
2. **R. Ugas-Carrion,** F. Sittner, C.J. Ochs, S. Flege, W. Ensinger, Characterization of the porosity of thin zirconium oxide coatings prepared at low temperatures, Thin Solid Films, 517 [6] 1967-1969 (2009).
3. **R. Ugas-Carrion,** F. Sittner, M. Yekehtaz, S. Flege, J. Brötz and W. Ensinger, Influence of stabilizing agents on structure and protection performance of zirconium oxide films, Surf. Coat. Technol., 204, 2064-2067 (2010).
4. M. Yekehtaz, F. Sittner, **R. Ugas-Carrión,** S. Flege, J. Brötz and W. Ensinger, Characterization of Protective Sol-Gel Coatings on Magnesium Based on Phenyl-triethoxysilane Precursor, Thin Solid Films 518, 5223-5226 (2010).

Presentations

1. Poster (oral poster presentation): Influence of stabilizing agents on structure and protection performance of zirconium oxide films, E-MRS Spring Meeting Strasbourg Symposium P: Protective Coatings and Thin Films – June, France, 2009.
2. Poster presentation: Effect of stabilizing agents on the structure and interface composition of thin protective zirconium oxide films, 17th ISSC Conference, University of Reading, England, March-April, 2009.

Academic Awards

-DAAD – Fundayacucho scholarship for Ph.D. Study, 2006-2009 at the Technische Universität Darmstadt, Germany

-Student Award, EMRS-09, Strasbourg, France.

.

Darmstadt, 10.08.2010

Ruperto Ugas Carrión,

Wendelgasse 4,
35037 Marburg

Eidesstattliches Erklärung

Ich erkläre hiermit an Eides Statt, dass ich meine Dissertation selbständig und nur mit den angegebenen Hilfsmitteln abgefertigt habe.

Unterschrift

Ruperto Ugas Carrión

Darmstadt, 10.08.2010

Ruperto Ugas Carrión

Wendelgasse 4,
35037 Marburg

Erklärung

Ich erkläre hiermit, noch keinen Promotionsversuch unternommen zu haben.

Unterschrift

Ruperto Ugas Carrión